The *XRISM* Proposers' Observatory Guide

Gate-Valve Closed Version: February, 2024

Announcement of Opportunity #1

Institute of Space and Astronautical Science (ISAS/JAXA),
X-ray Astrophysics Laboratory
NASA's Goddard Space Flight Center (GSFC)
and the
European Space Agency (ESA)

Copies of this guide are available in `html` and `pdf` formats.

Contents

List of Figures

List of Tables

Chapter 1

Introduction

The X-Ray Imaging and Spectroscopy Mission (*XRISM*) is a mission led by Institute of Space and Astronautical Science (ISAS) of Japan Aerospace Exploration Agency (JAXA) in collaboration with the National Aeronautics and Space Administration (NASA), the European Space Agency (ESA), and other partners in Japan and around the world. Its main purpose is to perform high spectral resolution, high throughput imaging X-ray spectroscopy of celestial X-ray sources. *XRISM* was lanched on 2023 September 6 (UT) on a JAXA HII-A rocket. As of this writing, the initial in-orbit check-out and commissioning phase of *XRISM* has just concluded, and 6 months of Performance Verification (PV) observations, whose targets have been chosen by the *XRISM* Science Team, have started. Subsequently, *XRISM* will become a general purpose observatory open to all astronomers, with annual calls for proposals issued in parallel by JAXA, NASA, and ESA. In addition, all PV data will enter public archive 1 year after the conclusion of the PV phase; all subsequent observational data will enter public archive after an initial 1-year exclusive use period.

The scientific payload of *XRISM* consists of two instruments, Resolve and Xtend.

The Resolve instrument has a Gate Valve (X-ray aperture door) that protects the detector on the ground as well as during launch and early operations, and is meant to be opened during commissioning. However, the Gate Valve has not opened, thereby shifting the nominal energy band of Resolve from 0.3–12 keV to 1.7–12 keV and lowering the effective area. While the *XRISM* team will continue to assess different approaches to opening the Gate Valve, the Cycle 1 program will be carried out with the closed Gate Valve configuration, and therefore this document describes Resolve in this configuration. Note that the Resolve Gate Valve does not affect the Xtend instrument.

- Resolve, a soft X-ray spectrometer, which combines a lightweight X-ray Mirror Assembly (XMA) paired with an X-ray microcalorimeter spectrometer, and provides non-dispersive $\sim$5 eV energy resolution in the 1.7–12 keV bandpass with a field of

view of ∼3 arcmin.

- Xtend, a soft X-ray imager, consisting of an array of four CCD detectors that extend the field of the observatory to 38×38 arcmin^2 over the energy range 0.4–13 keV. Xtend uses a lightweight XMA identical in design to that used for Resolve.

These instruments are nearly identical to the two soft X-ray instruments flown on *Hitomi*, a mission that was lost shortly after launch in 2016[1]. The Soft X-ray Spectrometer (SXS) on *Hitomi* and Resolve on *XRISM* are sufficiently similar, as are the Soft X-ray Imager (SXI) on-board *Hitomi* and Xtend on *XRISM*, that the papers based on *Hitomi* data serve as an excellent guide in preparing *XRISM* observing proposals. Note also that all *Hitomi* observations were carried out with the SXS Gate Valve closed. In addition, data formats as well as data analysis and simulation software for *XRISM* are based largely on those developed for *Hitomi*.

1.1 Purpose and Scope of this Document

This document is intended for researchers who have some general understanding of space-based astronomy and X-ray observations. It should provide the readers with a general understanding of the characteristics of Resolve and Xtend, including on-board data handling, calibration, and operational limitations. This document also explains the basics of how *XRISM* will be operated, and how the observing time will be allocated. Based on this document, the reader should be able to determine whether *XRISM* is the appropriate instrument to address their scientific question, and how to design appropriate observing program for the proposal.

This document is not intended as a data analysis guide. Neither is it intended to provide in-depth descriptions of the instruments. In addition, the mechanical details of proposal submission will be explained elsewhere.

The document is organized as follows. Chapter 2 summarizes the principal characteristics of the detectors on-board *XRISM*. Chapter 3 covers how the observing time will be allocated. This includes data rights and time available for General Observers (GOs), as well as policies regarding Targets of Opportunity (TOOs). In addition, observational constraints due to the orbit, Sun angle, and the pointing accuracy are described. The proposal process is reviewed, including how to submit a proposal, how they will be evaluated, and how observations will be scheduled, performed, and the results disseminated.

The subsequent three chapters describe XMA (Chapter 4), Resolve (Chapter 5), and Xtend (Chapter 6). Finally, Chapter 7 and Chapter 8 focus on particular caveats associated

[1]Note that *XRISM* does not carry the equivalents of the hard X-ray and soft gamma-ray instruments on-board *Hitomi*.

with, respectively, extended sources and bright sources, which may thus be of importance for many proposers.

Disclaimer:

The current version of this document was prepared largely based on the best pre-launch understanding of the observatory and its instruments, with some early indications from early commissioning activities. Our understanding of the performance of the mission is expected to evolve, quantitatively if not qualitatively. Any significant new information will be made available at our websites and through other communication channels.

Chapter 2

Mission Description

This chapter is a brief introduction to the satellite and its instruments and is intended to provide a quick overview. Reading it thoroughly should provide the reader with the necessary information to understand the capabilities of the instruments at a level sufficient to judge if *XRISM* is suitable for a scientific project, and to prepare the feasibility section of a *XRISM* proposal.

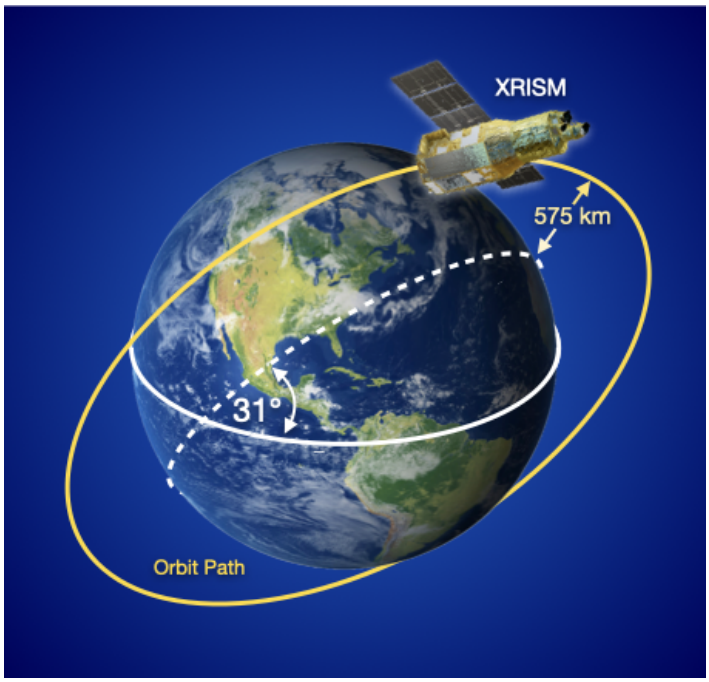

Figure 2.1: The 96 minute *XRISM* orbit.

2.1 Spacecraft: Orbit and Attitude

XRISM is in many ways similar to previous Japanese X-ray astronomy satellites (e.g., *Suzaku*) in terms of orbit, pointing, and tracking capabilities. *XRISM* is placed in a near-circular orbit with an apogee of ∼575 km, an inclination of ∼31 degrees, and an orbital period of about 96 minutes (Figure 2.1). From this altitude, most targets are occulted by the body of the Earth for about 1/3 of each orbit, except those near the orbital poles. Additionally, during passages through the South Atlantic Anomaly (SAA), the instruments will not produce usable data. Thus a 1 day observation of a target typically results in about 40 ks of good on-source time.

The maximum slew rate of the spacecraft is 4.5 degrees/min, and settling to the final attitude takes ∼ 10 minutes, using the star trackers. Given the relatively long slew time, the normal mode of operation is to point at a single target for at least 1/4 day (10 ks net exposure time) and often several days, without interleaving multiple targets.

Objects near the spacecraft orbital poles will not suffer Earth occultations (i.e., they are in the continuous viewing zone, CVZ), thus can be observed at a much higher efficiency. The orbit is predicted to precess with a period of about 2 months. The orbital poles will be at declinations of ± 59 $(90 - 31)$ degrees and a right ascension that changes with the precession phase. Because the evolution of *XRISM* orbit is influenced in part by the atmospheric drag, accurate long-term prediction for the times when a given target is in CVZ is not feasible.

The *XRISM* instruments are oriented perpendicular to the solar panels, which are fixed to the spacecraft, and must remain pointed to within 30 degrees of the Sun. Therefore, targets can be observed only when their Sun angle is in the 60–120 degree range. This also implies a constraint on the roll angle: when the target is at a Sun angle close to 90 degrees, there is a ±30 degree range of possible roll angles. When observed close to the limits of Sun angles, the roll angle is tightly constrained.

The overall observing efficiency of the satellite is expected to be about 45%. Proposals should specify the desired good on-source exposure but without accounting for instrumental dead times due to high count rates, if relevant.

2.2 Overview of *XRISM* Instruments

XRISM carries two instruments, Resolve and Xtend, that are co-aligned and operate simultaneously, each behind its own X-ray Mirror Assembly (XMA). Here we provide a brief overview, leaving further details to chapters dedicated to these in turn. We show a schematic of the *XRISM* spacecraft in Figure 2.2.

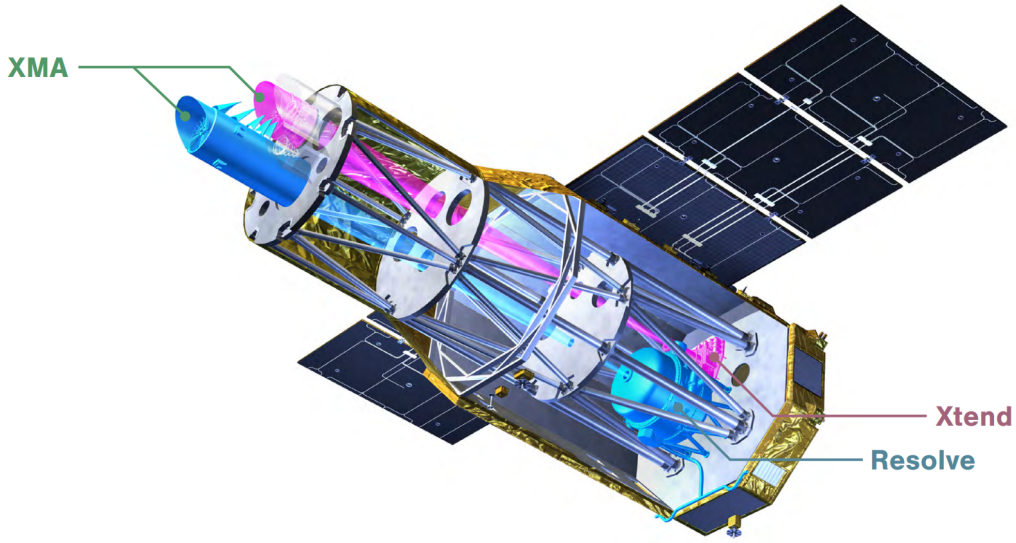

Figure 2.2: A schematic of the *XRISM* spacecraft. Resolve dewar and its XMA are highlighted in blue, while the Xtend instrument and its XMA are highlighted in pink. Image credit: JAXA.

2.2.1 X-ray Mirror Assembly (XMA)

The two near-identical X-ray Mirror Assemblies (XMAs) are used to focus X-ray photons on the two detectors. Both XMAs are composed of 203 thin reflector shells that use conical approximations of Wolter-I type optics, thereby resulting in a light-weight, large collecting area ($\sim$580 cm^{-2} at 1.5 keV and $\sim$420 cm^{-2} at 6.4 keV) X-ray telescopes. In terms of imaging quality, XMAs represent an incremental improvement over previous telescopes of the same type, such as those used for *Suzaku*. Half-power diameter (HPD) of 1.3$'$ is measured on ground for Resolve-XMA, and 1.5$'$ for Xtend-XMA. Stray light, or contaminating X-rays from outside of the field of view (FOV), is reduced by a stray-light baffle also called a Pre-Collimator (PC) placed above each reflector. A Thermal Shield (TS) is attached in front of the pre-collimator to stabilize the thermal environment of the telescope.

A more detailed descriptions of XMA can be found in Chapter 4.

2.2.2 Resolve

Resolve consists of an X-ray micro-calorimeter array of 6x6 pixels placed at the focus of an XMA, covering a $\sim 3' \times 3'$ arcmin^2 region of the sky. It is almost identical to the *Hitomi* Soft X-ray Spectrometer. Its unprecedented non-dispersive high spectral resolution (ΔE around 5 eV) capability is achieved by cooling the detector to 50 milli-Kelvin and measuring

the temperature rise when an X-ray photon is absorbed by the detector element.

The ability of the Resolve instrument to determine the photon energy depends on recording the complete history of temperature rise and decay associated with each photon, isolated from all other events, to be compared with templates. This leads to the concept of event grade. When the count rate is high, the fraction of high resolution events will decrease. Moreover, for very bright sources, there is a limit imposed by the Pulse Shape Processor (PSP) which is unable to process events at a rate above ∼200 per second (see Chapter 8 for more details). For both these reasons, it may be necessary and/or advisable to reduce the count rate of the brightest X-ray sources using a filter or offset pointing. For the former, both a neutral density and a (soft X-ray absorbing) beryllium filters are provided.

The effective area is ∼180 cm^2 at the 6–7 keV K-band, considerably larger than any other high-resolution X-ray spectrometers. The imaging capability is limited both by the pixel size and the imaging performance of the XMA. The calorimeter array is backed by an anti-coincidence detector that enables rejection of background events. The milli-Kelvin temperature in the Dewar is achieved by a cooling system that includes adiabatic demagnetization refrigerators, He coolants, and mechanical coolers. The cooling system allows redundancy and even cryogenic-free operation. For calibration, ^{55}Fe sources (one continuously illuminating a dedicated calibration pixel, and one on the filter wheel that can be inserted into the light path) and Modulated X-ray Sources (MXS) are available. The best strategy to utilize these calibration sources, as well as the in-orbit performance of Resolve in terms of gain and line spread function, are currently being investigated, but gain calibration accuracy of better than ∼1 eV is expected.

In comparison with grating instruments, the two key advantages of Resolve are:

- High spectral resolution for spatially extended sources: the energy resolution of Resolve is unchanged regardless of spatial extent, whereas those of grating instruments become degraded.
- High spectral resolution in its bandpass, particularly the Fe K region. Note that the energy resolution of Resolve is a slowly rising function of photon energy and is better than ∼5 eV for much of its bandpass except well above the Fe K band, resulting in a higher resolving power at higher energies. The opposite is the case for grating instruments whose wavelength resolution is roughly constant for a given order of a given instrument.

A more detailed descriptions of Resolve can be found in Chapter 5.

2.2.3 Xtend

Xtend is an array of four X-ray CCDs behind the other XMA. It has an imaging-spectroscopic capability of a wide field (38×38 arcmin^2) and a medium energy resolution in the 0.4–13 keV band (comparable to *Suzaku* XIS, *Chandra* ACIS, and *XMM-Newton* EPIC). There is a gap of ∼20 arcsecond between the chips (see Figure 2.3 for the layout). The nominal pointing position is placed at the center of Resolve FoV, which is offset from the center of Xtend by $\sim 5'$.

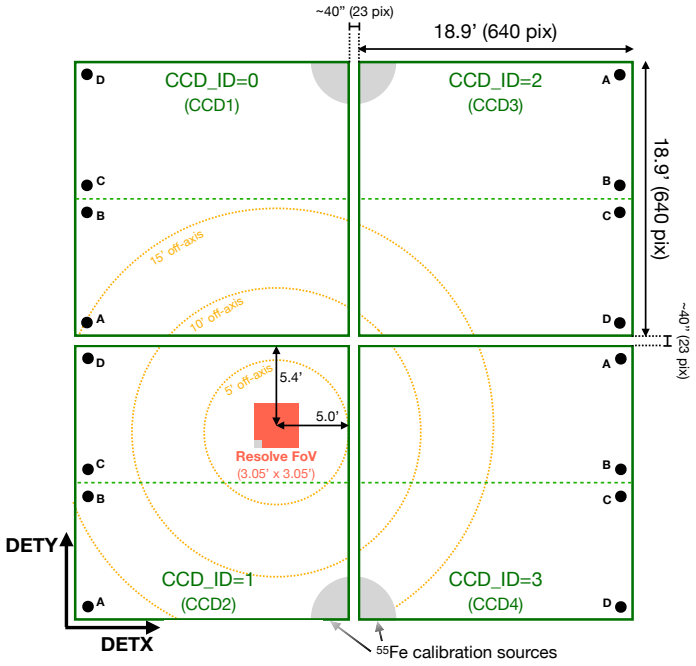

Figure 2.3: Schematic layout of the two scientific instruments on-board *XRISM*, Resolve and Xtend. This is the view looking toward the sky from the back of the focal plane.

The background level of Xtend is expected to be low and stable benefiting from the low-Earth orbit of the satellite. Above ∼7 keV, the use of a thick depletion layer should lead to a significant background reduction compared to the Back-Illuminated (BI) CCD in *Suzaku* XIS. All four CCDs on-board *XRISM* are BI devices and are more resistant to micro-meteorite impacts than Front Illuminated (FI) devices .

A more detailed descriptions of Xtend can be found in Chapter 6.

Table 2.1: *XRISM* capabilities at a glance.

S/C	Orbital apogee	575 km
	Orbital period	96 minutes
	Observing efficiency	$\sim 45\%$
XMA	Energy Range	0.3–15 keV
	Effective Area	$\sim$580 cm^{-2} at 1.5 keV
		$\sim$420 cm^{-2} at 6.4 keV
	Angular Resolution	$1.3'$ HPD for Resolve-XMA
		$1.5'$ HPD for Xtend-XMA
Resolve	Energy Range	1.7–12 keV
	Efective Area	$\sim$180 cm^2 at 6 keV
	Energy Resolution	$\sim$5 eV FWHM
	FOV	$3.05' \times 3.05'$ arcmin^2
	Pixels	6×6 array
	Filters	Open, ND, and Be
	Background	0.8×10^{-3} ct s^{-1} keV-1
Xtend	Energy Range	0.4–13 keV
	Effective Area	$\sim$350 cm^{-2} at 1.5 keV
		$\sim$300 cm^{-2} at 6.0 keV
	Energy Resolution	$\sim$180 eV FWHM at 6 keV
	FOV	$38' \times 38'$ arcmin^2

Chapter 3

Observation Policies

Following the PV phase, *XRISM* will enter the General Observer (GO) phase, which it will remain in for the lifetime of the mission, with annual Announcements of Opportunity (AO) released simultaneously by JAXA, NASA, and ESA. The institutional affiliation of the proposer determines which agency they should propose to. Persons at Japanese institutions should submit to the JAXA solicitation; those at US or Canadian institutions should submit to the NASA solicitation; and those with affiliations in ESA member and cooperating states should submit to the ESA solicitation. Persons with affiliations outside Japan, the US, Canada, or an ESA member state should submit to the JAXA solicitation, which reserves some time for such international proposals.

3.1 Data Rights

The data rights policy for *XRISM* is similar to previous missions. The normal exclusive use period for GO data is one year. This period may be waived if desired by proposers, but may not be extended.

3.2 Target Selection and Prioritization

The details of the AO are described more fully in the Call for Proposals (CfP). As with previous missions, proposals will be received by the relevant agency and evaluated by subject matter experts organized into review panels that make up the Time Allocation Committee.

Accepted targets will be classified into three categories: A, B, or C. Priority A and B targets are guaranteed to be observed, with A targets receiving a higher priority for observation scheduling. Priority C targets will be used as fillers when there are gaps in

the schedule. Priority A and B targets that have not been completed by the end of an observing cycle are carried over into the next cycle. Priority C observations that are not observed during that observing cycle are not carried over. The goal of the target selection process is to produce a combined list of targets representing approximately 140 percent of the available observing time, split among A (50 percent), B (40 percent) and C (50 percent) priority observations.

During Cycle 1, category A and B targets will be considered complete if 90% (for A targets) or 70% (for B targets) of the proposed time is obtained on the source. In general, supplementary observations will be performed for A or B targets that do not meet the completion criteria, although it may not always be possible in case of time critical observations.

During the GO phase, data from calibration and TOOs requested outside the proposal process (see below) will not be considered proprietary and will not have an exclusive use period.

3.3 Target of Opportunity (TOO) Proposals

TOO proposals are allowed for *XRISM* through the normal proposal process, although they must be ranked as Priority A to be accepted. Proposals with TOOs should not be mixed with non-TOO targets. TOO proposals are allowed for short-lived events in known objects, the timing of which is uncertain. The trigger criteria **must** be explicit and quantifiable, and stated in detail in the proposal text; a brief summary should appear in the "Remarks" section of the target form. In addition, TOO proposals **must provide an estimated probability of a successful trigger** during the AO period. It is **the PI's responsibility** to notify the *XRISM* project when the criteria are met. **Generic TOOs without a specific target (such as "a nearby supernova") will not be accepted in Cycle 1. The number of targets in TOO proposals should not exceed 10.** These policies are subject to change in future cycles.

3.4 Pointing Constraints

The Solar panels on the *XRISM* satellite are fixed. This places a restriction on the pointing direction with respect to the satellite-Sun line: the Sun angle constraint during Cycle 1 is 60–120 degrees. This means that at any given time of the year, only a swath of the sky 60 degrees wide is accessible for astronomical observations, and thus most celestial sources are available for observations for about 60 days every 6 months. If a specific observing date or a coordinated observation with other missions is required, the proposer must first determine if the observation is possible. This can be done using the "`Viewing`" tool on the HEASARC website:

`https://heasarc.gsfc.nasa.gov/cgi-bin/Tools/viewing/viewing.pl`

Long (>1 day) observations are the norm for *XRISM*. A large number of short observations is an inefficient use of the satellite because of the unusable time during slews and attitude settling. The pointing is expected to be accurate to $0.3'$ and can be reconstructed to better than $0.2'$, except during the initial settling period of up to 10 minutes. Moreover, there is a limit on the number of slews that can be uploaded to *XRISM*. For these reasons, a minimum exposure time of 10 ks has been set for all proposed observations. For Cycle 1, observations will be limited to 300 ks per pointing with the total not to exceed 600 ks per proposal.

Contiguous observations, i.e., observations not disrupted by the observation of another target, are generally guaranteed up to exposures of not more than 100 ks. This limitation is due to moon light constraints for the star trackers' field of view, conflicts with other time critical observations, and other operational/planning difficulties. While the operation team does accept requests for uninterrupted observations longer than the 100 ks, these are conducted on a best-effort basis.

Even during shorter pointed observations, there will typically be interruptions due to the location of *XRISM* in a low Earth orbit: Normally, a target will be occulted by the Earth for ∼30 minutes every satellite orbit. In addition, *XRISM* will pass through the South Atlantic Anomaly (SAA) during parts of 5 or 6 orbits every day. Due to the harsh radiation environment of the SAA, scientific observation is not possible during SAA passages. There are other variations in the particle background, depending primarily on the Cut-Off Rigidity (COR)[1]. Please check the *XRISM* website for the most up-to-date suggestions to reduce times of high background while maximizing the science.

There are also orbital constraints on the orientation of the projected Resolve and Xtend FOV on the sky. Since both are approximately square, specific roll angle is not expected to be a common requirement. However, if a specific roll angle is scientifically advantageous, the proposer must first determine if it is allowed. Interested proposers are directed to the *XRISM* GOF web site for details. Then the required roll range can be entered on the RPS proposal form. For objects close to the ecliptic poles it is possible to arrange for any roll angle by scheduling observations at a specific time, but for those located close to the ecliptic, Resolve and Xtend will project on the sky in a nearly fixed orientation. **Note that any roll constraint will make a proposal time critical.**

It is possible to specify the time of observations (time critical, or TC, observations) in order to observe during specific phases or for simultaneous observations. Monitoring observations (repeated observations with a specified interval) or roll-angle constrained observations are also considered time critical, and must be so flagged on the proposal form. The total accepted time of TC and TOO proposals will be restricted; the numerical limit

[1] *XRISM* is protected from solar and cosmic-ray particles by the geomagnetic field. The COR is an indicator of the minimum momentum required for a particle to reach a specific location, given the average geomagnetic field configuration.

will be evaluated based on experiences but may be of order 15% of the total observation, and proposers should justify their requirements carefully.

Overall the proposers are strongly urged to provide the most accurate information possible. All information that is indispensable for operation planning should be provided on the electronic forms. The PIs are advised to utilize the "Remarks" area if they have detailed requests which cannot be expressed with the check boxes/pull-down menus.

3.5 Events After Submission

After the *XRISM* proposal deadline, there will be three independent proposal reviews for the NASA, JAXA, and ESA proposal solicitations. Each review will create a target list from the proposed observations, ranking the accepted targets as category A, B, or C. Only category A and B targets are guaranteed to be observed. As stated above, TOOs and time critical observations are only accepted within some limit (approximately 15% of the total time) – however, the project will review this limit before the final target selection is made. Category C targets will be observed as time permits. An international merging committee will collate the three target lists and produce a single, unified list. Overlaps among targets accepted by multiple agencies will be resolved, either by merging the investigations (if both parties are willing) or by choosing one. In the latter process, the priority given by the national reviews, as well as the lengths of the accepted observations, will be considered. The final target list will be $\sim$ 40% oversubscribed. Category A targets will have 50% of the available time, category B 40%, and category C 50%.

The Cycle 1 allocation of GO time among the mission partners is 48% for Japanese investigations (including 4% for international proposals), 44% for US investigations (including Canada), and 8% for ESA investigations.

Even though observations are scheduled to acquire roughly the approved exposure time and although this will usually be achieved with *XRISM*, occasional losses of usable observation time are inevitable. As mentioned above, Category A observations will be deemed complete when they have received at least 90% of the approved time. Note that this will be judged based on the good time intervals of the cleaned Resolve event files after the standard screening. Additional observations will be scheduled automatically for those non-time-critical targets the observations of which are considered incomplete by the project scientist at ISAS. In the case of time-critical observations which are incomplete or unusable, it will be the PI's responsibility to determine the best course of action.

Each PI will be assigned a contact scientist, either at ISAS or the NASA *XRISM* GOF, who will work with the PI to assure the maximum science return. This will include double-checking coordinates, count rates and finalizing configurations (nominal pointing, modes, etc.). It is important to note that once an observation has been scheduled, any delay in responding to questions from the contact scientist may result in targets being removed

from the schedule.

Once the observation has been completed, the data will be promptly run through the processing pipeline and put into both the US and Japanese archives in encrypted form. The PI will be sent the decryption key, along with instructions on how to download and decrypt the data.

With the exception of the code that converts raw binary telemetry into FITS format files, all *XRISM* software is written as FTOOLS and distributed through the *XRISM* team at ISAS/JAXA and the NASA/GSFC HEASARC. This includes the tools used in the processing. All calibration files are distributed through the HEASARC `caldb` (calibration database) system. This enables users to apply any calibration updates themselves. The *XRISM* team at ISAS and the NASA *XRISM* GOF provide additional `FTOOLS` that may be necessary or desirable for analyzing *XRISM* data. The use of other software packages will only be supported at a lower priority level.

Chapter 4

X-Ray Mirror Assembly (XMA)

XRISM has two X-ray Mirror Assemblies (XMAs) focusing X-rays onto the focal plane detectors. One of these mirrors, Resolve-XMA, focuses X-rays on Resolve, while the other, Xtend-XMA, is used with Xtend. Both mirrors have identical design and improve on the mirrors on-board *Suzaku*. The entire system (see Figure 4.1) consists of an X-ray mirror, a Pre-Collimator (PC) stray light baffle, and a thermal shield.

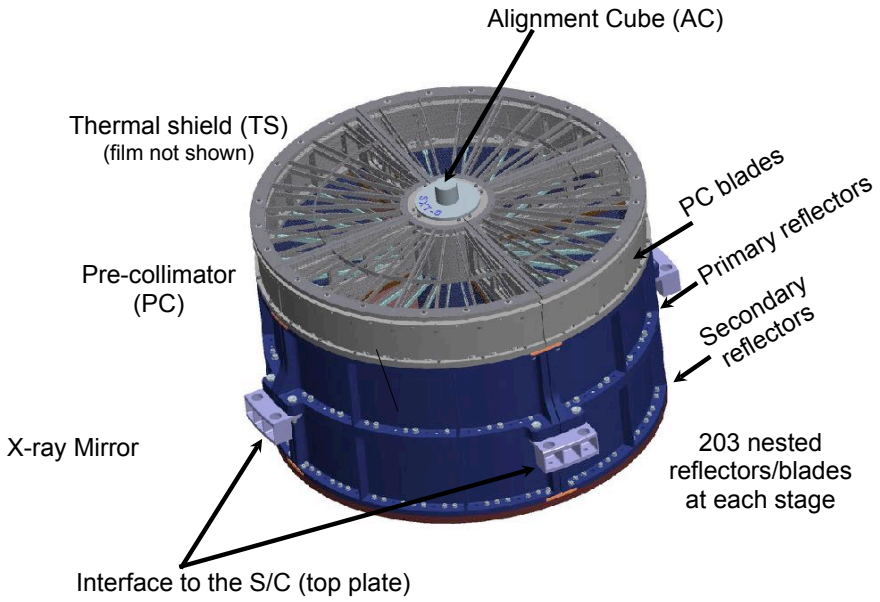

Figure 4.1: Image of the XMA with all its components.

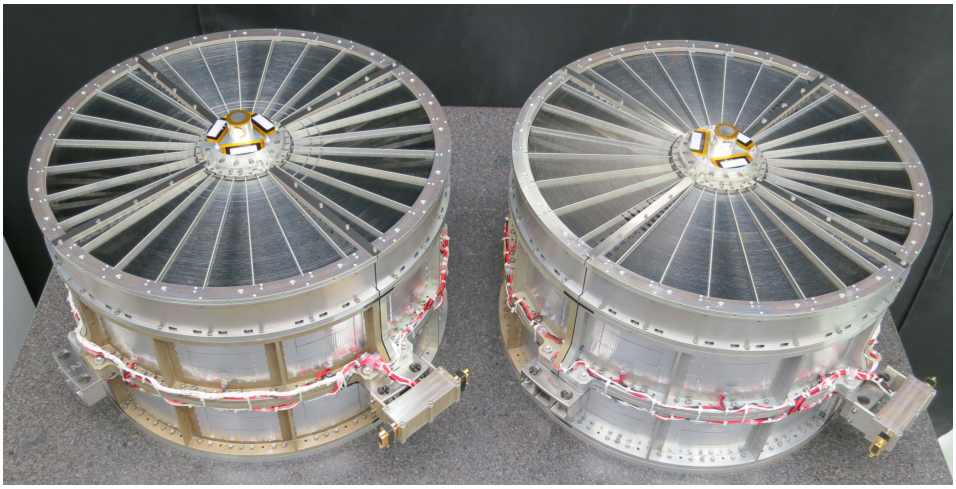

Figure 4.2: Picture of the X-ray Mirror Assemblies, without thermal shields (right: Resolve-XMA, left: Xtend-XMA).

Table 4.1: XMA parameters and their characteristics.

	XRISM XMA
Focal length	5.6 m
Effective aperture diameter	12 – 45 cm
Height	20 cm
Number of reflectors	203
Reflecting surface	gold
Grazing angle	0.15° – 0.57°
Energy range[1]	0.3 – 15 keV
Effective Area[2]	587 cm^2 1.5 keV
	438 cm^2 4.5 keV
	418 cm^2 6.4 keV
Angular Resolution (HPD)	1.3′ for Resolve-XMA and 1.5′ for Xtend-XMA
Angular Resolution (FWHM)	8″ for Resolve-XMA and 7″ for Xtend-XMA

[1]The nominal energy range of XMAs is 0.3 – 15 keV. XMAs have sensitivity to higher energy ($>$ 15 keV) photons but the calibration accuracy declines. [2]Includes telescope, pre-collimator, thermal shield but not the detectors. Values are from Boissay-Malaquin et al. (2022).

4.1 XMA Components

4.1.1 Mirror Part

The XMA mirror, with an outer diameter of 45 cm, and a 5.6 m focal length, uses conical approximations to the Wolter Type I configuration with 203 nested shells consisting of 1624 individual reflectors (Figure 4.2). The reflective surfaces of the reflectors consist of a single-layer coating of gold. The reflectors are arranged in four quadrants for each set of primary and secondary housings. Seven holding bars on the top and bottom sides support the reflectors. The reflector substrates are composed of Aluminum, and the 203 shells are organized into three groups, with different substrates thicknesses per group. An epoxy buffer layer helps focus grazing-incidence X-rays with energies up to 15 keV. In addition to the reflectors, bare substrate foils are installed inside the innermost primary reflectors to stop the incident X-rays from directly arriving at the innermost secondary which is a path producing the stray light (see Section 4.1.2). A pre-collimator, installed for stray light protection, consist of coaxially nested cylindrical aluminum blades placed above each reflector. A thermal shield (TS) is attached in front of the pre-collimator to stabilize the thermal environment of the XMAs. The shield is made of Al-coated Polyimide to ensure a large effective area in the soft energy band. The thermal shield transmits soft X-rays but helps to reduce the radiative heat transfer into and out of each XMA.

The final result is a relatively light mirror with large throughput over a broad energy range (Serlemitsos et al., 2010, and references therein). Although largely inspired by *Suzaku*'s mirrors, the two XMA mirrors benefited from both relaxed weight constraints and several fabrication improvements, including thicker substrates, a larger number of forming mandrels, thinner epoxy layer for replication, stiffer housings, and higher-precision alignment. All these improvements yield better overall mirror performances, including a smaller angular resolution and an improved effective area both at 1 keV and at 6 keV (Okajima et al., 2012). The XMA was developed at NASA GSFC in collaboration with JAXA/ISAS, and Tokyo Metropolitan University in Japan. The summary of each mirror performance compared when necessary to the relevant requirement is given in Table 4.1. Unless explicitly noted, the parameters mentioned in the table are identical for both mirrors.

4.1.2 Pre-Collimator

The grazing-incidence optics adopted for X-ray imagining use a large number (203 in the case of *XRISM*) of reflectors nested as tightly as possible to increase the effective area. As a result, this configuration increases the possibility of reflection other than the normal double reflection within the telescope. These contaminations of abnormal paths are referred to as "stray light." Studies on the *ASCA* stray light (Mori et al., 2005) showed that the main contribution to the stray light is from secondary reflections of photons with an incident angle between τ and 2τ (where τ is the angle of the primary reflector measured from the

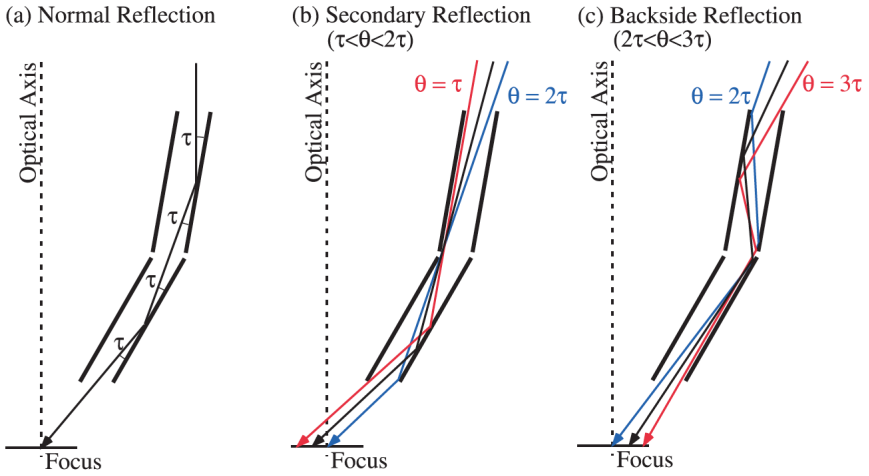

Figure 4.3: Major reflection paths occurring in the XMA structure. (a) Normal double reflection of the X-ray arriving from the on-axis direction. Incident X-rays are bent by the angle 4τ in total, and converge to the on-axis focus: (b) Secondary reflection, which arrives at the focal plane only if the incident angle of the X-ray, θ, measured from the optical axis is in the range $\tau < \theta < 2\tau$: (c) Stray light path that gives rise to the brightest ghost among various backside reflections, the reflection at the backside of the primary followed by the normal double reflection. This pattern occurs when the X-ray incident angle is in the range $2\tau < \theta < 3\tau$. From Mori et al. (2005).

optical axis of the telescope – see Figure 4.3). Therefore, a pre-collimator is installed in order to address the issue of both secondary and backside reflection that would otherwise contaminate data on the focal plane.

The Pre-Collimator (PC) built for *XRISM* is derived from the one on *Suzaku*. Each PC consists of cylindrical aluminum shells (blades) with varying radii of 60 – 225 mm, alignment frames to guide the blade positions, and the blade housing body. Each PC blade is placed precisely on top of the respective reflector to reduce off-axis X-ray photons that leads to a "ghost" image within the detector field of view. Since the secondary reflection is caused by the off-axis X-rays going just above the primary mirrors, these cylindrical blades can block this component effectively. The blade thickness is designed to be narrower than that of the reflector. Thus, there is no loss of the on-axis effective area if the alignment between the mirrors and blades is attained. The alignment frame and the housing are made of Aluminum. Heat-forming process is introduced to the production to stabilize the blade shape in orbit. Precise curvature of radius and the linearity along with the direction of incident X-rays ensure that the blades do not obscure the telescope aperture. Figure 4.4 shows a pre-collimator and its geometry and Table 4.2 shows the main characteristics of the XMA pre-collimator.

Table 4.2: The main characteristics of the XMA pre-collimator.

Number of segments	4
Material	Aluminum
Number of blades	204
Number of support bars	7

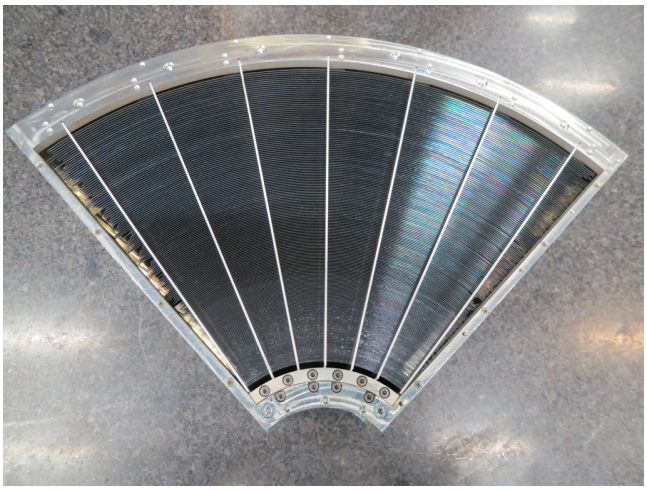

Figure 4.4: Image of a Pre-collimator quadrant used for *XRISM* XMA.

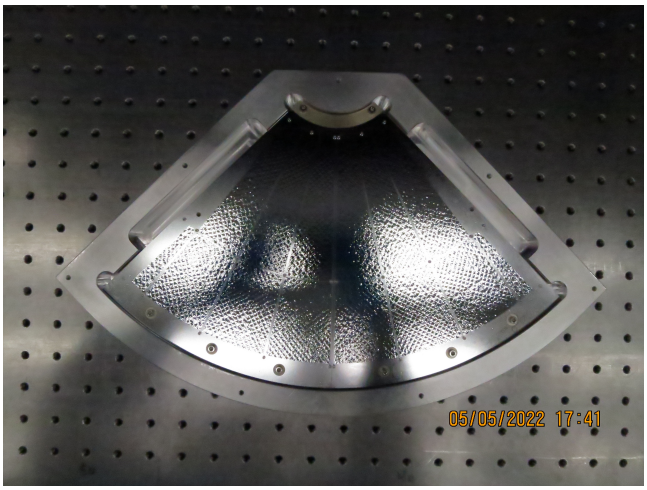

Figure 4.5: Image of a thermal shield quadrant used for *XRISM* XMA.

4.1.3 Thermal shields and heaters

Per requirement, the operating temperature of the telescopes in orbit must be maintained at 22°± 7 °C. This is achieved by covering the entrance side with a thermal shield (TS) composed of the 4 thermal shield quadrants shown in Figure 4.5 for each XMA. These shields isolate the telescopes thermally from space and reflect infrared radiation from the interior of the spacecraft. The thermal shields also work to block optical light coming either from the sky or from the surface of Earth illuminated by the Sun.

The shields are made of an aluminized Polyimide glued to a supporting stainless-steel mesh. The reflectivity in the optical wave band is more than 90%, and yields a rejection of the optical light from the bright Earth and the reflection of the IR radiation from the telescopes at ∼290 K back to the interior of the satellite. In addition to the shields, heaters are affixed to the wall of the housing to keep it within the mandated temperature range. The whole XMAs are inside the sunshade base. Thermometers are attached to the wall to monitor the temperature and control the heaters.

4.2 Expected Performance

4.2.1 Focal Positions and Optical Axis

For each mirror, the transmission is maximized when the target is observed along the optical axis. The left diagram of Figure 4.6 shows the "ideal" telescope+detector system. The actual configuration of a mirror includes a shift between the focal point and the detector aimpoint (shown in the middle diagram) and a tilt of the mirror optical axis with respect to the nominal aim-point (shown in the right diagram). Moving off the detector aimpoint from the mirror on-axis focal point results in reducing the effective area due to vignetting. This places the boresight measurement and the determination of the optical axis position as one of the highest priority among the calibration requirements for both instruments. The detector aim point is defined as the center of the Rosolve field of view. The optical axis is tilted about 15" with respect to the nominal aim-point direction, as this angle makes the maximum on-axis effective area. With this small angle, the loss of the effective area is less than 0.5% due to vignetting and is negligible. However, the focal point may shift to +Y direction as indicated in Figure 4.7. Xtend is on-axis at aim point (less than 3" shift). Detailed in-flight calibration is forthcoming. However, the alignment configuration measured at the ground should be adequate for Cycle 1 proposal preparation. Figure 4.7 indicates the location of the detector aim point with respect to the Xtend and Resolve FoVs. The boresight and the pointing accuracy are around 20 arcsec for Resolve and Xtend.

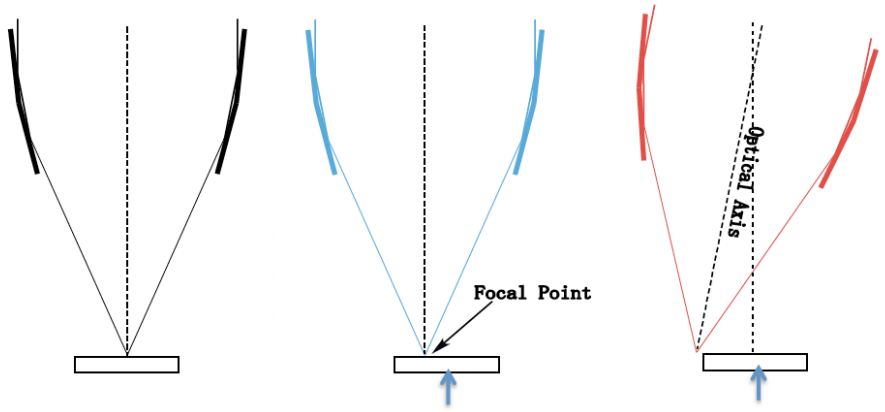

Figure 4.6: Cartoon view of the actual configuration of a mirror compared to the ideal geometry (shown on the left). The middle picture illustrates the shift between the focal point and the detector aim point and the right picture shows in addition the effect of a tilt of the optical axis with respect to the nominal aim-point direction (HITOMI in-flight calibration plan, 2015.)

4.2.2 Effective Areas

The predicted effective area of both the Xtend-XMA and Resolve-XMA can be calculated using ground measurements combined with ray-tracing simulations. Table 4.3 lists the ground measurements for both the Xtend-XMA and Resolve-XMA (Boissay-Malaquin et al., 2022). The simulated effective area curves are plotted in Figure 4.8.

Table 4.3: Effective area (in cm^2) for both XMAs (with 68% statistical errors), at different energies E, for the whole telescope axis. From Boissay-Malaquin et al. (2022)

Energy [keV]	Effective Area (cm^2)	
	Resolve-XMA	Xtend-XMA
1.5	584.7 ± 0.4	589.4 ± 0.4
4.5	434.7 ± 0.6	441.5 ± 0.6
6.4	416.0 ± 0.6	422.2 ± 0.6
8.0	345.3 ± 0.8	349.2 ± 0.8
9.4	233.4 ± 0.6	235.5 ± 0.6
11.0	163.4 ± 0.4	164.5 ± 0.4
17.5	38.4 ± 0.2	37.9 ± 0.1

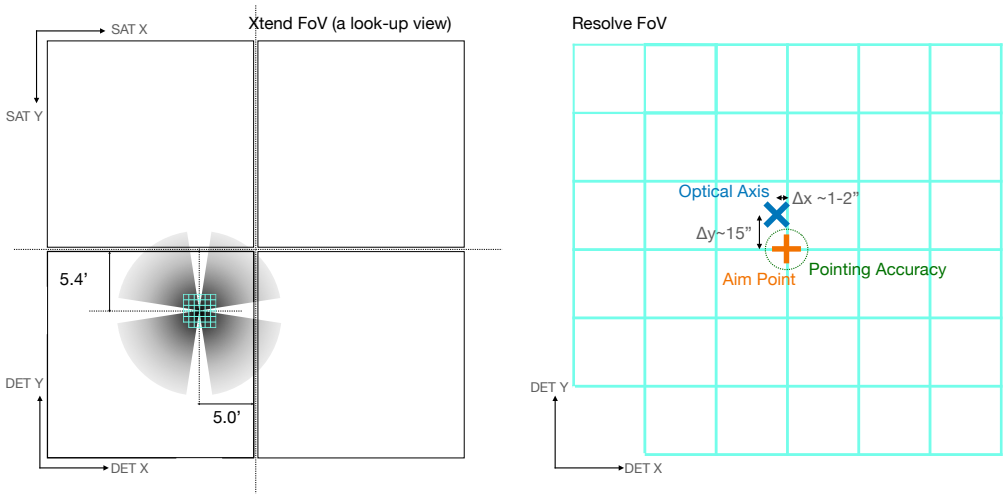

Figure 4.7: Left: Layout of Xtend FoV (black) superimposed with Resolve FoV (cyan). This is a look-up view. The expected Xtend aimpoint is located from ∼5.0′ (DETX) and ∼ 5.4′ (DETY) from the edges of the CCD. The ground calibration reported that Xtend is on-axis at aim point (less than 3" shift). Right: The expected aimpoint of Resolve as the center of Resolve FoV. The ground calibration reported that optical axis of the XMA-Resolve is slightly shifted. In-flight calibration is on-going.

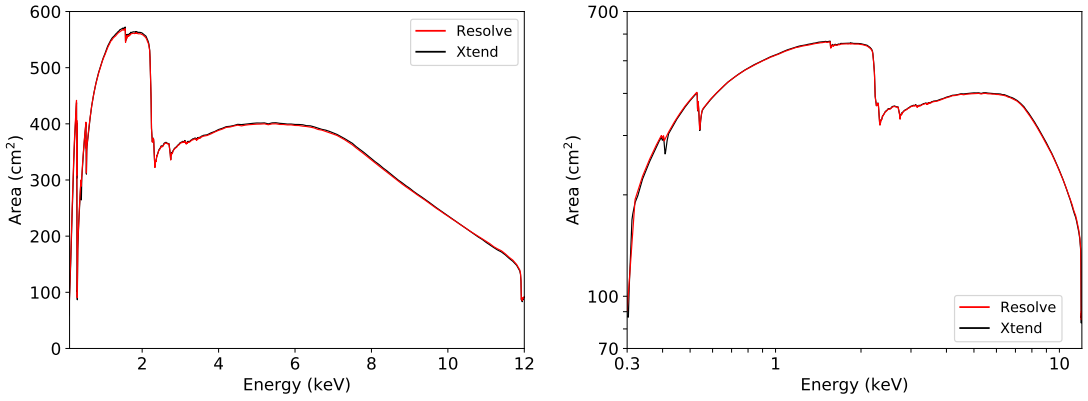

Figure 4.8: Effective area versus energy, for Xtend-XMA (black) and Resolve-XMA (red) plotted on the linear scale (left) and on the log scale (right). Note that these simulated curves are based on ground measurements and the XMA-only effective areas, thus not including QE of the detectors, etc..

4.2.3 Vignetting

The vignetting measures the variation of the effective area as a function of off-axis angle. It also depends on the photon energy as well as the azimuthal angle. The left panel of Figure 4.9 shows the vignetting curves measured on the ground at different energies (shown by open squares on the plot) fitted with 1D Lorentzian model, for Cross direction 1 (azimuthal angle: 0-180°, see the right panel of Figure 4.9), for Xtend-XMA. The similar curves for Resolve-XMA is shown in Figure 4.10, using a smaller off-axis angle range and 1D Lorentzian model. Figure 4.11 shows these vignetting curves at 6.4 keV for 8 different azimuthal angles for both well fitted with Resolve-XMA and Xtend-XMA, revealing a very similar mirror FoV (defined as FWHM at 6.4 keV of 1D Lorentzian model) of about 14 arcmin for both XMAs.

Figure 4.12 shows the size of XMAs' Field of View (not the detector FoVs), as a function of energy.

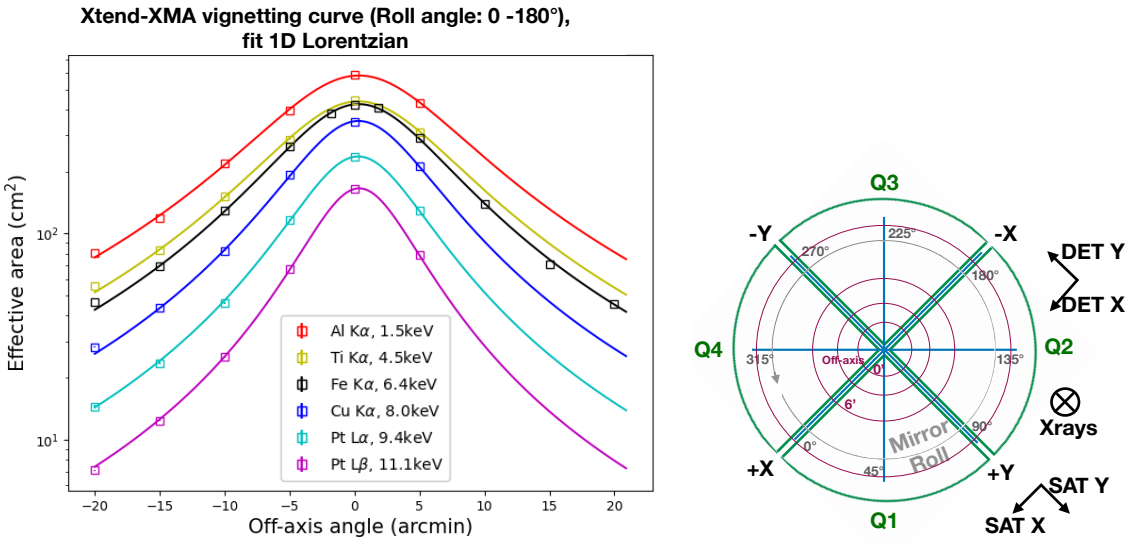

Figure 4.9: Left: Vignetting curves of all energies, for Xtend-XMA, for azimuthal 0-180 deg, fitted with the sum of Lorentzian and Gaussian models to the data measured on the ground. Right: Look-down illustration of the mirror roll angle (different from the spacecraft roll angle) and the off-axis angle used during the ground calibration measurements (see Boissay-Malaquin et al. (2022)). The coordinates of the satellite and detector are shown, as well as the boundaries of the XMAs' quadrants.

4.2.4 Angular Resolution

The Point-Spread Function (PSF) was measured at nine different energies. Figure 4.13 shows the on-axis focal plane image of the Resolve-XMA and Xtend-XMA, illustrating that the PSF has structures. The PSF structures may have to be taken into account when

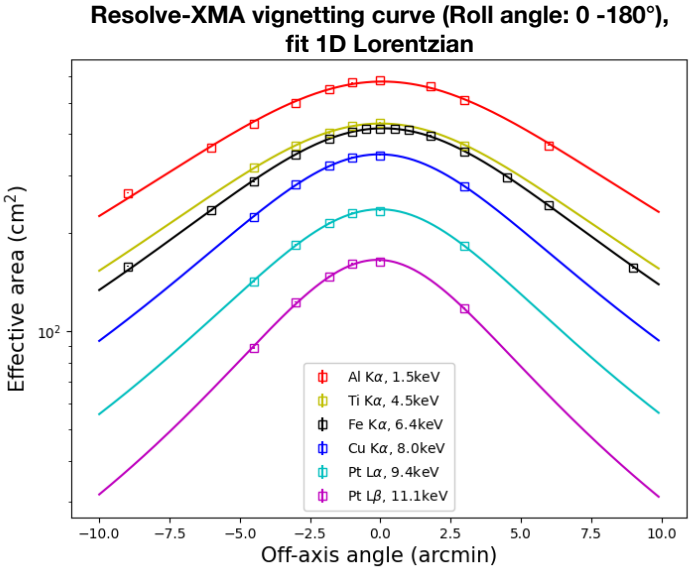

Figure 4.10: Vignetting curves of all energies, for Resolve-XMA, for roll angle (azimuthal angle) 0-180 deg, fitted with 1D Lorentzian model fitted to the data measured on the ground.

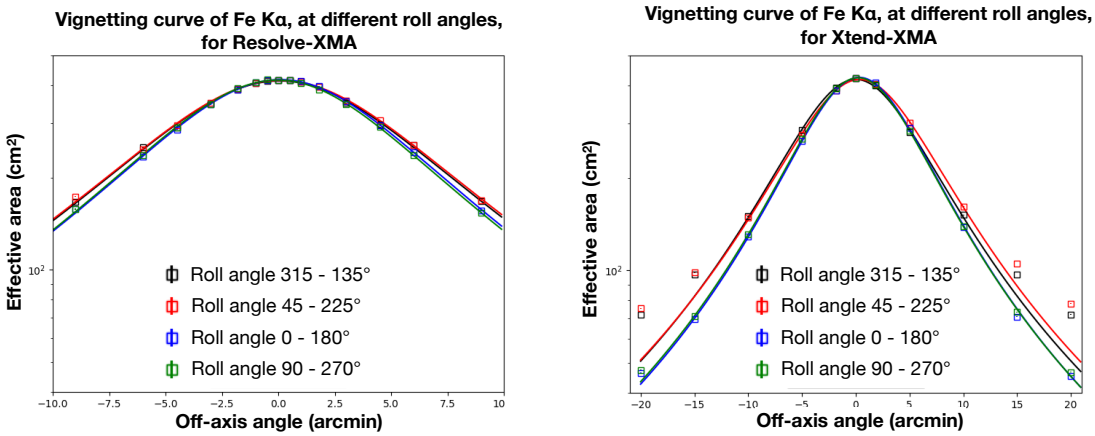

Figure 4.11: Vignetting curves at 6.4 keV fitted to the data points measured on the ground, for Resolve-XMA (left) and Xtend-XMA (right), for 8 roll (azimuthal) angles (see the right panel of Figure 4.9).

planning to observe a bright source or analyzing extended sources with a bright point source (Chapters 7 and 8). One-dimensional PSF, which was normalized so that the total number of photons is unity within a radius of 8′, and of the Encircled Energy Function (EEF) for both Xtend-XMA and Resolve-XMA are given in Figure 4.14 and Figure 4.15, respectively. Both figures also exhibit that the profiles are a function of the incoming photon energy. Table 4.4 summarizes the values of the Half-Power Diameter (HPD) angular resolution. For

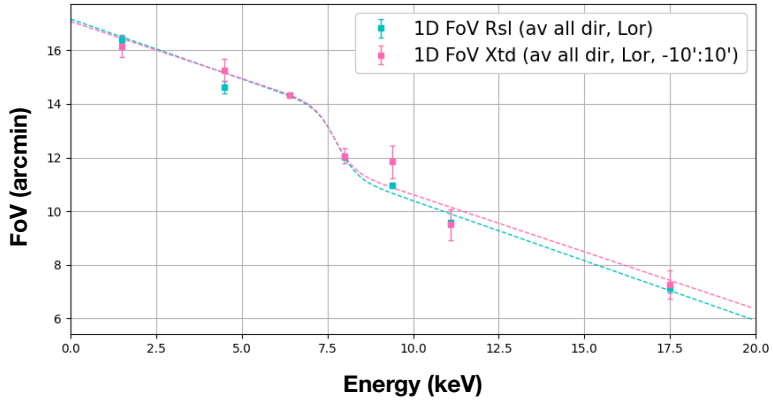

Figure 4.12: Field of View of the XMAs, as a function of energy. The FoV is defined here as the FWHM value determined by fitting the vignetting curves with a 1D Lorentzian model, and does not take the physical size of the detectors into account. The FoV is the average value of the FWHM in all directions. The data points are from the ground measurements.

both mirrors, the measured HPD is found to be better than the 1.7′ requirement (Tamura et al., 2022). The typical error of the angular resolution is about 0.01′ in HPD, based on statistical error, uncertainty in the position of the center of the image, and the fluctuation of the CCD background. The angular resolution of the Resolve-XMA is about 0.1′-0.2′ better than that of Xtend-XMA at all energies.

Table 4.4: The HPD obtained at seven energies. From Tamura et al. (2022)

Energy [keV]	1.49	4.50	6.40	8.05	9.44	11.07	17.48
Resolve-XMA [′]	1.29	1.30	1.30	1.28	1.22	1.19	1.24
Xtend-XMA [′]	1.47	1.46	1.47	1.47	1.40	1.37	1.37

4.2.5 Stray Light

Stray light designates X-rays that enter the detector via a path other than the normal double reflections. It includes the case of a single reflection on either reflector, a reflection on the back side of the reflectors, or a reflection on the pre-collimator blade. The pre-collimator significantly reduces the amount of stray light (as seen in 4.1.2), but it also causes slight stray light. Stray light that can occur in a multi-nested thin foil optic was discussed in detail by Mori et al. (2005). Figure 4.16 shows the stray light images at 1.49 keV obtained at 30′ and 60′ off-axis angles at an azimuthal angle. In both images, the X-ray source is positioned on the right side. This is the same stray light structure reported for the *Hitomi* SXT mirrors (Iizuka et al., 2018). The 30′ off-axis image has a component biased to the right side of the image, while in the 60′ off-axis image there

is stray light spread over the entire detector. The stray light seen on the right side of the 30′ off-axis images is due to the reflection of the pre-collimator, while the extended component is mainly due to the reflection on the backs of the reflectors. We note that the direct component coming through the gap between the inner wall of the housing and the innermost reflector reported for *Hitomi* SXT Mirror (Iizuka et al., 2018) is not seen in XMAs, because bare aluminum foil was added inside the innermost reflector to removes the direct incident component (Tamura et al., 2022). The main contributions on the measured stray light for XMAs are probably due to pre-collimator reflections. The amount of stray light entering within an 8′ radius, converted to effective area, is shown in Table 4.5 as well as the amount of stray light entering the Resolve detector. We note that the flux of the stray depends on the azimuthal direction of the incident photons, and the values in Table 4.5 are instances. The detailed analysis of stray light will be performed with the in-flight calibration data. However, expected stray light effects will not be large based on *Suzaku* observations. Therefore, proposers are not expected to consider stray light contamination on their targets when planning proposal submissions.

Table 4.5: The effective area at 1.49 keV for off-axis sources due to stray light. From Tamura et al. (2022)

	Resolve-XMA (r<8′)	Resolve-XMA (Reslove FoV)	Xtend-XMA (r<8′)
30′ off-axis [cm^2]	0.26 ± 0.01	0.007 ± 0.001	0.16 ± 0.01
60′ off-axis [cm^2]	0.18 ± 0.01	0.009 ± 0.001	0.11 ± 0.01

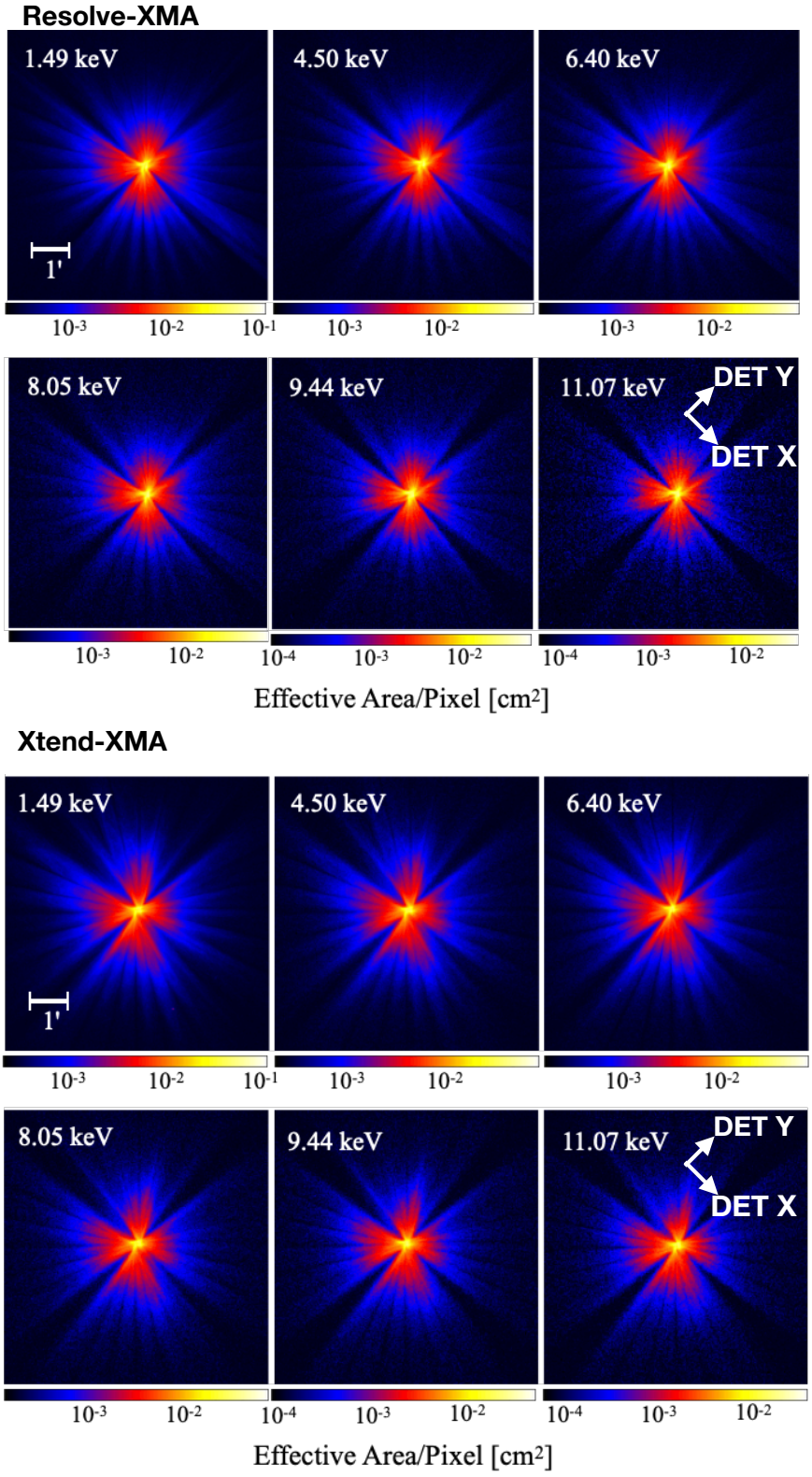

Figure 4.13: Focal plane images of Resolve-XMA (top) and Xtend-XMA (bottom) at the six energies of 1.49, 4.50, 6.40, 8.05, 9.44, and 11.07 keV (Tamura et al., 2022). The image size is $6.7' \times 6.7'$.

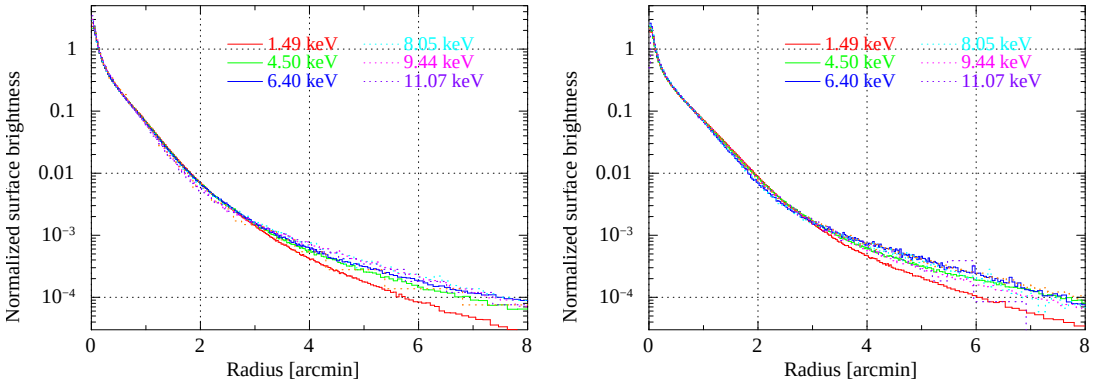

Figure 4.14: One-dimensional PSFs of Resolve-XMA (left) and Xtend-XMA (right). The six PSFs at 1.49 (red), 4.50 (green), 6.40 (blue), 8.05 (light blue), 9.44(violet), and 11.07 keV (dark blue) are plotted (Tamura et al., 2022). These plots are based on the ground measurements.

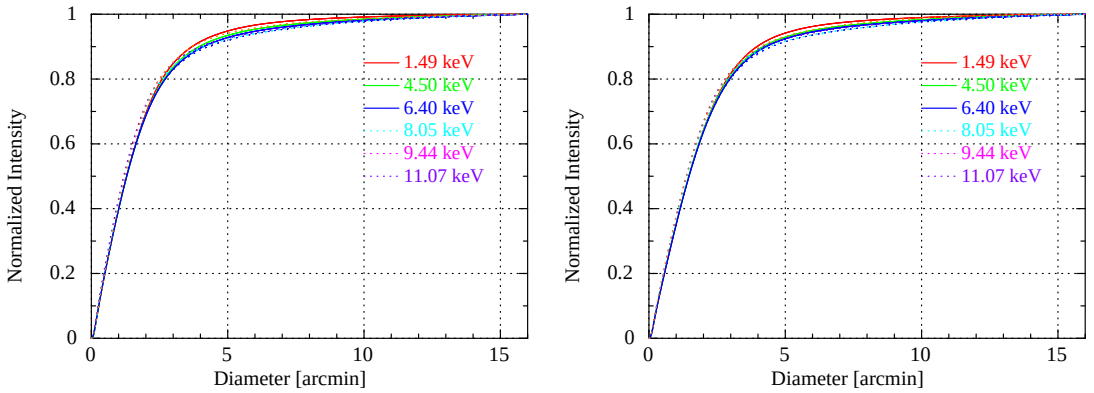

Figure 4.15: The EEF of the Resolve-XMA (left) and the Xtend-XMA (right). The six EEFs at 1.49 (red), 4.50 (green), 6.40 (blue), 8.05 (light blue), 9.44 (violet), and 11.07 (dark blue) are plotted (Tamura et al., 2022). These plots are based on the ground measurements.

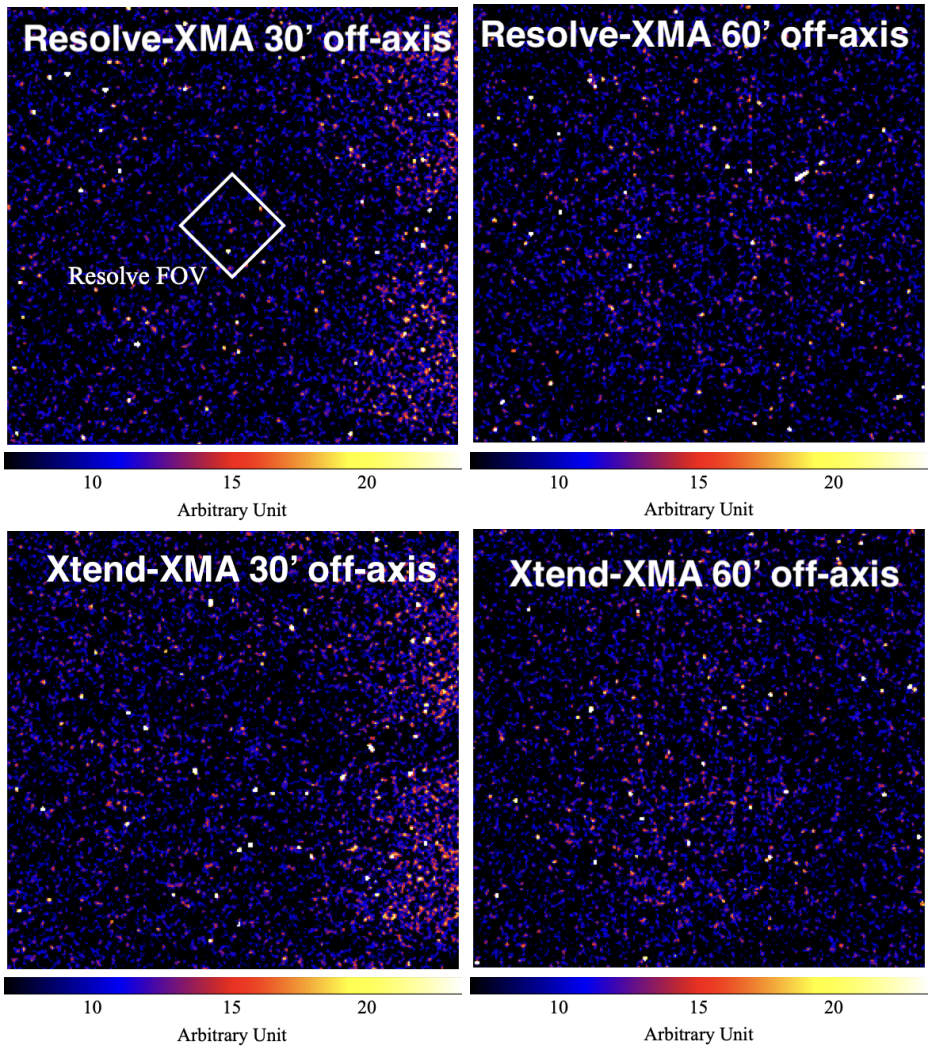

Figure 4.16: Stray light images of Resolve-XMA (top) and Xtend-XMA (bottom) at 30′ off axis angle (left) and 60′ off axis (right) (Tamura et al., 2022). The X-ray energy is 1.49 keV. The image size is 17.8′ ×17.8′. The FOV of Resolve is shown in left top panel.

Chapter 5

Resolve

Resolve is a high resolution X-ray imaging spectrometer with a $3' \times 3'$ field-of-view. It consists of X-ray focusing mirrors (XMA, Chapter 4), and a 36-pixel X-ray calorimeter system (XCS) with better than 5 eV resolution over much of the 1.7-12 keV energy band, according to the initial in-orbit calibration. An anti-coincidence detector placed behind the calorimeter array enables rejection of particle background events.

Key performance parameters are provided in Table 5.1 and an overall view of the Resolve is shown in Figure 5.1. Figure 5.2 shows the effective area of the instrument. The nominal energy range of Resolve is 1.7-12 keV. At low energies, the effective area of Resolve declines steeply due to the closed gate valve ($\sim$0.5 cm^2 at 1.7 keV). At high energies, Resolve is sensitive to photons above 12 keV, even up to $\sim$20 keV. However, calibration becomes less reliable at high energies, and 12 keV is currently the high end of the nominal Resolve energy range.

Resolve is descended from the X-ray Spectrometer onboard *Suzaku* Observatory (Kelley et al., 2007) and the Soft X-ray Spectrometer (SXS) onboard *Hitomi* (Kelley et al., 2016). It is the first microcalorimeter detector that is available to guest observers.

5.1 Overview

Figure 2.2 shows the schematic of the position of the Resolve within the satellite. X-rays emerging from the X-ray Mirror Assembly (XMA; see Chapter 4) pass through a Filter Wheel Mechanism (FWM; cf. Section 5.8.1) mounted 91.5 cm from the detector. The FWM has six filter positions: two open, one with ^{55}Fe calibration source, two for X-ray attenuation to reduce the flux incident on the detector, and one with a polyimide filter. Not all filters are available to observers (cf. Section 5.8.1). Modulated X-ray Sources (MXS; cf. Section 5.6), mounted on the filter wheel axis beyond the FWM with respect to the path of X-rays, serve to calibrate the detector gain. The filter wheel position is

Table 5.1: Summary of the expected Resolve detector properties based on the ground calibration. HPD stands for Half Power Diameter.

Parameter	**Expected**
Lifetime	Goal: 5 years
Energy range	1.7-12 keV
Effective area	$\sim$ 180 cm^2 @6keV
Angular resolution	1.3′ HPD
Energy resolution	5 eV (FWHM)
Energy-scale accuracy	0.5 eV
Line-spread function accuracy	Goal: 1 eV
Pixel size	30"×30"
	818 μm× 818 μm
Field of View	3.1′ × 3.1′
Array format	6 × 6
	35 science pixels
	1 calibration pixel
Relative timing accuracy	80 μs for high- and mid-res events
Operating temperature	50 mK
Maximum X-ray count rate	200 counts s^{-1} array^{-1}
Residual background	0.8×10^{-3} counts s^{-1} keV^{-1}

user-selectable, while MXS is not.

Beyond the FWM, the X-rays go through the aperture door (i.e. the closed gate valve) and then enter the dewar (a cryogenic vacuum vessel where the microcalorimeter array and anti-coincidence detector reside) through five thin-film filters, each staged at a different temperature, before reaching the detectors. These filters help isolate the cooling system from the ambient environment and attenuate the flux of IR photons (thermal radiation from warmer structures) and UV/optical photons (from the sky) that reach the detector. The optical blocking filters in the dewar are fixed in place. The transmission curve for the full five-filter stack is shown in Figure 5.3.

The microcalorimeter detector array, along with the anti-coincidence detector, is housed within the Detector Assembly and maintained at its operating temperature of 50 mK by a multi-stage cooling system with a temperature stability better than 2.5 μK, and with efficiency >95% for more than three years. This low operating temperature and its stability enables the detector to attain its required energy resolution. The cooling system is designed with redundant features to be tolerant to some failure cases and to enable operation of the detector beyond the nominal three-year lifetime.

Analog signals from the Detector Assembly are amplified and digitized. The digitized signal is sent to the Pulse Shape Processor (PSP), which detects X-ray events from the data stream and applies an optimal filtering algorithm to determine the pulse heights of

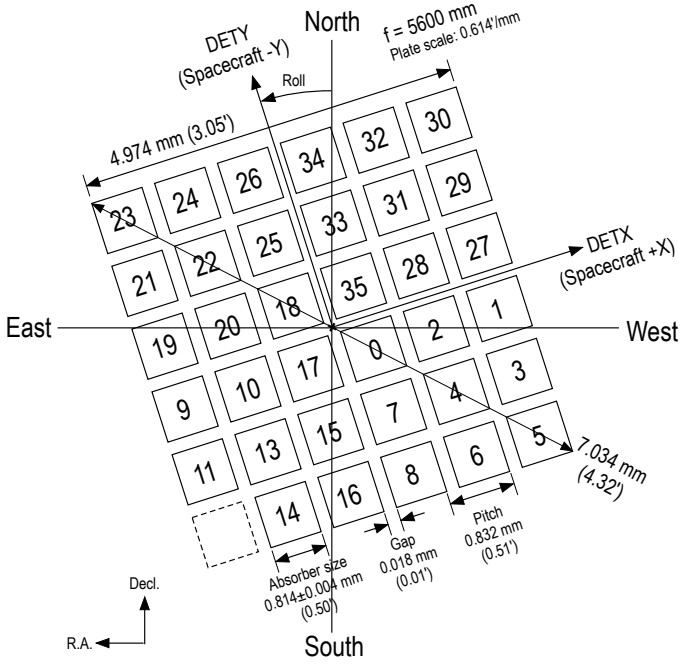

Figure 5.1: A schematic of the Resolve microcalorimeter array focal plane. Dimensions shown are the design values, but most actual absorbers were 0.818 mm wide, and the gaps were correspondingly smaller on average.

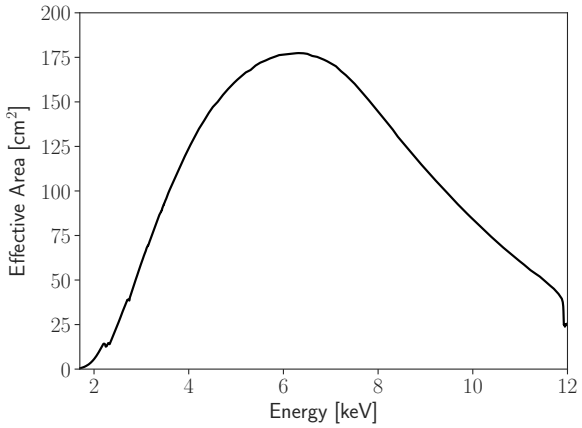

Figure 5.2: Effective area of Resolve, which includes the gate valve transmission (Midooka et al., 2021).

X-ray events. Details of PSP are provided in Section 5.3.1.

The microcalorimeter detector does not trigger on optical events, but is sensitive to optical photons. The absorbed energy contributes to noise, thus degrading the X-ray energy resolution. However, photons outside of the passband are highly attenuated by the

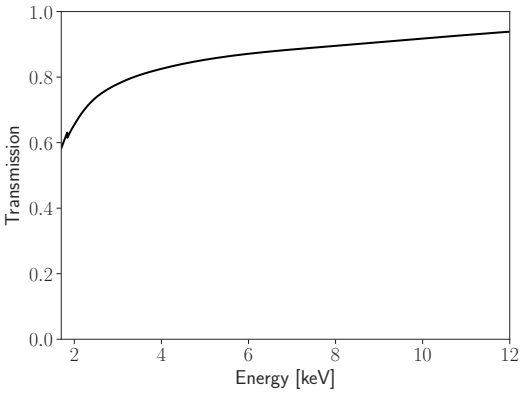

Figure 5.3: Transmission curve for the non-selectable five-filter blocking filter stack.

filter stack, and further by the currently closed aperture door (gate valve), and therefore this effect should not be important.

5.2 The microcalorimeter

The Resolve detects and measures X-rays with a 6×6 pixels X-ray microcalorimeter array (see Figure 5.1). There are 35 active pixels in the main array and 36 readout channels. One corner pixel is not wired and, instead, a calibration pixel out of the field of view used with a continuous, collimated ^{55}Fe source to provide one source of gain tracking for the main array. This pixel is active at all times and is designated as pixel number 12 (in lieu of the inactive corner pixel; cf. Figure 5.1 and Section 5.6).

The pixels are arrayed on a 0.83 mm pitch with a filling factor greater than 96%. Each pixel projects to $0.5' \times 0.5'$ on the sky and the entire X-ray sensitive portion of the array subtends a solid angle of $3.05' \times 3.05'$. It is very important to note that these pixels are **smaller** than the PSF ($0.5'$ pixel vs $1.3'$ HPD). This means that if there are bright sources in and around the FOV or the source is extended, photons from other regions of the sky will scatter into an individual pixel. For more information, see Chapters 7 and 8.

A microcalorimeter detects X-rays using a high-sensitivity thermometer that measures the heat produced by thermalization of photon energy when a photon is absorbed by a low heat capacity absorber.

Since the amplitude of the signal translates into X-ray energy, a microcalorimeter is a single photon detector that measures the energy of every incident photon. By combining 36 independent microcalorimeters in a 6×6 array configuration, the Resolve instrument provides high-energy resolution imaging spectroscopy of point-like and diffuse celestial X-ray sources without the use of dispersive optics Mitsuda et al. (2010, 2014), in contrast to the grating instruments on board of *XMM-Newton* and *Chandra*. Unprecedented energy

resolution is attained at $E > 2$ keV (including the Fe K band) for all sources, and at all energies for extended, diffuse sources such as supernova remnants and galaxy clusters.

5.2.1 Photon detection

The concept underlying an X-ray quantum microcalorimeter detector is based on the measurement of the temperature increase of an isolated thermal mass. The measurement is made using a thermometer in a quasi-static equilibrium with the absorber (Figure 5.4). Thus, the three essential components are (i) an absorber that absorbs the incident X-ray and thermalizes the deposited energy, (ii) a coupled thermometer that measures the temperature increase in the absorber, and (iii) a weak link to a heat sink that restores the absorber to its original temperature. The energy resolution is determined by the precision of the temperature increase measurement against a background of temperature fluctuations.

For an absorber heat capacity $C_{\rm pix}$, thermal link conductance $G_{\rm link}$, and heat sink temperature $T_{\rm sink}$ the absorber temperature increases by $\Delta T_{\rm pix} \approx E_{\rm X-ray}/C_{pix}$ (on the order of a ∼mK for Resolve) upon absorption of energy $E_{\rm X-ray}$ and re-equilibrates to its quiescent temperature with a decay time constant $t_{\rm decay} \approx C_{\rm pix}/G_{\rm link}$. This is illustrated in Figure 5.4.

For Resolve, the rise time for the temperature pulse induced by absorption of an X-ray is on the order of a ms, and $t_{\rm decay}$ is a few ms. However, the detector requires multiple decay timescales to fully re-equilibrate so that for sufficiently bright sources a second pulse may arrive on the tail of a previous pulse. This is explained further in Section 5.3.3.

5.2.2 Anti-coincidence detector and particle background

Resolve is equipped with an anti-coincidence (anti-co) detector. Its main purpose is to reject cosmic-ray events that could be incorrectly interpreted as X-rays. Unlike X-ray photons (which are detected by the microcalorimeter only), cosmic rays trigger events in both the microcalorimeter and the anti-co, and thus they can be identified and removed. Additionally, the anti-co provides an independent monitor of the particle environment. In addition to the advantage of the spacecraft being placed in a low-Earth orbit, a lower and more stable particle background compared to other X-ray missions is achieved thanks to the anti-co.

The Resolve anti-co detector is essentially identical to that deployed in SXS on *Hitomi* (Kilbourne et al., 2018b). It is located directly below the microcalorimeter array, as shown in Figure 5.5. As ionizing charged particles pass through the anti-co, unbound electron/hole pairs are liberated and their drift under the influence of an electric field creates a current that is amplified and measured. Calorimeter events that arise from ionizing particles are flagged for subsequent vetoing as they also trigger a pulse in the anti-co detector. This

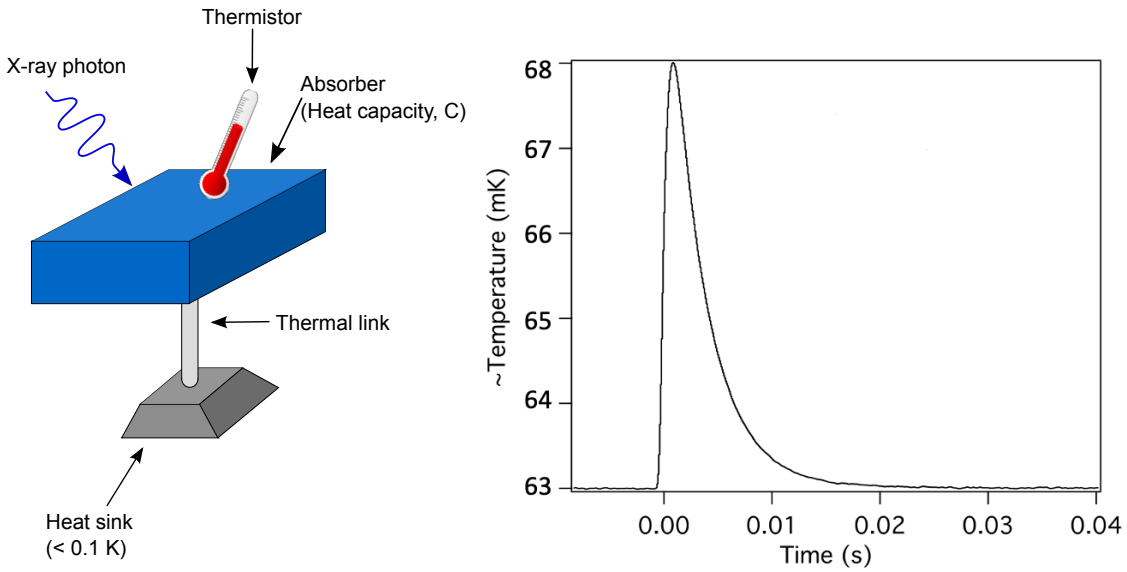

Figure 5.4: The concept of an X-ray calorimeter is shown in the *left* panel, whereby an X-ray deposits energy in an absorber that is measured by a thermometer after the energy thermalizes. Subsequently, the absorber returns to its quiescent temperature and the system is ready to detect and measure the next X-ray. *Right* panel shows a schematic of the temperature of an absorber, which is a part of Resolve pixels, as a function of time. Upon absorbing the photon, the temperature goes up proportionally to the energy of the incident photon, and then goes down with time constant proportional to the heat capacity and thermal link conductivity.

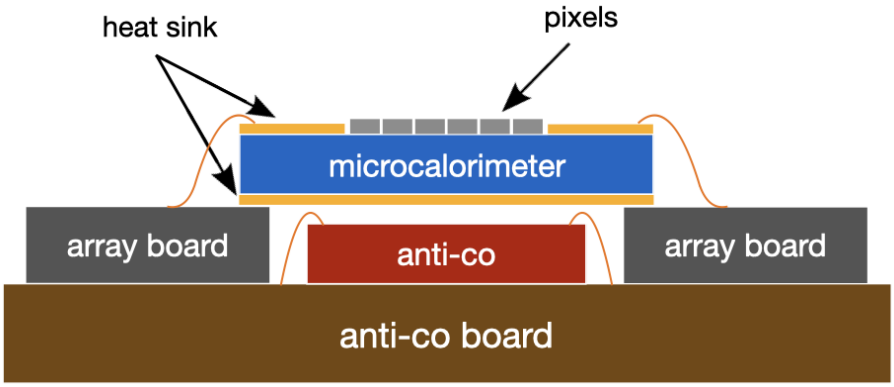

Figure 5.5: Schematic arrangement of the XRISM Resolve microcalorimeter array and the anti-coincidence detector (c.f. Porter et al., 2010). The microcalorimeter array sits on top of the anti-co detector.

way the anti-co detector reduces the non X-ray background.

The anti-co incidence rejection (i.e., removal of cosmic-ray events) is performed on the

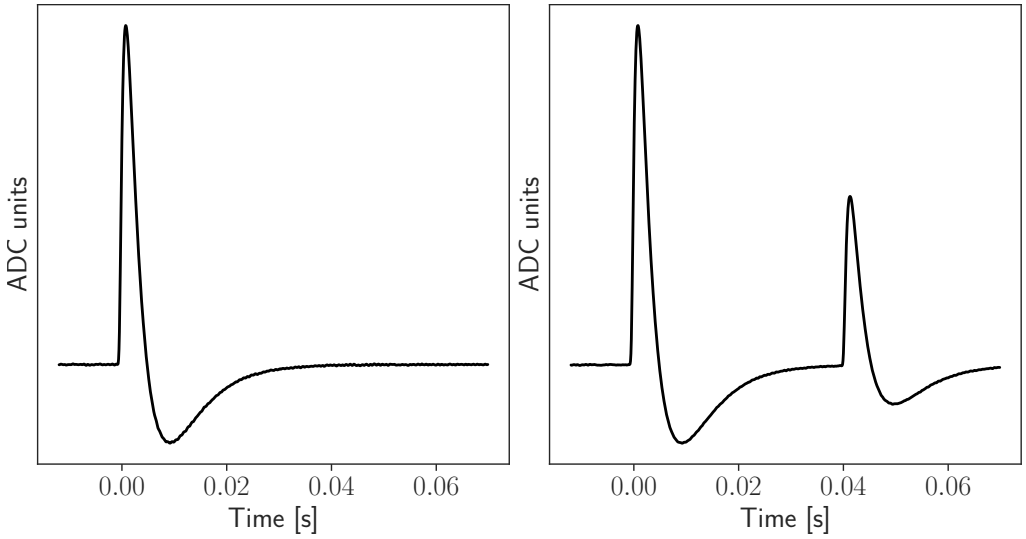

Figure 5.6: Typical shape of a pulse triggered by an incident X-ray. *Left* panel shows a single photon, while *right* panel shows a situation where second photon is detected before the pixel equilibrates after the first event. The undershoot following the pulse happens because the electronics are AC coupled. For details, see Section 5.3.1.

ground as part of pipeline processing, allowing for more flexibility in applying different veto timing windows, as well as the capability to conduct spectroscopic analysis of anti-co events.

5.3 Event processing system

5.3.1 Event triggering

Signals from both the microcalorimeter and the anti-co detector are transferred from the Detector Assembly to the XBOX (X-ray amplifier BOX), where they are shaped (via analog high-pass and low-pass filters), amplified, and digitized. The digitized signals are sent to the Pulse Shape Processor (PSP) for event discrimination, classification, and processing. The PSP triggers on pulse candidates and characterizes them, calculating the pulse heights, arrival times, and other characteristics of each event.

A temperature increase in the microcalorimeter due to absorption of an X-ray leads to a drop in resistance and corresponding drop in voltage across the thermistor. The processing results in a profile where peaks are followed by deep, long undershoots that are a result of AC-coupling in the electronics. When the calculated derivative of this amplitude profile exceeds the threshold, an X-ray event is triggered. The characteristic profile of the amplitude of this drop after shaping and inversion in the XBOX is shown in Figure 5.6.

The PSP calculates a running boxcar derivative of the incoming data stream of each calorimeter channel, and when that derivative exceeds the selected threshold, an X-ray event is provisionally triggered. Then, a search for events occurring after the first event is conducted. To detect second order pulses (pulses arriving during the decay of the previous pulse), the same trigger algorithm is applied to an adjusted derivative profile (Boyce et al., 1999). The adjusted profile is triggered as a second order pulse if the adjusted derivative rises above a threshold and then falls below zero within a specified length of time. The latter condition assures that the second order pulse has the characteristic shape of an X-ray event (Figure 5.6, right panel). The process is repeated to search for third order events, and so on until no further pulses are found.

Anti-coincidence (anti-co) events (cf. Section 5.2.2) are triggered in a similar way to pixel pulse events, but are based on the pulse profile only (and not its derivative). Anti-co events are utilized to flag coincident pixel events for subsequent filtering. Triggering occurs when the sample value exceeds the inter-pulse baseline level by a sufficient amount.

5.3.2 Pulse height determination

To determine the pulse height amplitude (PHA; which, ultimately, is related to the energy of the incident photon), the signal processing by the PSP exploits the approximate energy independence of the pulse profile and energy resolution by employing the optimal filtering method. This requires the construction of a pulse profile template. Cross-correlation of the observed signal with this optimal filter template yields an estimate of the pulse height with the lowest signal-to-noise frequencies filtered out. The details of this method can be found in Moseley et al. (1988) and Szymkowiak et al. (1993).

Since the needed precision of the energy determination of anti-co pulses is much less than for calorimeter pulses, to conserve the computing resources of the PSP, the assigned anti-co pulse height is simply the peak value of the pulse.

5.3.3 Event grading: low, mid, and high-res grades

To assure the highest accuracy of the optimal filter matching (as described in Section 5.3.2) there must be only one pulse per pulse time interval. If this is the case, the highest energy resolution ("hi-res") is attained. If there is a second pulse within that interval, a truncated template is applied, and a lower resolution ("mid-res") is set. If there are multiple pulses within the truncated template the resolution is even lower ("lo-res"), and the pulse height must be estimated from the height of the peak over the baseline. Figure 5.7 shows the difference in these spectral resolutions.

Specifically, the events are graded based on comparing the time difference between neighboring pulses against two limiting values, $\delta t_1 = 70.7$ ms and $\delta t_2 = 18.3$ ms. Hi-res events are those for which pulse height analysis using the full template is possible, i.e. those

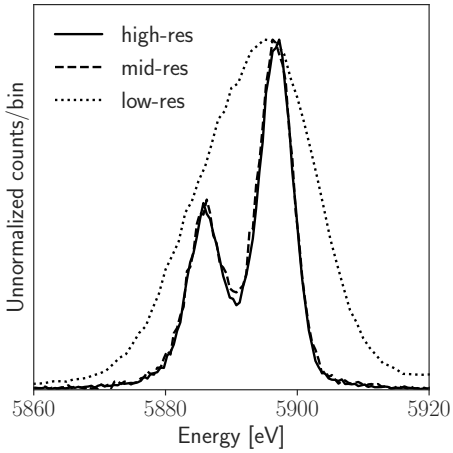

Figure 5.7: Comparison of the fluorescent Mn Ka spectra for different event grades from the Resolve ground calibration program.

with no other detected pulses with arrival times nearer than δt_1. Mid-res events are those for which pulse height analysis using the truncated template is possible, i.e. those where other pulses are detected with arrival times nearer than δt_1 but not within δt_2. If pulses are detected too close ($< \delta t_2$) for the mid-res template, they are classified as low-res.

Events that are separated in time from preceding events by a full template length or more are characterized as primary events, otherwise as secondary events (primary events may then be classified as either high-resolution, mid-resolution, or low-resolution based on the time interval to the subsequent event). Secondary events are those that are preceded by an event within the time interval allocated for a single pulse sample, and classified as mid-res or low-res depending on the time interval to the nearest event using these same criteria.

Because the detector may not be fully re-equilibrated from the energy absorbed from the previous pulse there may be a shift in the gain for secondary events (cf. Section 5.4). For high-count rate sources, there may be a long chain of secondary events associated with a single primary. Finally, if pulses arrive so rapidly that they cannot be individually detected at all, they are measured as a single event with an amplitude equal to the sum of those of the unresolved components. This pile-up will result in a biased spectrum and count rate. Note that this happens only at very high count rates (cf. Chapter 8).

Combining high, mid, and low resolution grades (based on the relative time of the nearest event) with primary and secondary flags leads to the five possible event grade classifications illustrated in Figure 5.8 and shown in Table 5.2. The Resolve spectral resolution requirement applies to Hp and Mp grades (marked in bold font in Table 5.2), though we expect Ms to be very similar.

All detector pixel pulse events are therefore graded as a combination of primary or

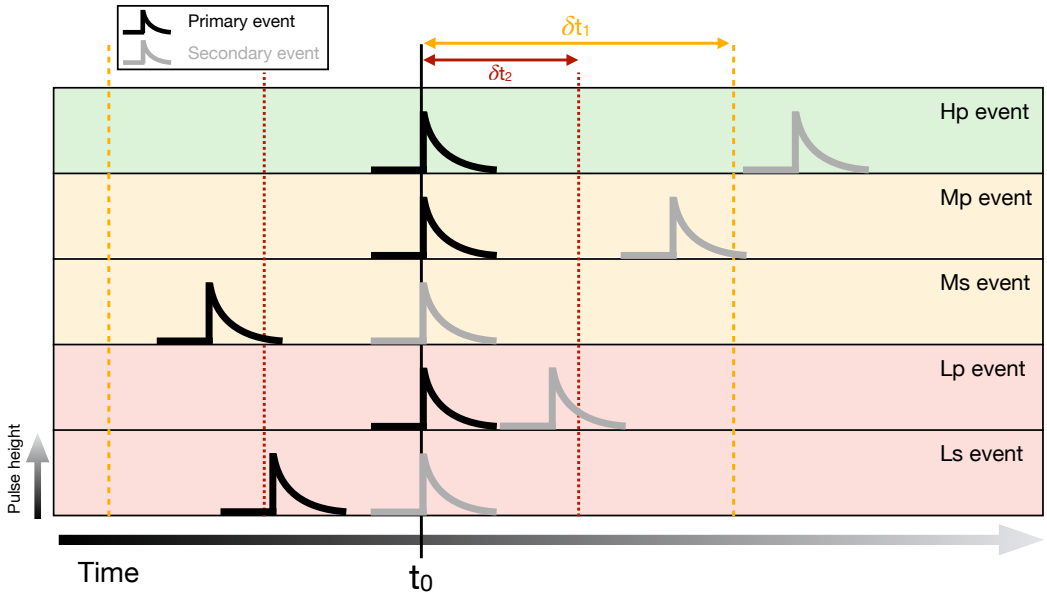

Figure 5.8: Sketch illustrating the grading of Resolve events. The five cases described in the text (high primary, medium primary, medium secondary, low primary, and low secondary) are considered. For details see Ishisaki et al. (2018).

Table 5.2: Definition of event grades. Calorimeter-grade energy resolution is obtainable only for events labeled Hp and Mp, marked in bold font

	$t_p \leq \delta t_2$	$\delta t_2 < t_p < le\delta t_1$	$\delta t_1 < t_p$
$t_n \leq \delta t_2$	L_S	L_S	L_P
$\delta t_2 < t_n \leq \delta t_1$	L_S	M_S	$\mathbf{M}_P$
$\delta t_1 < t_n$	L_S	M_S	$\mathbf{H}_P$

secondary and high, medium, or low resolution – depending on the proximity to adjacent events in time. The event grade provides a measure of data quality.

5.3.4 Event grade branching ratios

The proportion of events in the various event grades depends on the source count rate. The highest-resolution data is only obtainable at count rates that are sufficiently low such that consecutive events are well separated in time.

The branching ratio, defined as the fraction of events that fall into a particular event grade, may be calculated from the template width assuming Poisson statistics. The ratio as a function of the event rate landing on a single pixel is shown in Figure 5.9 for each grade and discussed further in Chapter 8.

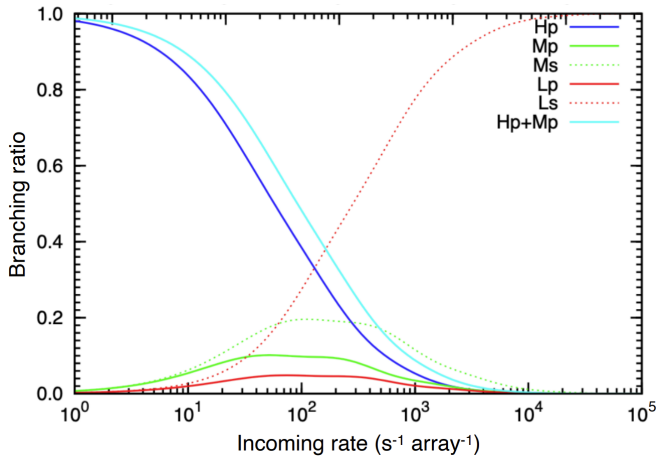

Figure 5.9: The event grade branching ratio is changed by the incoming rate. At low rates, most events will achieve calorimeter resolution (H_p or M_p). For bright sources, resolution is degraded.

As the rate increases, the branching ratio for calorimeter-resolution (i.e., H_P+M_P grade) events declines. The H_P+M_P event rate reaches its maximum of 3.6 events s^{-1} at an incoming rate of about ∼10 counts s^{-1} $pixel^{-1}$.

5.3.5 Pulse Shape Processing limit

There is a limit to the number of events that can be processed by the PSP in a given time: count rate of ∼200 s^{-1} $array^{-1}$. When the count rate is high and this limit is exceeded, some pulses will not be processed and dead time arises. The dead time can be calculated by the PSP telemetry and should be carefully taken into account.

The computational load is the limiting factor for the PSP to process high-count rate sources, the limiting rate depending on the event grades. Choosing an appropriate filter may help increase efficiency of calorimeter-grade events (see Section 5.8.1).

5.3.6 Cross-talk

Electrical and thermal cross-talk can cause further degradation of the energy resolution. Electrical cross-talk in practice is only a concern between nearest-neighbor electrical channels. Most electrical cross-talk from in-band X-rays is not triggered, but these un-triggered pulses can contaminate X-ray pulses. Additionally, the heat flow into the pixel frame from a photon absorbed by a calorimeter pixel or a photon directly absorbed in the frame causes a temperature perturbation, which also contributes to noise at very high count rates. For more details, see Chapter 8.

This cross-talk can significantly impact the energy resolution for high count rate ob-

servations. Ground tests demonstrated energy resolution degradation of a few eV. The energy resolution can be recovered by screening out events that occur simultaneously on electrical nearest neighbors, in which case the cross-talk cut is applied at the price of lower effective exposure time (note that this approach is not applicable when e.g. dead time arises due to a high count rate, cf. Sect. 5.3.5). This was a consideration for the Resolve instrument team in planning the usage of the MXS but it will not be a significant effect for most observations.

5.4 Detector gain

The PSP measures the pulse height of a detected event. This pulse height is then converted into incident photon energy using the detector gain. The latter is determined by the effective temperature of each pixel, which depends on both the heat-sink temperature and radiative loading. The effective temperature is determined by using a reference X-ray line (nominally from the FW ^{55}Fe source and/or MXS) and performing non-linear interpolation between calibration curves taken at different heat-sink temperatures. The gains can be continuously calibrated or interpolated between intermittent assessments, depending on the time scale of the change.

5.5 Line spread function

The Line Spread Function (LSF) describes the response of the detector to a monochromatic beam of photons. A pre-flight LSF has been characterized for each pixel, as shown in Figure 5.10. It consists of a Gaussian core, which dominates up to a level of $\sim$1% for high energies. A minor fraction of events will be redistributed to lower energies in an exponential tail, electron-loss continuum, and escape peaks (Eckart et al., 2018). The LSF depends on the detector noise, and therefore these pre-flight measurements will be repeated in-orbit.

5.6 Calibration sources and MXS operations

Good calibration is critical for a high spectral resolution detector like Resolve. Both LSF (Section 5.5) and gain scale (Section 5.4) need to be regularly calibrated for each pixel. Resolve is equipped with three types of calibration sources to monitor the temporal change of the detector gain in the orbit (gain drift). One is the calibration pixel (cal-pixel, or pixel number 12) that does not receive celestial X-rays but instead is constantly illuminated by a collimated ^{55}Fe radioactive source. Another ^{55}Fe source is mounted on one of the filter positions of the Filter Wheel (cf. Section 5.8.1) and can be used to illuminate the whole array when the position is selected. Mn Kα events at the cal-pixel are always available for

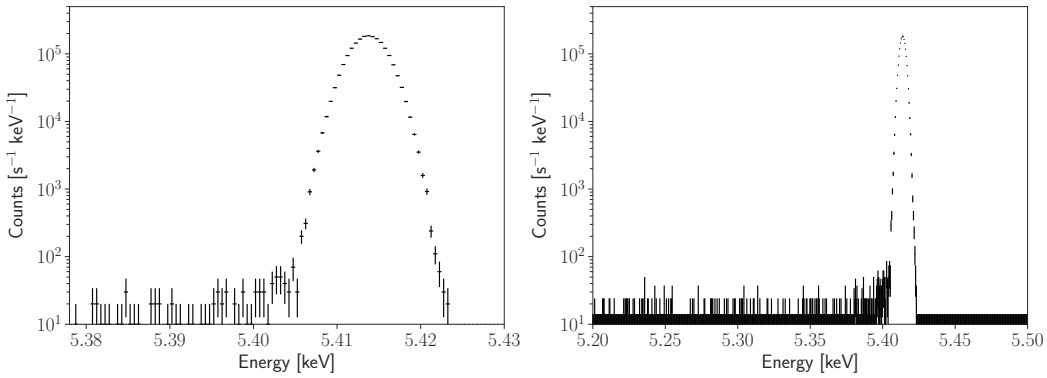

Figure 5.10: Instrument response to a monochromatic emission line at 5.414 keV, demonstrating the Gaussian core which dominates the line shape and the electron loss continuum. For more details, see Eckart et al. (2018)

calibration reference for the overall gain drift of the array (common-mode gain), while the filter wheel ^{55}Fe is useful to monitor the gain drift pixel by pixel (differential-mode gain).

The last type of calibration sources are the Modulated X-ray Sources (MXS), which can be used to monitor both the common and differential gain drift and is not available to observers. Four MXS units are mounted below the Filter Wheel. Two of these are nominal and the other two are redundant. Each pair consists of direct and indirect (fluorescent) sources that emit a set of high-energy X-ray emission lines, mainly Cr Kα at 5.41 keV and Cu Kα at 8.05 keV (de Vries et al., 2018).

5.7 Background

There are multiple contributions to the Resolve background. Astrophysical backgrounds and foregrounds include e.g. the Cosmic X-ray Background (CXB), the Galactic Halo (GH), the Local Hot Bubble (LHB), and Solar Wind Charge Exchange (SWCX). The significance of these components will depend on the position on the sky, on the timing of the observation, and on the target itself (diffuse or not, etc). With the aperture door (gate valve) closed, CXB is the main source of the celestial X-ray background.

The Non-X-ray Background (NXB) originates mainly from secondary particles (mainly electrons and photons) produced by primary cosmic rays that do not traverse the anti-co and X-rays from the calibration sources (scattered from the internal ^{55}Fe source, or the MXS pulse tail). Figure 5.11 shows the NXB measured in-orbit by the *Hitomi* SXS microcalorimeter. The Mn K lines are scattered X-rays from the internal calibration source, and the other lines are fluorescence produced by cosmic rays. These measurements demonstrated that the NXB in microcalorimeter detectors with an anti-coincidence veto is usually very low (Kilbourne et al., 2018a). However, we caution that the NXB can have a non-

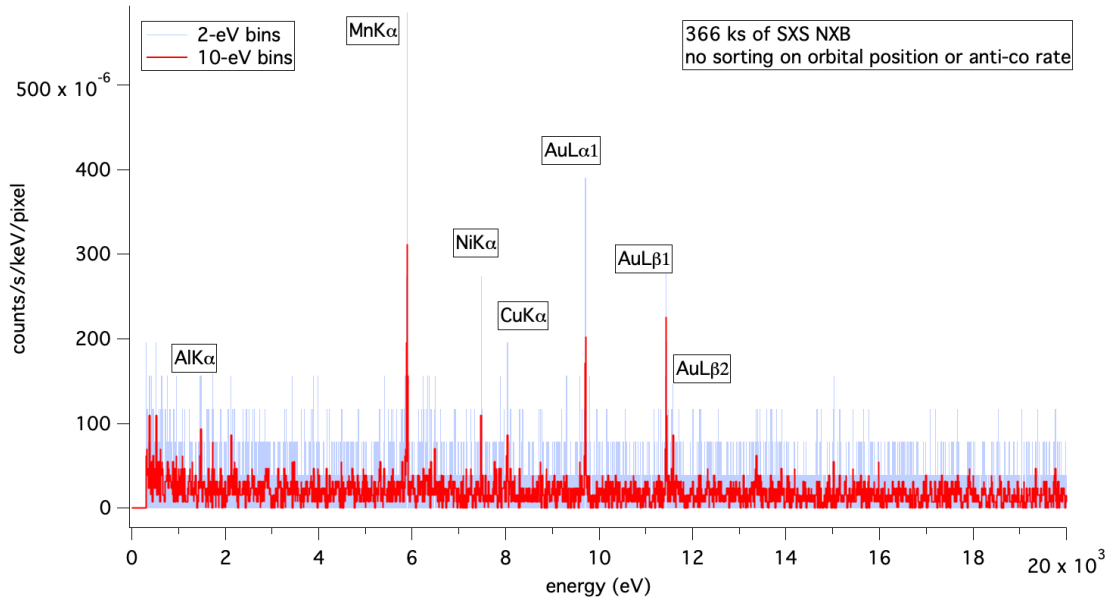

Figure 5.11: Spectrum of the NXB background measured in-orbit in the *Hitomi* SXS microcalorimeter. For details, see Kilbourne et al. (2018a).

negligible impact in a few specific cases (e.g. sources with very faint, diffuse emission).

5.8 Planning observations with Resolve

It is strongly recommended that proposers simulate Resolve observations as part of their scientific justification and feasibility. Special caution must be taken when proposing for extended and bright sources (cf. Chapters 7 and 8). An up-to-date list of simulation tools can be found on the NASA XRISM website[1].

5.8.1 Filter selection

The filter wheel provides a means of selecting a filter setting so as to optimize observations. The filters essentially allow the reduction of flux from bright celestial sources to reduce the detector dead time. The six filter wheel positions include two empty positions (i.e., no filter), a position with radioactive ^{55}Fe calibration source, Be and neutral density (ND) filters for X-ray attenuation, and a polyimide filter. Filter wheel is shown in Figure 5.12 and transmission curves are shown in Figure 5.13.

There are a total of six positions, three of which can be selected by the observers:

[1] https://heasarc.gsfc.nasa.gov/docs/xrism/proposals/

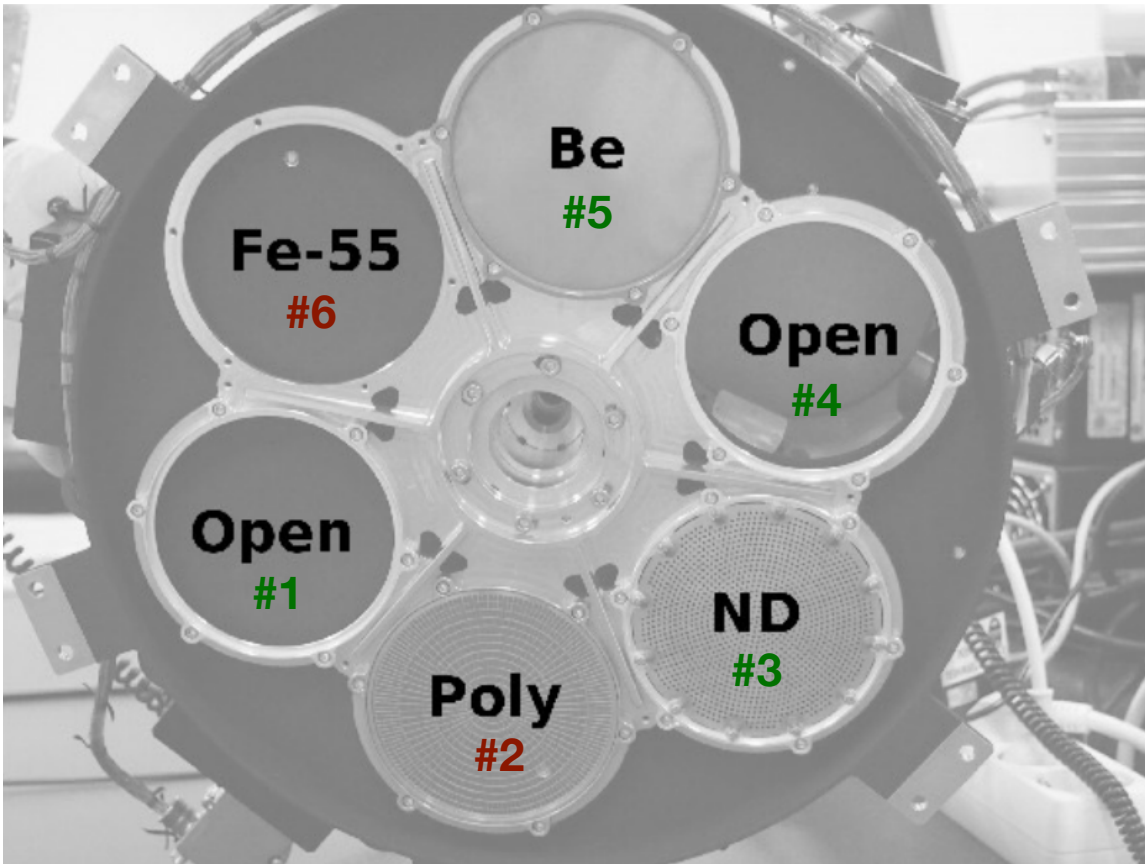

Figure 5.12: Filter wheel filter configuration arrangement, viewed looking up from the detector toward the sky.

- **Positions 1 and 4** are open, filter-less positions. Most nominal observations will be conducted with one of the two open positions.
- **Position 3** has an X-ray Neutral Density (ND) filter consisting of a 0.25 mm molybdenum foil, which blocks 75% of the flux uniformly across the 1.7-15 keV energy band. Molybdenum does not produce fluorescence lines in the Resolve energy band. This filter can be used to reduce the flux of bright sources, therefore improving the efficiency of microcalorimeter-grade events and, ultimately, the spectral resolution (see Sections 5.3.3 and 5.3.5 as well as Chapter 8 for details).
- **Position 5** has a 30 μm Be filter used to preferentially suppress low-energy photons (below 3 keV). This filter maintains both flux and high spectral resolution at the Fe K region.

Positions that are not selectable are:

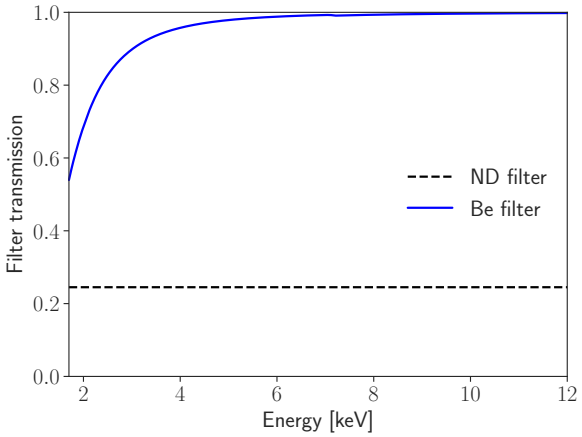

Figure 5.13: Transmission curves for the selectable filters, the Neutral Density (ND) and Be-filter. For filter effective area curves see Figure 8.3.

- **Position 2** has a 200 nm thick polyimide filter, fixed on a stainless steel mesh. This filter is to be used for protection against contamination during the initial phase of the mission only.
- **Position 6** has the radioactive ^{55}Fe sources illuminating the entire array and producing emission lines at 5.89 keV and 6.49 keV. These five sources, all fixed on two perpendicular bars across the FW opening, may be used for in-flight gain and energy resolution calibration, in a manner that is determined by the Resolve instrument team.

5.8.2 Observing faint to moderately bright point sources

To plan an observation of a faint to moderately bright point sources, simple spectral simulation and background modelling is sufficient to determine the integration time necessary to accumulate sufficient number of counts.

5.8.3 Observing extended sources

We refer the reader to Chapter 7.

5.8.4 Observing bright sources

We refer the reader to Chapter 8.

Chapter 6

Xtend/SXI

6.1 Xtend Basics

Xtend is the soft X-ray imaging telescope of *XRISM*, with a pair of an X-ray mirror (XMA) and an X-ray CCD imaging spectrometer (Soft X-ray imager: SXI, Hayashida et al., 2018). Xtend has a larger field of view ($38' \times 38'$) and a low/stable non-X-ray background, ideal for observing diffuse X-ray emission with low surface brightness. The large field of view (FoV) and the finer pixel size ($1.''74$) also provide more detailed spatial information of or around the target, extending the capabilities of Resolve's spectroscopy by evaluating contamination from sources outside Resolve's FoV and measuring the local diffuse background (Figure 6.1). Xtend works in a complementary role to Resolve.

Besides a few improvements, Xtend is almost identical to the Astro-H SXT + SXI telescope system (see Section 6.4.6). Therefore, its publications and archival data should be a good reference for Xtend's performance. This chapter describes the SXI module and the combined performance of the XMA and SXI. Chapter 4 describes the XMA-specific performance, which has an identical design to Resolve's XMA telescope but with a slightly different performance.

The SXI houses four identical X-ray CCD sensors in a 2×2 grid. Each CCD has an identifier, CCD_ID=0−3[1], used for the science and housekeeping data (Figure 6.2). These CCDs are similar to those on earlier or ongoing X-ray observatory missions, such as *Suzaku* XIS, *Chandra* ACIS, and *XMM-Newton* EPIC-MOS. However, the SXI CCDs utilize the p-channel, backside-illumination technology, which realizes a thick depletion layer of 200 μm, with high quantum efficiencies in a broad energy range between 0.4–13 keV. The following list describes the key instrument performance. Table 6.1 also summarizes Xtend's

[1]The instrument team and manufacturer also uses another identifier CCD1-4, which has the same numbering order but starts from 1 (e.g., CCD1 for CCD_ID=0). This document consistently refers to the CCD_ID identifier to avoid confusion.

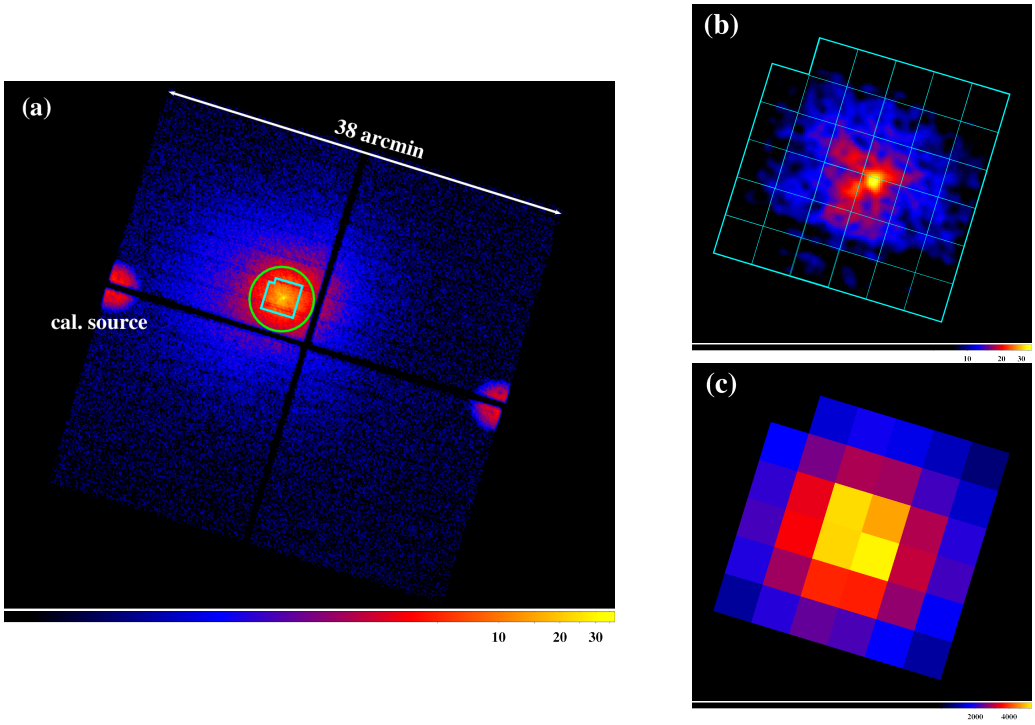

Figure 6.1: X-ray images of the Perseus cluster obtained with the *Hitomi* observatory (Nakajima et al., 2018). (a) Full X-ray CCD (SXT+SXI) image overlaid with the micro-calorimeter (SXT+SXS) FOV in cyan. (b) Magnified CCD image of the central region overlaid with the SXS pixel boundaries in cyan. (c) Micro calorimeter (SXT+SXS) image of the same region.

characteristics.

Table 6.1: Xtend Characteristics

Field of View	$38' \times 38'$ (Full window)
Sensitive band	$0.4 - 13$ keV
Effective area	356 cm^2@1.5 keV, 307 cm^2@6 keV
On-axis XMA PSF at 6.4 keV†	$1.47'$ (HPD), $7.2''$ (FWHM)
Pixel size	$1.74''$ (48μm, logical)
Time resolution	4 sec (Full window), 0.5 sec (1/8 window)
Energy resolution (FWHM)	$\sim$180 eV @ 6 keV
Pileup tolerance	2.5 mCrab (Full window)
Total (NXB + Sky) X-ray background‡	$\leq 10^{-6}$ counts keV^{-1} s^{-1} arcmin^{-2} cm^{-2}

HPD: Half Power Diameter.
†See the XMA chapter (4) for the details.
‡See Figure 6.4 *right* and Figure 18 of Nakajima et al. (2018) for the details.
These values are based on ground or in-flight calibrations.

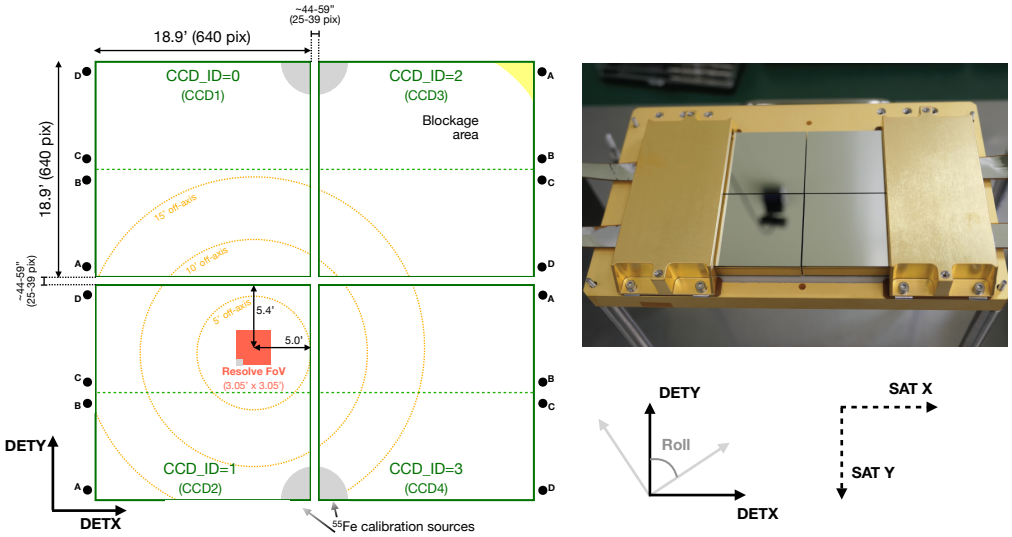

Figure 6.2: *Left* — Schematic layout of the SXI CCDs looking toward the sky from the back of the focal plane. The 4 CCD chips are aligned in a 2×2 format. Each CCD has two electrically separated segments, whose boundary is shown by the dashed line. Each segment has two readout nodes for redundancy (the black dots with the A/B/C/D labels). Each chip has an additional frame store area on the readout node side. The filled gray half circles show approximate areas illuminated by the calibration sources. The red box shows the SXS FOV and the dotted orange circles show the off-axis angles. The distances from the CCD edges are inflight measurement values. There is a tiny area on the far side corner from the aim point shown in yellow, where a camera body structure blocks the view of the sky. *Right* — SXI CCD sensor photo (Nakajima et al., 2020, Fig. 4). Gold-coated metal frames cover the frame store areas.

Field of View: The 2×2 CCD array covers a $38'\times38'$ square FOV with small mechanical gaps between the CCD chips. The gaps between the active pixel regions are $44''-59''$ (1.2−1.6 mm). The aim point co-aligns with the Resolve aim point and offsets by 5 or $5.4'$ from the CCD edges of CCD_ID=1 to avoid the chip gap. In the 1/8 window mode, the 2 CCDs (CCD_ID=0, 1) have a narrow rectangular FOV with the aim point at the width center. The long side does not touch the CCD edges, having a relatively big imaging gap with the other 2 CCDs' FOV (Figure 6.5, Section 6.2).

Sensitive Energy Range & Quantum Efficiency: The SXI CCD sensors have a p-type channel and n-type substrate, enabling a thick depletion layer of ∼200 μm and realizing a large X-ray stopping power up to ∼13 keV. The CCDs are backside illumination CCDs with high transparency to soft X-rays. The SXI system also has the Optical Blocking Layer (OBL) on the CCD surface to block optical/IR lights and the Contamination Blocking Filter (CBF) at the hood top to avoid molecular contamination build-up and further block optical/IR lights. These components limit the soft X-ray sensitivity to ∼0.4 keV. Figure 6.3 *left* shows the SXI CCD quantum efficiency.

Effective Area: This value primarily depends on the XMA's effective area (see Sec-

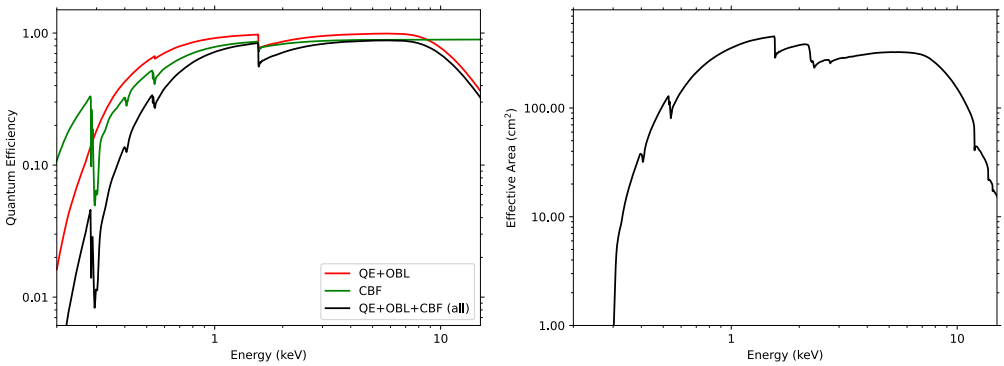

Figure 6.3: *Left* — SXI CCD Quantum efficiency measured with the ground experiments (*black*). The plot also separately shows the quantum efficiency of a CCD chip combined with the transmission of the Optical Blocking Layer (QE + OBL, *red*) and the transmission of the Contamination Blocking Filter (CBF, *green*). *Right* — Effective area of the Xtend telescope, including the XMA component.

tion 4.2.2) and the CCD's quantum efficiency. Beside, the SXI runs with the charge injection operation through the mission, which produces 1−3 insensitive CCD rows every 80 rows and reduces the effective area by 1−3%. Figure 6.3 *right* shows the effective area of the Xtend system for a point source at on-axis. The effective area can decline with radiation damage or contamination condensation in the line of sight. The instrument and science operations teams will calibrate it regularly and update the result in the calibration database.

Angular Resolution: Each CCD has a square imaging area with 1280×1280 physical pixels of 24 μm length each, which are binned by 2 pixels onboard during the science operation. The output science data have 640 "logical" pixels of 48 μm, equivalent to 1.74″ in the sky. This pixel size is significantly smaller than the on-axis PSF's half-power diameter (1.47′) and FWHM (7.2″) (see Chapter 4).

Time resolution: The nominal operation (the Full window mode without the burst option, see Section 6.2) takes a frame exposure for 3.96 seconds and then moves the obtained data to the frame store area in 36.864 milli-second for readout. The imaging area takes another exposure right after this transfer, so, this operation continuously obtains data every 4 seconds. The 1/8 window mode without the burst option runs this cycle every 0.5 sec. The 1/8 window mode with the burst option uses only a fraction of each 0.5 sec exposure. The data-collecting cycle does not increase, but users can use its narrow exposure interval information for pulsar analysis, for example.

Energy resolution: The CCD energy resolution depends on the statistical fluctuation of charges produced by X-ray photons, the number of charges lost during the CCD charge transfer (charge transfer inefficiency: CTI), and the readout electric noise. Normally,

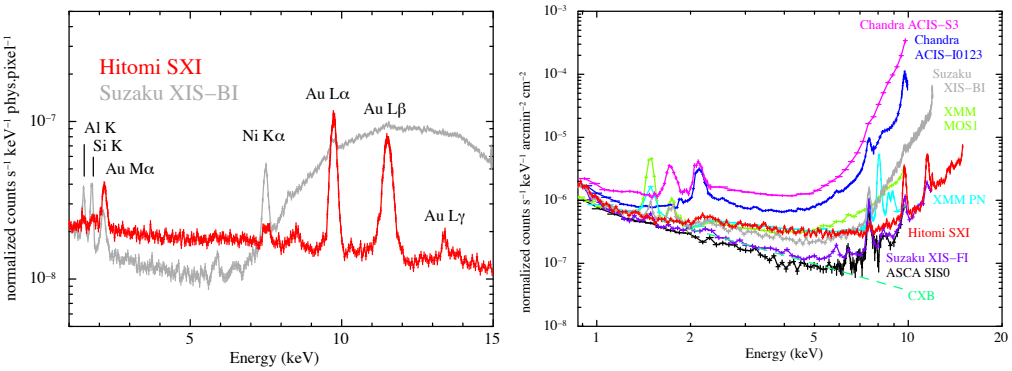

Figure 6.4: *Left* — *Hitomi* SXI NXB spectrum normalized by the physical pixel area. The plot also shows a Suzaku XIS-BI NXB spectrum for the same physical pixel area. *Right* — *Hitomi* SXI total (NXB + sky) background spectrum normalized by the effective area and solid angle of the sky. The plot also shows the CXB spectrum and background spectra of other X-ray CCD instruments (Nakajima et al., 2018).

the first component, charge statistical fluctuation, is the most significant factor in the CCD energy resolution. Higher energy X-rays have worse absolute energy resolution (ΔE) with more charges but better relative energy resolution ($\Delta E/E$) with better statistics. The ground calibration verified the energy resolution of ∼180 eV at 5.9 keV (FWHM). The CTI normally gets worse through the mission with in-orbit radiation damage. The instrument and science operations teams will calibrate the energy resolution regularly with the ^{55}Fe calibration sources and/or celestial source observations and updates the result in the calibration database.

Background: Cosmic Ray (CR) particles or fluorescent X-rays from detector materials excited by those particles interact with the CCD sensors and produce charge clouds in CCD pixels. The grade selection method effectively excludes those events but selected (cleaned) data still include some of them called Non-Xray Background (NXB). The NXB flux changes with cutoff rigidity in orbit, whose distribution varies with the 11-year Solar cycle. (Figure 6.4 *left*, Nakajima et al., 2018). The amount of NXB depends on the exposed duration of each pixel on a CCD and, therefore, the CCD rows (vertical pixel coordinates). The instrument and science operations teams will study the NXB contribution to cleaned data under various observatory environments and provide a tool that evaluates the NXB spectra during individual observations. The sky background contribution is expected to be similar to the Hitomi SXI at 5.6×10^{-6} counts s^{-1} arcmin^{-2} cm^{-2} in the 5−12 keV band (Figure 6.4 *right*, Nakajima et al., 2018).

Table 6.2: Available Window/Burst Mode Options

	N	Image Size (H) × (V)	Time Res. (sec)	Exp. time (sec)	LTF	Pile-up (mCrab)
Full Window No Burst	1	640×640	4	3.9631	0.99	2.5
1/8 Window No Burst	8	640× 80	0.5	0.4631	0.93	21
1/8 Window 0.1s Burst	8	640× 80	0.5†	0.0620	0.12	160

N: Number of exposure in a unit time interval (4 sec).
Image Size: each CCD chip size.
LTF: Live Time Fraction.
Pile-up: On-axis source flux that suffers 10% photon pile-ups, equivalent to an SXI count rate at 6.3 cts s^{-1}.
†Users can measure each photon's arrival time information with ∼0.06 sec accuracy.

6.2 Observation Options for General Users

Users can choose the following optional operation modes for CCD_ID=0 and 1 to observe bright sources and/or improve time resolution (Table 6.2). These two sensors run in the same mode as they share the CCD sequences, while the CCD_ID=2&3 sensors always run with the Full window mode.

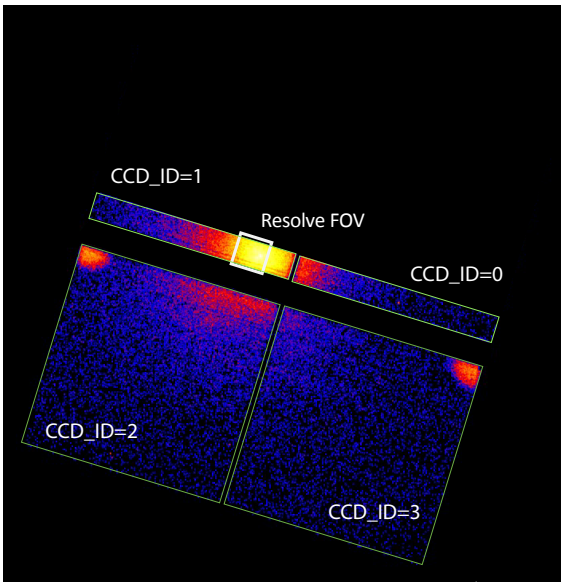

Figure 6.5: Simulated SXI image of the Perseus cluster with the 1/8 window mode. The green boxes show the approximate chip boundaries.

Window option

The window option reads only a divided portion of the CCDs. The guest observer's program supports the 1/8 window option, which reads only 80 CCD rows for one exposure. This operation reduces the readout time to 1/8, so the exposure cadence, and therefore the time resolution, increase by 8 (see Figure 6.5).

Burst option

The burst option collects events obtained during a fraction of the nominal exposure time. This mode reduces photon pileups of bright sources with short-frame exposures. However, it only takes a single exposure in an exposure cycle and trashes events outside of the exposure interval. So, it does not increase the time resolution. The product data have time stamps of the beginning of each exposure so that users can refine photon arrival times for timing analysis. The guest observing program supports the 0.06 sec exposures (12% duty cycle) for the 1/8 window mode.

How to Choose the Observing Mode

Many point sources optimal for Resolve observations would exceed the Full window mode pileup limit. Even some diffuse sources like Perseus cluster, Pup A and Cas A have bright knots that go beyond the pileup limit (see e.g., Figure 3 in Tsunemi et al., 2013). Which Xtend mode should users choose?

The answer depends on the goal of their Xtend observation. If users want to collect photons only from the aim point target as many as possible, they should choose the 1/8 window mode and add the burst option if the target is brighter than ∼21 mCrab. However, the pileup occurs only near the PSF core, so users may be able to utilize data from the extended PSF outskirts with little photon pileups using the Full window mode. The HEASOFT tool, `pileest`, would help estimate pileup fraction from obtained event data.

6.3 Things to Be Considered for Bright Source Observations

6.3.1 Photon Pileup

Two or more X-ray photon events are indistinguishable when they fall in 3x3 CCD pixels in a single frame exposure; such an incident is called photon pileup. Many pileup events have two photons at different pixels, recognized as a multiple-pixel event and discarded, while others are just counted as single X-ray events. Either way, the SXI counts two or more pileup X-ray photons as one or zero, underestimating the photon flux. If detected as single X-ray events, pileup events have an energy of two or more X-ray photons, making

the spectrum harder. The PSF core has the highest count rates per CCD pixel and prone to pileup. The PSF peak diminishes as the source flux increases and turns into a hole in a severe case.

The pileup fraction is the ratio of pileup events over all incoming X-ray events. Xtend SXI reaches the 10% pileup limit at a count rate of 6.3 cts s^{-1}, corresponding to $\sim$4.5 $\times 10^{-11}$ ergs cm^{-2} s^{-1} between 2−10 keV for the Crab nebula spectrum with a power-law Γ at 2.13 (an IACHEC model[2]). Pileup tolerance depends on users' science goals. For example, users should minimize the pileup to detect a weak hard spectral tail, while they may allow some degree of pileups to detect emission lines.

6.3.2 Out-of-Time Events

Out-of-time events are X-ray events detected during the CCD frame transfer — parallel transfer of charges from the imaging area to the frame store area. One logical pixel transfer takes only 57.6 μsec, so only bright sources appear as vertical streaks above the background in images. Out-of-time events rarely suffer photon pileups as detected charges stay in a fraction of time in a pixel, and so can be used for measuring non-pileup spectra of extremely bright sources.

In the normal clocking mode, out-of-time events constitute a uniform brightness streak and contribute only $\sim$0.93% of the total counts from a target. In the burst option, they constitute a significant fraction of the source counts with a relatively long frame transfer interval to the frame exposure, contributing 7.3% of the source count during the exposure.

6.3.3 Sacrificial Charge

Very bright sources create so many X-ray events that their charges also work as fillers of charge traps in the CCD chips (**?**). This effect improves the spectral resolution, but it depends on the source brightness and is difficult to estimate. The instrument team does not plan to implement the effect in the standard calibration.

6.4 SXI in Depth

The following sections describe the detail of the SXI instrument. They may not necessarily be for proposal preparation, but they should help understand how the instrument works.

The SXI sensor (SXI-S) is placed at one of the two XMA's focal plane — 5.6 m below the mirror — on the *XRISM*'s optical bench. The SXI instrument system consists of four components: a sensor body (SXI-S), pixel processing electronics (SXI-PE), digital

[2]https://iachec.org

electronics (SXI-DE), and a cooler driver (SXI-CD). The SXI-S (Figure 6.6) includes the CCDs and their supporting systems, driver and video electronics, a single-stage Stirling cooler, and calibration sources. The SXI-PE extracts X-ray event information from initial image data. The SXI-DE packages X-ray event and associated housekeeping (HK) data and delivers them to the Satellite Management Unit (SMU). The SXI-DE controls the Stirling cooler and associated heater, keeping the CCD sensor's temperature at −110 °C (early operational phase), −120 °C (late phase), or the desired temperature.

Table 6.3: SXI Characteristics

CCD Type	Frame transfer, p-channel, Backside illuminated
Number of CCDs	4
Number of segments per CCD	2
Imaging area	31 × 31 mm^2, 640 ×640 logical pixels (1280×1280 physical pixels)
Pixel size	24 μm × 24 μm (physical pixels)
CCD gap	1.2−1.6 mm (44−59″)
Depletion depth	200 μm
Optical blocking layer	Al(100 nm)/Al(100 nm) deposited on the CCD surface
Contamination Blocking Filter (CBF)	Al(80nm)/Polyimide(200nm)/Al(40nm)
CCD operating temperature	−110 °C/−120 °C
Calibration sources	two ^{55}Fe radioisotopes

6.4.1 X-ray Detection Mechanics and Operation

Hamamatsu Photonics K.K. fabricated twelve flight-model candidate CCD chips, and the Xtend team selected four CCD flight-model chips among them (Yoneyama et al., 2021). The SXI CCDs have a p-type channel and n-type substrate, in which positively charged holes act as mobile charge carriers instead of electrons for earlier X-ray CCD cameras (See Figure 1 in Bebek et al. (2004)). The high resistivity of the n-type substrate produces a thick depletion layer so that the CCDs are fully depleted to the back surface with a depth of ∼200 μm. For comparison, the *Suzaku* XIS backside illuminated CCD with a p-type Si substrate was polished to 45 μm to ensure full depletion. The large SXI CCD depletion depth combined with the backside illumination improves the quantum efficiency at both soft and hard X-ray energies.

The larger depletion depth causes longer drift length and more extensive diffusion. This effect strongly affects soft X-ray photons absorbed near the CCD surface: because the CCDs are backside illuminated, their charges need to drift from near the surface to the bottom with the electrodes. X-ray event charges rarely fall in a single physical CCD pixel (24 μm × 24 μm) but multiple pixels. To simplify the event processing, the SXI nominally combines charges in every set of 2×2 original pixels before the CCD readout and converts

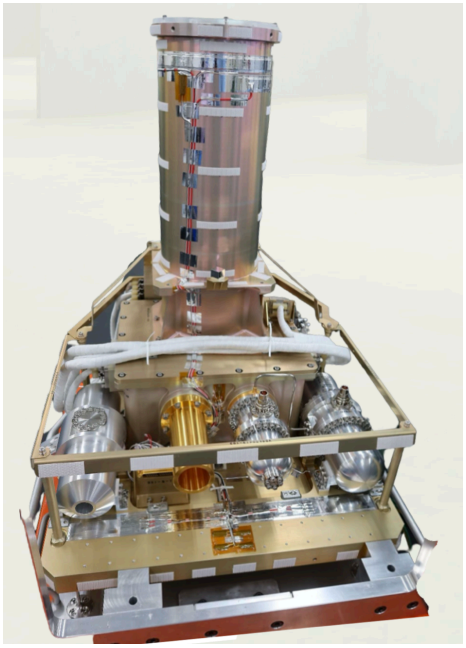

Figure 6.6: External View of SXI-S

them to a digital value. This 2×2 onboard binning format has ∼30% of X-ray events in a single binned pixel, and the rest within 3×3 binned pixels. In the following, the "physical" pixel refers to the original 24 μm × 24 μm CCD pixel, while the "logical" pixel does the 2×2 binned 48 μm × 48 μm, pixel. The SXI science data output in the 640 × 640 logical pixel format for each CCD.

Each CCD chip has a rectangular shape with a square imaging area (IA) and frame store (FS) area. The IA has 1280 × 1280 physical pixels, exposed to the sky through the XMA for X-ray photon detection. The FS also has 1280 × 1280 pixels but is covered with a metal plate and used solely for temporary charge storage. In a normal data acquisition sequence (Figure 6.7), the IA area detects X-ray photons in a frame exposure (3.96 sec in the normal clocking, Full window mode), whose charges quickly drift to the buried channel of the corresponding pixels. After the exposure, the CCD clock driver changes the electrode voltages (so-called clocking) to move the accumulated charges by one vertical pixel at one cycle and repeat this cycle 1280 times to transfer all charges in IA to FS. This "parallel transfer" process transfer all charges in the 1280 CCD columns in parallel. One pixel shift takes 28.8 μsec, and a whole parallel transfer from IA to FS takes 36.9 msec. During each parallel transfer, the SXI also operates charge injection for the subsequent frame exposure (Section 6.4.2 for the detail) so that the parallel transfer duration depends on the charge

injection frequency and the clocking mode

After the parallel transfer, the CCD driver transfers charges in the bottom row horizontally to readouts with two serial registers. A serial register handles a CCD segment, moving charges in the bottom row by one horizontal pixel at one clock cycle toward the active readout node. An analog-to-digital converter measures the number of charges at the readout and stores the value in memory. Once the serial register reads charges in the whole pixels in the horizontal line, the driver vertically transfers all FS charges by one pixel and then read charges moved to the bottom row. The driver continues this sequence until reading all FS charges.

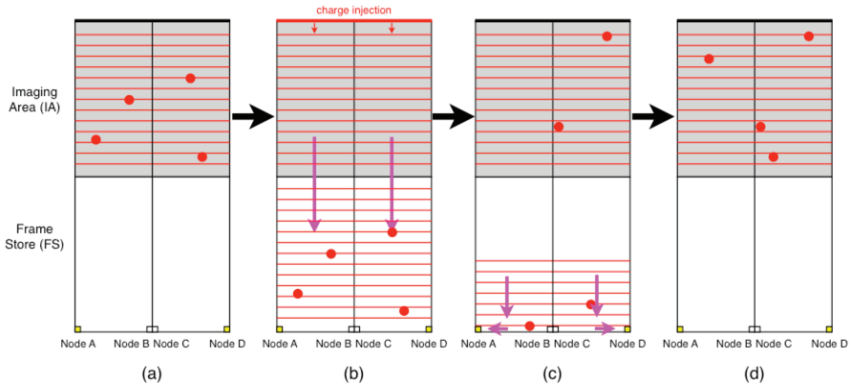

Figure 6.7: Schematic diagram of the charge transfer process on a CCD. (a) At the end of a frame exposure, X-rays or charged particles produce charge clouds around the reacted pixels (red dots). (b) The CCD clock driver transfers the charge clouds vertically to the FS region. It also injects artificial charges to the top serial register every N vertical transfers (N =80 in the prelaunch default setup), which move down to the IA with the subsequent vertical transfers (red lines). (c) Once all IA charges move to the FS area, the CCD clock driver only transfers charges in the bottom FS row horizontally for readout and then moves all FS charges down by one pixel for another horizontal readout. It repeats this process until all FS charges are read out. IA takes another exposure during this readout process. (d) Another charge transfer process begins. The CI spacing and X-ray cloud sizes are not to scale.

6.4.2 Charge Transfer Inefficiency and Charge Injection Operation

Defects in the CCD silicon lattice can hold charges for a short time. If a defect, or so-called trap, is on an electrode, it can capture a portion of charges under transfer and keep them until untrapped charges move to a downward pixel. This process, called charge transfer inefficiency or CTI, occurs stochastically, producing a tail to the original charge distribution and adding noise to the reconstructed event pulse height. The chance of trap increases with the number of pixel transfers, so more charges tend to be ripped off from events detected further from the readout node (i.e., large RAWY coordinates). The SXI chips have relatively large CTIs in the ground testing, and the CTI is expected to progress in orbit as particles continuously bombard CCDs and break the silicon lattice (Kanemaru

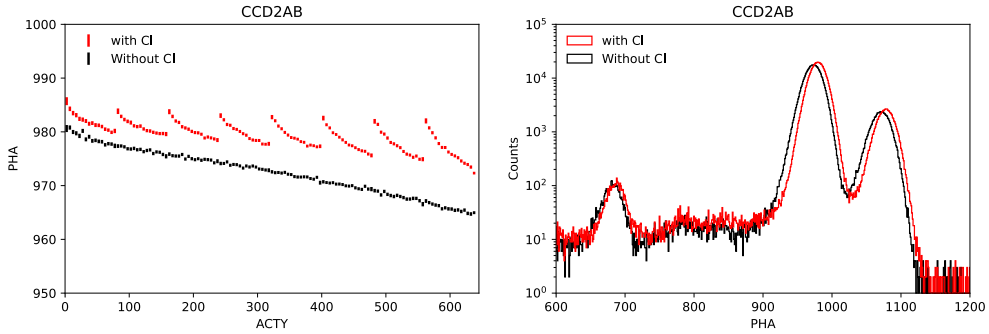

Figure 6.8: Results of a ground test of charge injection (CI) operation in September 2021 with an SXI-S CCD engineering model. In this test, 5 keV charges were injected to the CCD chip by every 80 binned rows. *Left* — Peak Pulse Height (PH) values of Mn Kα source events with/without (*red/black*) CI with the ACTY row, equivalent to twice the number of parallel transfers. CI prevents PH (i.e. charge) reduction. It produces a saw-tooth pattern because it works better on pixels following near a CI row. *Right* — ^{55}Fe radioactive source spectra accumulated from all events on the CCD chip. CI recovers the line energy and the energy resolution.

et al., 2019).

To ameliorate the CTI problem, the SXI employs the charge injection (CI) technique. The *Suzaku* observatory's X-ray CCD camera (XIS) employed this technique for the first time in orbit and substantially improved the energy resolution in the middle of the mission to near the initial performance (see, for example, Bautz et al., 2007; Uchiyama et al., 2009). This technique artificially fills a large number of charges every N CCD row, which fill traps before X-ray events pass the traps during the vertical transfer (Figure 6.7). Figure 6.8 clearly shows that the calibration source spectra improves with the CI operation. A downside is that the CI rows stay in the IA during frame exposures, so these lines, and probably their leading and trailing rows, cannot detect X-rays. This limitation reduces the effective area by $1/N$ or more.

Most trapped charges escape quickly and appear in a few trailing pixels. These charges change the original 5×5 pixel patterns, which is problematic for the grade event extraction classification. This charge migration can be statistically estimated and restored, and so the charge trail correction algorithm runs during the pipeline processing to fix the problem. A small amount of charges reappear outside the 5×5 pixels, causing an artificial pulse height deficit. The CTI correction algorithm in the pipeline processing recovers the expected loss based on the ground and onboard calibration study (Yoneyama et al., 2020).

6.4.3 Hot Pixels

Defects in the CCD silicon lattice can also produce charge currents without X-ray or particle events, which appear as high pulse height pixels called hot pixels. Some hot pixels are permanent, always showing pulse heights above the defined hot pixel threshold. SXI-PE finds such pixels when taking dark frames onboard and flags them as hot pixels. The other hot pixels, specifically flickering pixels, show high pulse heights randomly or occasionally. They may not appear as hot pixels in dark frames, so ground data analysis finds them through statistical analysis.

Strayed optical lights can produce pseudo-hot pixels under pinholes of the optical blocking layer. If the known pinhole pixels have a significant event rate increase in orbit, the instrument and science operations teams will obtain frame images and investigate the cause. The teams do not expect optical light to leak into the SXI camera with the current observatory and instrument designs.

6.4.4 Area Discrimination

If a CCD constantly outputs enormous numbers of events from a very bright source or hot pixels, the telemetry may be unable to handle all event data and lose some onboard. If it occurs, the science operations team may choose CCD areas to downlink to avoid telemetry saturation. This area discrimination setting is not a selectable option for general observers.

6.4.5 Supporting Components

Optical Blocking Layer and Contamination Blocking Filter

X-ray CCDs are also sensitive to optical and infrared lights, which can work as noise for X-ray observations. To block the lights, the SXI CCDs coat the surface with Optical Blocking Layer (OBL), two Al layers 100 nm thick each. OBL blocks optical lights to infrared, while it transmits X-ray emission above $\sim$0.4 keV (Figure 6.3). The OBL has a small number of pinholes of 0.1$-$0.3%, which might produce high pulse height pixels with stray optical lights though the instrument team does not expect such lights come into the camera body. Pixels under the pinholes are flagged and may not be used for science data analysis if they produce significant noise.

The SXI CCD, with an operating temperature of $-110/-120$ °C, is significantly colder than the other satellite components. Adhesive outgases from the satellite body tend to stick to such cold surfaces permanently. The *Suzaku* and *Chandra* observatories had such buildups on the optical blocking filters of their CCD instruments, which significantly reduced the soft X-ray sensitivities in-orbit. The Xtend SXI includes CBF at the hood top, which is composed of polyimide with a 200 nm thickness sandwiched between aluminum

with thicknesses of 80 nm and 40 nm. It blocks outgases from getting inside the SXI body while it is warm enough at about +25 °C at 50 cm above the CCD chips not to build up contamination on its surface. The CBF also eliminates a vacuum-tight chamber and door-opening mechanism (Mori et al., 2022). Figure 6.3 shows the combined quantum efficiency of the CCDs, OBL, and CBF.

Calibration Sources

The SXI has two ^{55}Fe radioactive sources installed into the bonnet for in-flight calibration (Figure 6.6). The sources emit Mn Kα (5.9 keV) and Kβ (6.5 keV) radioactive decay lines to two circular spots on the CCD detector plane (Figure 6.2). The instrument and science operations teams will collect in-orbit data of these lines and measure each CCD chip's gain and energy resolution from their line centroids and widths. The team regularly updates the result in the calibration database so that users can utilize the latest calibration by reprocessing their datasets.

The holder of each calibration source collimates direct radiation to $\lesssim$4.8 mm ($\sim 3'$) from an adjoining corner of two CCDs (Figure 6.2). The ground calibration cannot fully reproduce the in-orbit condition, so that the instrument team will measure the irradiated areas in orbit.

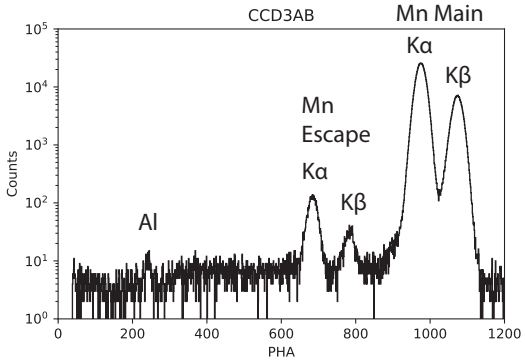

Figure 6.9: 55Fe calibration source spectrum, obtained during the thermal vacuum test in August 2022.

Cooling Systems

A mechanical Stirling cooler removes heat from the SXI's focal plane at a constant rate. The SXI-DE monitors the CCD temperature every second and powers the heater on the backside of the cold plate to regulate the focal plane temperature at $-110/-120$ °C. The CCD temperature was stable on ground EM testing to within 0.1 °C. Such a low-temperature fluctuation helps stabilize the CCD performance and ease the calibration effort if realized

in orbit.

6.4.6 Change from the *Hitomi* SXI

The Xtend SXI is almost identical to the *Hitomi* SXI (Tanaka et al., 2018; Nakajima et al., 2018), but there are design changes to fix the problems found in the *Hitomi* SXI.

Adding a Notch Structure on the CCD Electrodes: The *Hitomi* SXI has a relatively large charge transfer inefficiency (CTI), degrading spectral energy resolution (e.g., Kanemaru et al., 2020). The Xtend SXI CCDs add a notch implant to each channel, whose potential well produces a narrow charge transfer path, reducing the chance of encountering charge traps. With the notch, the Xtend SXI has a factor of 3 smaller CTI than the *Hitomi* SXI. The Xtend SXI also does not show spatial variation in CTI seen in the *Hitomi* SXI.

Coating Additional Al Layer to the Optical Blocking Layer: The optical blocking layer of the *Hitomi* SXI had multiple pinholes with high optical/IR light transmission. When scattered optical/IR lights leaked into the *Hitomi* SXI body, these pinholes produced large pulse height pixels. The Xtend SXI adds a 100 nm thick Al coating to the original 100 nm Al coating on the CCD surface, reducing the number ratio of pinhole pixels from 4.1% to 0.2% (Uchida et al., 2020). This coating, in turn, slightly degrades soft X-ray sensitivity.

Placing an Aluminum Sheet on the Wiring Area: The bonding sheet between the CCD and Si base is transparent to optical lights. When scattered optical/IR lights leaked into the Hitomi SXI body, the lights sneaked in through the bonding sheet, producing pulse height increases of pixels near the CCD edges. The Xtend SXI makes Al coats on the layer of the backside electrode (under the passivation) to block the optical light.

No Openings on the Optical Bench: The scattered lights mentioned above originated from the two openings in the fixed optical bench for the *Hitomi* hard X-ray instrument (HXI). *XRISM* has no openings on the optical bench without the HXI and so expects no incoming scattered light inside the satellite and SXI body.

Shifting the Aim Point: The Xtend SXI's aim point is placed at (8 mm, 8 mm) from the two active pixel edges[3]. These values are larger than the Hitomi SXI values (6.5 mm, 6.5 mm), intended to minimize the portion of the main target's PSF outskirt falling in the chip gap.

[3]The precise values are measured with onboard calibration.

Chapter 7

Observations of Extended Sources

In this chapter, we present the characteristics of *XRISM* instruments that are relevant to the observations of extended sources. In particular, we discuss the possibilities and limitations of spatially-resolved spectral analysis given the imaging performance of XMA and the smaller FOV of Resolve. Careful simulations are often necessary to assess, at a reasonable degree of confidence, whether a particular spatial-spectral analysis objective is achievable.

7.1 Challenges of analyzing extended sources

The non-dispersive high-resolution spectroscopy offered by the Resolve instrument on-board *XRISM* allows one to observe extended sources (e.g., clusters of galaxies, supernova remnants) with an unprecedented spectral resolving power (Chapter 5). Similarly, theses sources can also be imaged and investigated spectrally (though at much lower spectral resolution) using Xtend (Chapter 6). However, the limited spatial resolution permitted by the observatory (as well as the limited number of pixels on the Resolve detector) requires extra caution from observers of these systems.

The two main limiting properties of Resolve are:

- The Resolve pixels are $0.5' \times 0.5'$, i.e. substantially smaller than the PSF ($\sim$1.3 arcmin HPD);
- The Resolve field of view is $3' \times 3'$ (i.e. of size comparable to the PSF).

The Xtend instrument has a larger field of view and, therefore, is not affected by the latter issue. The PSF, however, is caused by the XMA (Chapter 4) and thus affects Resolve and Xtend in the same way.

As a consequence, in both instruments photons from specific regions of the sky are expected to spread over the detector and "contaminate" (more specifically, mix with photons from) other regions. Given that this process occurs at all energies, this mixing will affect the source not only spatially but also spectrally. In the following, we refer to this process as "spatial-spectral mixing" (SSM).

Concretely, and depending on the extent, properties and environment of the source, Resolve can be affected by two types of SSM:

- **Internal SSM**: when the emission within the field of view mixes across pixels and contaminates other regions within the same field of view. For instance, a supernova remnant hosting clumps and/or hot spots with specific spectral features – e.g., bright metal lines – or a complex star-forming region with several spatially-resolved stars. This signal will mix through the entire region covered by Resolve, and one will notice, e.g., an enhancement of the same metal lines in other pixels as well.
- **External SSM**: when sources outside the detector contaminate the detector region itself. One typical example of external SSM would be a pointing of the outskirts of a relaxed galaxy cluster. Another example is the case of a bright AGN located a few arcmin away in projection from any extended source of interest. In the former (latter) case, a fraction of photons from the bright cool core (AGN) leaks into the detector and contaminates the observed outskirts (extended source).

The external and internal SSM are illustrated in Figure 7.1 for the simple case of photons from a single point-like source spreading over the detector. As seen on the figure, due to mirror support structures, imperfect alignments of telescope components, mirror foil figure errors, and non-ideal foil surfaces, the PSF has a complex shape and is not azimuthally symmetric. Particularly in the case of a complex extended structure (e.g., with resolved point sources, clumps and/or hot spots), the PSF effects cannot be seen as a simple Gaussian-like smoothing of an ideal image and should be thus addressed carefully and accurately. The next two figures (Figs. 7.2 and 7.3) focus on a concrete (though very simplistic) case of a circular extended source, half of which is redshifted (V1 = +235 km s^{-1}) while the other half is blueshifted (V2 = −235 km s^{-1}). At first approximation, this is close to what is expected for galaxy clusters with rotating bulk motions of their hot haloes. The spectral effects of the PSF mixing of that specific source are shown in Figure 7.3. Quite interestingly, a mixing of the two components with equal fluxes (e.g., if one looks at central region covering the two components simultaneously) produces a double-peaked line profile, much easier to identify and interpret than the asymmetrical profile seen when one component dominates over the other (e.g., if one looks at a region with one component – though inevitably affected by SSM still).

Generally speaking, the SSM issues described above are somewhat less impactful for Xtend as its PSF (although of similar size as in Resolve) is much smaller than its field

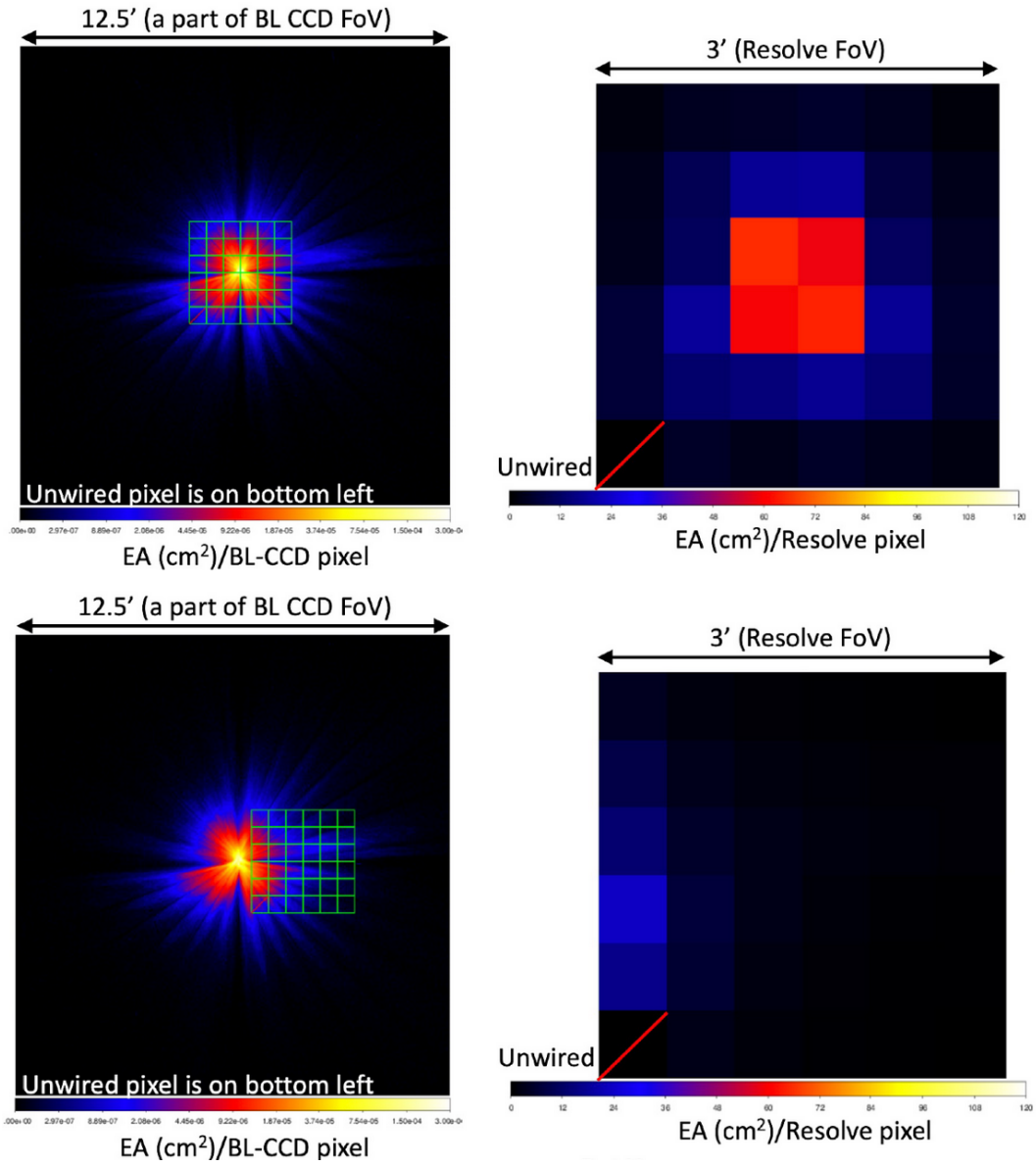

Figure 7.1: Shape of the PSF and its effective impact on Resolve. Top panels: case of a point-like source placed at the center of the field of view (left), translating into significant internal SSM on the Resolve pixels (right). Bottom panels: case of a point-like source placed directly outside of the field of view (left), translating into significant external SSM on the Resolve pixels (right). "BL-CCD" stands for "Beam-Line CCD".

of view. Except in specific cases, a moderately extended source placed on axis of the (large) Xtend field of view will thus make the external SSM less important in comparison,

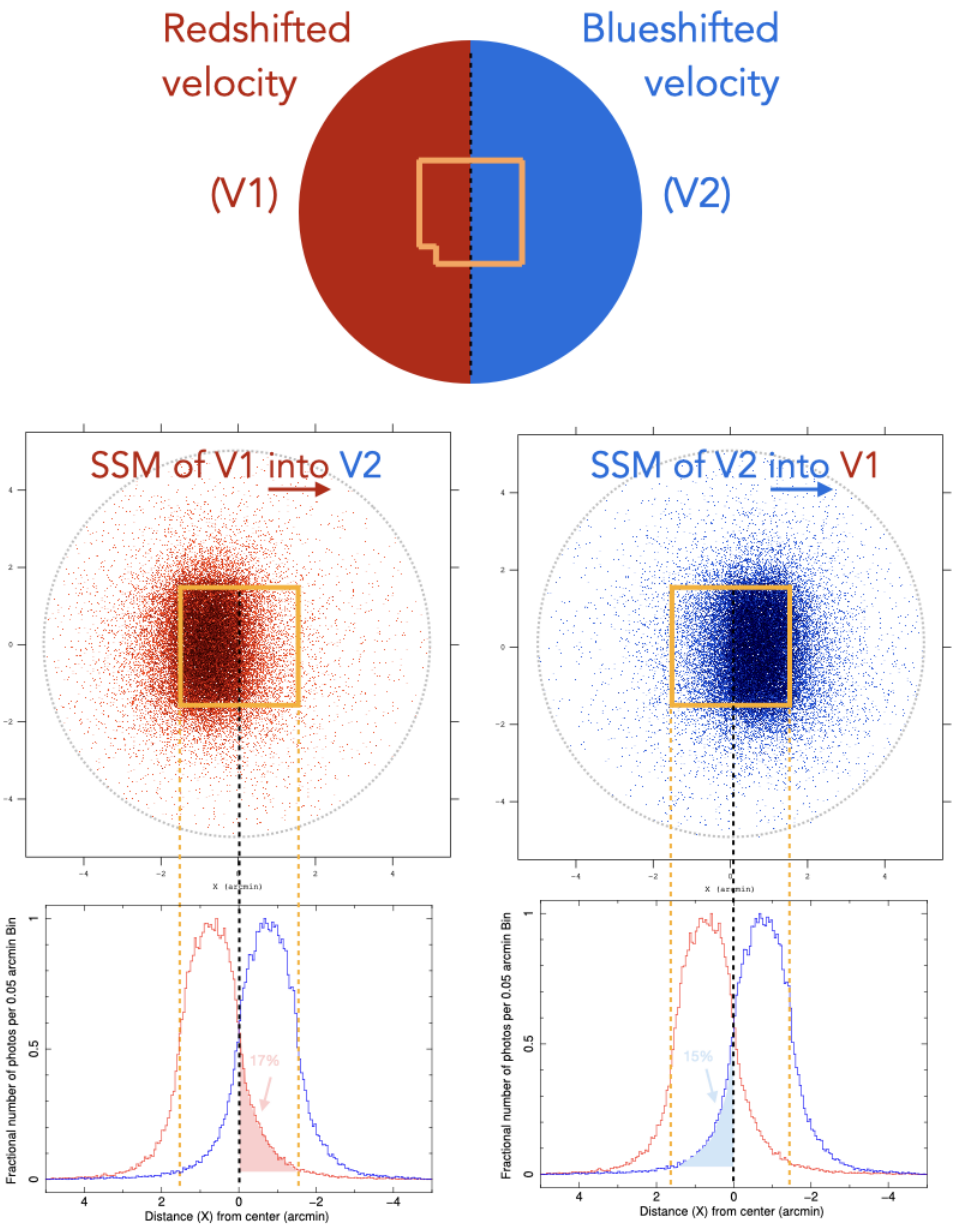

Figure 7.2: Simplistic case of spatial mixing for a circular extended source whose left and right halfs are redshifted and blueshifted, respectively (uppermost panel). The two intermediate panels show, from that region (grey dotted circle), a distribution of all the *incoming* (redshifted or blueshifted) photons eventually reaching the Resolve detector (with yellow square and dashed lines lines indicating the Resolve detector boundaries).The *XRISM* PSF effectively mixes photons from each part into the other, resulting in 15-17% of cross-contamination (two bottom panels, showing the fractional number of photons).

and it will be easier to quantify the internal effects of the PSF mixing within the source. Moreover, the moderate spectral resolution of Xtend means that there will inevitably be less subtle spectral features to be affected by SSM. This, however, does **not** mean that SSM effects can be neglected when analyzing extended sources with Xtend. In fact, variations from e.g., bright emission lines (and/or the continuum) are still important to take into account even at CCD resolution.

The "advantage" of the SSM from Xtend is that the issue is not new. In fact, such effects have affected extended sources in very similar ways in previous missions such as *ASCA* or *Suzaku*. For this problem, we thus refer the proposer to the literature which abound with many concrete cases (for the case of galaxy clusters, see e.g., Markevitch et al. , 1996; Bautz et al., 2009; Bulbul et al., 2016). In contrast, the above-mentioned characteristics of Resolve make (internal **and** external) SSM issues more complicated and relatively unexplored (see however the case of the Perseus cluster observed by *Hitomi*; e.g., Hitomi Collaboration , 2018). The rest of this chapter will therefore focus primarily on Resolve.

7.2 Facing the challenge: methods and prospects

As mentioned earlier, the problem of SSM is *not* completely new, as it has already been encountered to some extent in other X-ray missions – in particular those with a large PSF, such as *Suzaku* and *NuSTAR*. The spectral analysis of X-ray extended sources in those cases is often performed as follows:

1. Subdivide the extended source in various spatial regions of interest (e.g., where spectral features and physical properties may vary);
2. Extract, for each spatial region, a spectrum (S_j) as well as an associated ARF (A_j). In most cases, the same RMF (R_j) can be assumed for all regions as it weakly varies across the detector;
3. Fit each region with a linear combination of models, where each model M_i is associated with each spectrum S_j as follows:

$$S_1 = A_1 R_1 (P_{1\to1} M_1 + P_{2\to1} M_2 + P_{3\to1} M_3 + \dots) \tag{7.1}$$

$$S_2 = A_2 R_2 (P_{1\to2} M_1 + P_{2\to2} M_2 + P_{3\to2} M_3 + \dots) \tag{7.2}$$

$$S_3 = A_3 R_3 (P_{1\to3} M_1 + P_{2\to3} M_2 + P_{3\to3} M_3 + \dots) \tag{7.3}$$

$$\dots \tag{7.4}$$

Under a more generic form, one has:

$$S_j = A_j R_j (\sum_i P_{i \to j} M_i), \tag{7.5}$$

where $P_{i \to j}$ are coefficients corresponding to the relative contribution of the model M_i in the spectrum S_j. In an ideal case with no contamination at all, the $P_{i \to j}$ matrix is in fact diagonal. Even in more realistic cases, many $P_{i \to j}$ terms may be negligible (particularly if regions i and j are more than a few arcmin away), however the SSM will inevitably make several other $P_{i \to j}$ values positive.

To estimate numerically each value from the $P_{i \to j}$ matrix, a tempting approach would be to associate them directly with the normalization parameter of each model M_i in simultaneous fits of all spectra S_j. Such normalization parameters ($N_{i \to j}$) would then be left free in the fits. This method, however, is strongly discouraged for a number of reasons. First, thawing all these normalizations considerably increases the number of free parameters in the fits, with a high risk of reaching strong degeneracies between the latter and/or local minima in the fits. Also, the best-fit values of the free $N_{i \to j}$ coefficients may not reflect the true mixing rate in the considered region (as such normalizations could be biased by other unaccounted uncertainties). In fact, free normalizations between the matrix elements uncouple the problem from the actual telescope and detector, making a "black box" of the whole SSM issue, and will thus likely give artificial results. Such approach should be thus avoided by all means, particularly in the case of Resolve observations.

A much more accurate way to proceed is to determine these coefficients directly by calculating (i.e. via ray-tracing) the contribution of each component from region i into a considered region j. This can be done from the *XRISM* data reduction software by the routine `xaarfgen` (Figure 7.4) which, via its ray-tracing subroutine `xraytrace`, generates an ARF that can be applied directly on a given model M_i. The obtained effective area has been specifically scaled by the routine to account for the exact contribution from region i into region j, meaning that the normalization parameter of each model M_i remains untouched (thus, it conserves its initial physical interpretation). The subroutine `xraytrace` is able generate such ARFs from a geometrically simple input model (e.g., point source, β model) or even an input image; e.g,. taken from *Chandra*/ACIS, *XMM-Newton*/EPIC, or simply from a simulation[1]. Adopting this method, the $P_{i \to j}$ values have their information directly encoded in a grid of ARFs generated specifically for this purpose ($A_{i \to j}$), and the

[1]Despite this being the best feasible approach by far at the moment, it is good to keep in mind that generating an ARF in a local region from an input image has its own limitations. In particular, such an image stands for one specific energy and does not account for the energy-dependency of the extended source. Such systematics can be assessed by reproducing the same exercise with input images obtained from different energy bands. In the case of the Perseus cluster, for instance, the energy dependency of this method using *Hitomi* SXS data was found to be negligible (Hitomi Collaboration 2018, PASJ, 70, 9).

above system of equation becomes then:

$$S_1 = R_1(A_{1\to1}M_1 + A_{2\to1}M_2 + A_{3\to1}M_3 + \dots) \tag{7.6}$$

$$S_2 = R_2(A_{1\to2}M_1 + A_{2\to2}M_2 + A_{3\to2}M_3 + \dots) \tag{7.7}$$

$$S_3 = R_3(A_{1\to3}M_1 + A_{2\to3}M_2 + A_{3\to3}M_3 + \dots) \tag{7.8}$$

$$\dots \tag{7.9}$$

or, under its generic form,

$$S_j = R_j(\sum_i A_{i\to j}M_i). \tag{7.10}$$

In the case of Resolve, it becomes then tempting to follow the same method with, for bright and very extended objects, up to 35 regions (each corresponding to one active pixel on the detector). However, the wealth of spectral information delivered by *XRISM* associated with the complexity of the ray-tracing process used for the mission requires computing resources that may become considerably heavy. In fact, the computing time requested for ray-tracing in the "fast-mode" (i.e. with more limited off-axis accuracy) and extracting a single ARF can easily exceed the hour, making the above approach extremely time-consuming (i.e. on the order of days or even weeks for standard single machines).

Besides the use of distributed/pseudo parallel computing (if available at the user's host institute), a library of pre-computed PSFs (as a function of the energy, off-axis angle, azimuthal angle) will be made available for Resolve after the launch of the mission (likely ready for AO-2). The sum of contributions will then generate a series of fine-grid effective areas for the spectral regions considered. Another alternative to reduce computing times is to focus on a small energy range[2] (if permitted by the science goal) and/or reduce the number of ray-tracing photons. Also, since the SSM is due to the telescope, the ray-tracing code `xrtraytrace` as part of the *XRISM* data analysis software can be used to make SSM estimates by running standalone for single energies. For proposals and/or actual analysis of real data, one can still use the above approximate methods to make an initial assessment of which cross-mixing elements are negligible (e.g,. two regions that are distant from each other). Doing so, the run time for creating the full ARFs is not wasted on ARFs that can be safely omitted.

[2]A single energy is not possible with the current ARF generator, but a narrow energy band is.

7.3 Consequences and general considerations

As we have seen in the previous two sections, the analysis of extended sources with *XRISM* is possible, but challenging. To help proposers evaluate to what extent their science goal is feasible, we provide in this section a list of items and considerations that are important to keep in mind at all stages of the observation – from the proposal to the analysis.

We stress that this list is purely indicative, non-exhaustive, and does *not* constitute a formal checklist for the technical feasibility of any future proposal.

1. It is very likely that the proposers' extended source will be affected by SSM. To estimate how the latter will impact the analysis of the former (and the proposed science goals), it is important to take into account all information on what is known (or unknown) about the spatial and spectral structure of the source. The presence of notable features (e.g., hot spots, blobs, bright nearby AGN or centrally peaked emission), each with their own spectral behavior, will inevitably affect the spectrum of the spatial region(s) to be investigated. Determining how strongly this will affect your science goals and what strategy to use when accounting for this effect will be essential for conducting successful observations.

2. If known to some extent, it is strongly advised to plan a coherent mapping/tiling of the source; i.e. to define spatial regions where pixels are thought to have a (more or less) similar spectral behavior. This also means that, in some cases, the observation should rather be aligned for an optimal match of pixels with spatial features of the source (e.g., to better capture cavities in clusters or shocks in SNRs), rather than simply match the center of the source with the on-axis position of the detector.

3. As the science goal might depend on which region of the extended source (and with which roll angle) the telescope should point at (e.g. if one wants to minimize the SSM in one particular region of interest), it is also important to check the target visibility. This can be done using the visibility checker tool and optimizing the observational position based on the position angle in the observation period.

4. Generating ARFs can be computationally expensive. This is especially true in the case of extended sources, as accounting for the SSM often requires to generate a large number of ARFs. The proposers should keep in mind that several methods exist, some may be more appropriate depending on the proposers' needs and available computing resources (e.g., computing precise ARFs directly, using fastmode, using PSFLib, using an alternative or hybrid method, etc.).

5. A consequence of the previous item is that, although tempting, using Resolve for multi-pixel array spectroscopy is challenging: given that any given pixel is likely affected by the emission from the 34 others, this approach requires the simultaneous

fitting of at least 35x35 = 1225 spectral components[3]. If only one pixel is of particular interest, however, the problem can be considerably simplified by grouping all the others in one common region.

6. The SSM is commonly (and correctly) assumed to happen within the field of view. The external SSM, however, should not be ignored, as its contamination to the investigated sky region(s) can be non-negligible in some cases.

7. Quite counterintuitively, substantial SSM is not necessarily "bad" for the analysis. For instance, a mixing of two components in equal proportions is likely to give rise to spectral features that are easier to spot (and control) than a fainter contamination whose subtle features may lead to significant biases. Specifically, two equally bright regions of different velocities could result in a double-peaked line, much easier to disentangle than a 90-10% mixing resulting in slight (yet significant) line asymmetry.

8. Once the data are retrieved, spectral clues of SSM should rather be investigated by eye before performing a blind fit. Fitting residuals might also provide some clues for mixing (e.g., finding a bump where no line is expected). Similarly, even at the proposal stage it is encouraged to explore the feasibility well beyond a simple setup of `fakeit` and fitting commands in Xspec.

9. The proposers should keep in mind all other systematic uncertainties that may affect the analysis of their extended source. Effective areas, for instance, have their own uncertainties. Those can be of various origins (e.g., calibration, statistical fluctuations in ray-tracing estimates, or even uncertainties related to software algorithms and assumptions). Similarly, other particular properties of the source might, in some cases, further complicate the analysis (e.g., pileup effects – see Chapter 8, uncertainties in atomic databases impacting spectral features relevant to the science goals, etc.).

[3]Taking the external SSM into account, each region requires at least one additional off-detector region. This means that the above number of components fitted simultaneously further increases to $36 \times 35 = 1260$.

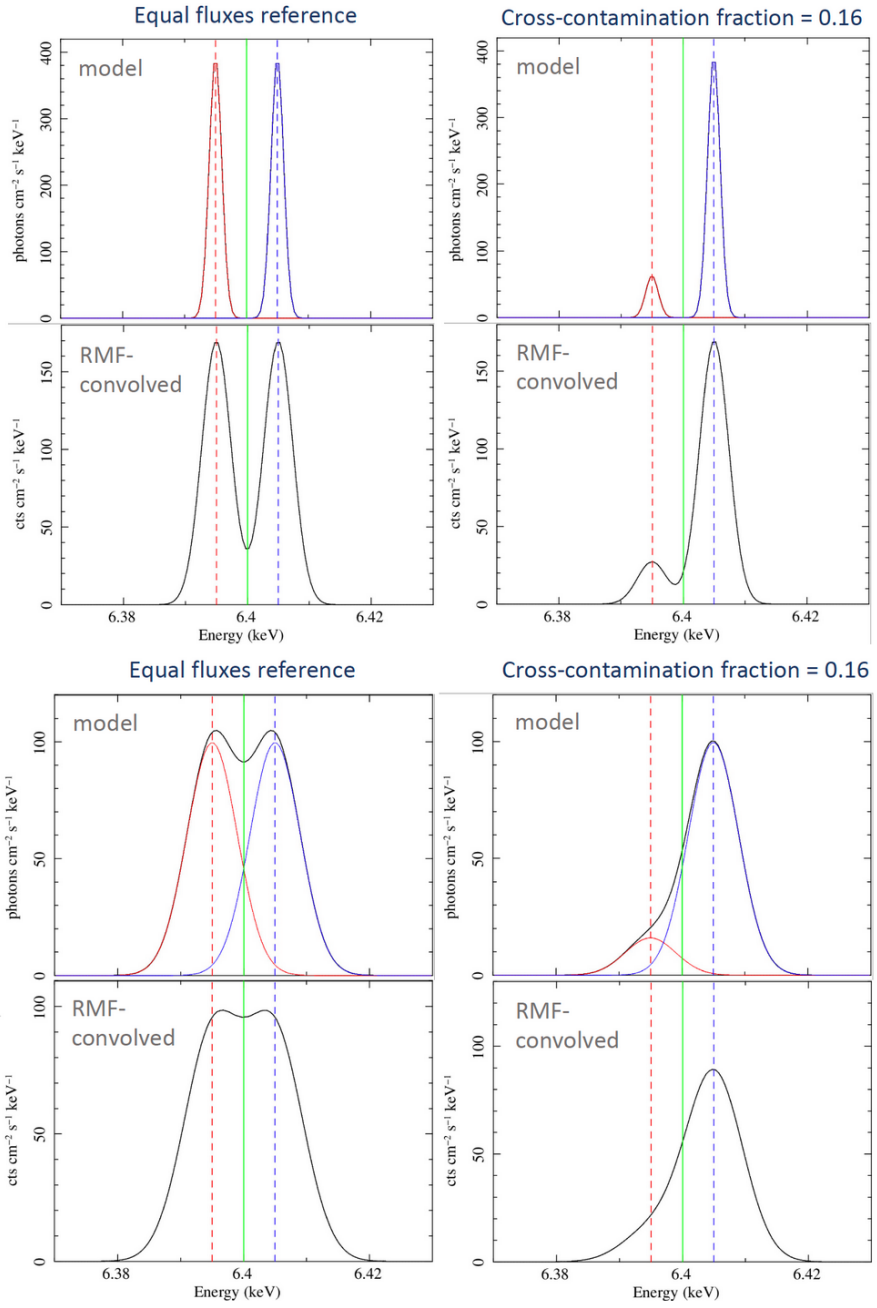

Figure 7.3: Spectral mixing effects on the Fe-K line at 6.4 keV as seen by Resolve, assuming the simplistic case presented in Figure 7.2 (V1 = -235 km s^{-1}; V2 = +235 km s^{-1}). The top four panels assume a line width of $\sigma = 1$ eV (FWHM = 110 km s^{-1}), separating cases for contamination of equal fluxes (left panels) vs. cross-contamination of 16% representing the regions shown in Figure 7.2 (right panels), as well as theoretical models (upper panels) vs. more realistic profiles convolved by the Resolve RMF (lower panels). The bottom four panels show the same effect for a larger line dispersion width ($\sigma = 4$ eV; FWHM = 440 km s^{-1}).

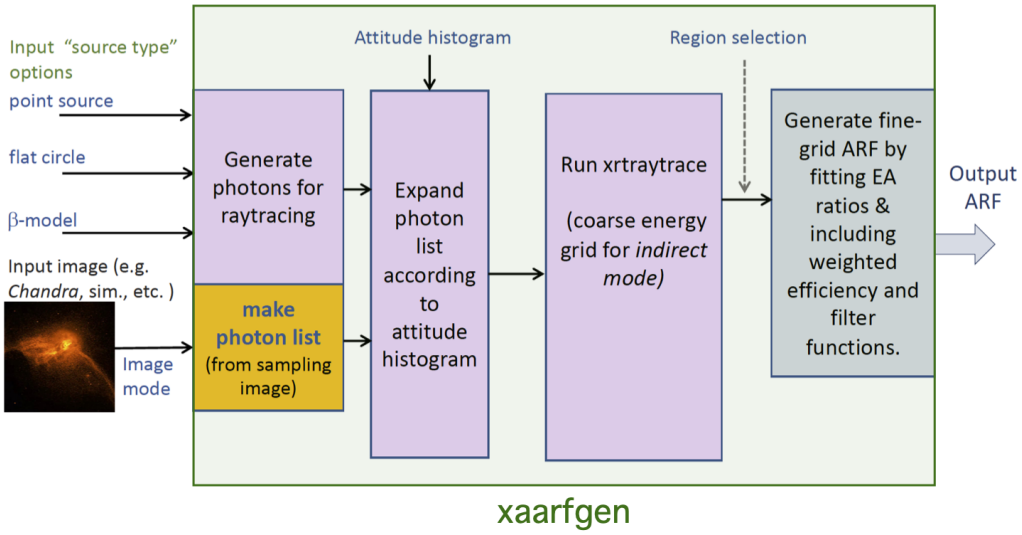

Figure 7.4: Illustration of the tasks performed by the routine `xaarfgen`—and the utility of the latter in computing SSM coefficients for the analysis of extended sources.

Chapter 8

Resolve Observations of Bright Sources

Bright sources, here defined as those that produce $\gtrsim 100$ ph s^{-1} in the Resolve bandpass, are important *XRISM* targets because the high count rate enables precise measurements of variability in emission and absorption lines, as well as detecting weak features at high significance. The X-ray flux that produces a count rate exceeding 100 ph s^{-1} depends on the spectrum, with softer spectra producing greater count rates at a fixed energy, but as a rule of thumb this chapter applies to source fluxes exceeding $0.3-10$ keV $F_{\rm X} > 5\times10^{-9}$ erg s^{-1} cm^{-2}. This flux is equivalent to about 500 mCrab, where the Crab Nebula X-ray flux is defined as $2-10$ keV $F_{\rm X} = 2.4\times10^{-8}$ erg s^{-1} cm^{-2} (Willingale et al., 2001). **Almost all persistent "bright" sources are well-known Galactic compact objects (see `https://heasarc.gsfc.nasa.gov/docs/heasarc/headates/brightest.html`).**

Above this flux, the number of source events (especially high-resolution events) no longer depends linearly on the source flux and exposure time. High count rates can saturate pixels with low-resolution events, saturate the onboard event processor entirely, and degrade the energy resolution due to electrical cross-talk (Mizumoto et al. , 2022). The net impact is fewer clean, high-resolution events than expected for the exposure time. In this chapter, we briefly introduce the challenges posed by very bright sources, then describe observing strategies to maximize the high-resolution event rate, and conclude with general advice on proposing and analyzing such sources. Since the Crab Nebula is the only current *extended* source with a count rate that falls in this regime, observing strategies assume point-like sources.

Any source that can produce $\gtrsim 100$ counts s^{-1} in Resolve will be extremely piled-up in Xtend, for which a "bright" source is about thirty times dimmer ($0.3-10$ keV $F_X \sim 5\times10^{-11}$ erg s^{-1} cm^{-2}). Chapter 6 describes the impact of high count rates on event detection (pile-up and out-of-time events) and the observing modes available to

mitigate issues. For almost any bright source, the optimal Xtend observing mode is a windowed burst mode.

8.1 Challenge: High-Resolution Event Rates

Observers should try to maximize the high-resolution yield, which we denote as Hp+Mp following the convention of Section 5.3.3 (high-resolution and primary medium-resolution events). Section 5.3 describes how events are detected. Section 5.3.3 describes how the Hp+Mp yield depends on total incident count rate in a single pixel based on the characteristic time delay between photons: Hp+Mp increases with total rate up to a maximum and then decreases as the average time delay between arriving photons becomes shorter than the length of the high-resolution optimal filtering template. However, as almost all "bright" sources are point-like, we must also consider the illumination pattern of the Resolve array by the PSF. The total array Hp+Mp rate, $S_{\rm arr,Hp+Mp}$, depends on the total source flux, the shape of the PSF and pointing center relative to the center of the Resolve array, and the source spectrum. $S_{\rm arr,Hp+Mp}$ reaches a maximum of $\approx$100 counts s^{-1} for an on-axis point source with a *Hitomi*-like PSF (half-power diameter of 1.2′) at a total incident rate of 1000 counts s^{-1} on the array.

8.2 Challenge: Event Loss

The Pulse Shape Processor (PSP) cannot process 1000 count s^{-1}; its limit is about 200 count s^{-1} for an on-axis source, assuming that all events processed by the PSP are original source counts (i.e., background events further reduce this). Events beyond this limit are discarded and therefore "lost." The PSP processes events by drawing the next event from a list provided from the event-finding board (a field-programmable gate array, or FPGA). The packet of information from this list includes the addresses of the stored pulse data, so the PSP retrieves the pulse from the buffer and cross-correlates it with a template as described above. The processing time depends on the template length. When processing is complete, the event data is discarded and the energy, arrival time, etc. are sent to the data recorder. If the data buffer fills up before the PSP has processed all waiting events, the entire buffer is cleared and begins to fill up from zero. Hence, at high count rates the PSP can be overwhelmed and events can be lost (but see below).

The PSP houses four CPUs, one for each quadrant of the 36-pixel Resolve array. Each CPU runs an event-processing application for each of 9 pixels so that more than one event can be processed simultaneously. This means that event loss in one quadrant does not necessarily imply event loss in other quadrants, which we will use to our advantage in observing bright sources. When an event from a given pixel is processed, the default behavior of each CPU is to put that pixel in the back of the line and start processing

events from the next available pixel. However, because different event grades take different processing times, a pixel with many low-resolution events can get a higher fraction of its event buffer processed than one with mostly high-resolution events. Averaged over the array, high-resolution events can be preferentially lost.

Resolve does not "pile up" in the same way as CCD imaging spectrometers, but an analogous effect can occur for two events that arrive at almost exactly the same time. When two events are separated by less than a few ms, the secondary event-finding process in the PSP can fail and treat the two events as a single event, thereby misreporting the energy. Several percent of the events can be affected (Mizumoto et al. , 2022), with a concurrent loss of several percent of the exposure time after screening.

Finally, it is important to note that the event-finding algorithm on the FPGA that creates the lists and fills data buffers for the PSP sends information about the number of lost events to the data recorder, so not all information is lost when there is a buffer overflow. The FPGA will not be overwhelmed for almost any conceivable X-ray flux and this information can be used to reconstruct source fluxes (since whether an event is lost or not, or whether it is high resolution or not, does not depend on photon energy). However, without the search for secondary events performed by the PSP, the FPGA count rate is a lower limit.

8.3 Challenge: Minimizing Cross-talk

In addition to event grading and event loss, a third challenge in the high-count-rate regime is electrical cross-talk (Section 5.3.6). Voltage ("parent") pulses in the wire from one pixel induce "child" pulses in neighboring wires (*thermal* cross-talk is an order of magnitude weaker and unimportant). Child pulses have an amplitude 0.6% that of the parent for immediately neighboring wires and <0.1% for next-nearest wires. Due to the wiring map of the array, child pulses are not necessarily induced in physically adjacent pixels (Figure 8.1). Most pixels produce two child pulses per parent, and a few produce only one.

Because of their small amplitude, child pulses are rarely, if ever, detected as events in their own right. However, child pulses make the signal noisier and can lead to significant errors in the energy measured by optimal filtering if they occur at the same time as a real event. Such unhappy coincidences increase with count rate, so cross-talk can degrade the energy resolution of the Hp+Mp spectrum for bright sources. This degradation varies from pixel to pixel, so the total-array degradation is a weighted average. Under ordinary circumstances, cross-talk contamination can be eliminated by ignoring events in electrically neighboring pixels that occur within a few ms of each other. However, for very bright sources the fraction of events that occur within a few ms of each other may be quite high. Strict filtering can eliminate many Hp+Mp events, making the cure worse than the disease.

The impact of cross-talk on scientific analysis depends on the spectrum and the goal.

A hard spectrum at a very high count rate will produce child pulses with larger average amplitudes than a soft spectrum at the same rate, leading to larger errors on the energy. Likewise, if a line of interest falls at 1 keV the fractional error in the velocity resolution will be worse than at 6 keV. The effect can be calculated exactly as a function of count rate for a monochromatic source, but for a more physically motivated spectrum we must calculate it statistically. Figure 8.2 shows the impact of cross-talk for a 4 Crab (2-10 keV $F_X \sim 10^{-7}$ erg s^{-1} cm^{-2}), on-axis point source with a Crab-like spectrum with no filters. The left panel shows the broadening and centroid shift resulting from increased cross-talk contamination for an example Fe Kα line. The right panel shows the average energy resolution (starting from a fiducial 5 eV resolution) in each pixel for this source (note that the most strongly affected pixels are at the array edge but are electrical neighbors of the central four). More examples of the impact of cross-talk on energy resolution are given for simulated spectra in Mizumoto et al. (2022).

Finally, it is worth noting that in *bursty* sources (i.e., those with sharp variations within a single observation) the spectral resolution may degrade during a particularly bright burst. Observers interpreting line shifts and broadening during a burst must account for cross-talk.

Note: The estimates of cross-talk presented here are based on a representative pair of pixels from the Hitomi Soft X-ray Spectrometer. Cross-talk impact can be non-uniform, as it depends on the size of the parent pulse in volts per eV, the strength of the coupling, the interaction of the cross-talk pulse shape with the unique digital filter of the parent pixel, and the gain scale of the parent pixel. As noted above, the incident spectrum also makes a difference.

8.4 Observing Strategies: Filters and Off-Axis Pointing

Degradation of energy resolution due to electrical cross-talk becomes important above 0.3-10 keV $F_{\rm X} \gtrsim 5 \times 10^{-9}$ erg s^{-1} cm^{-2}. Event loss starts to become important above $F_{\rm X} \gtrsim 2 \times 10^{-8}$ erg s^{-1} cm^{-2}. Above these thresholds, maximizing the "clean" Hp+Mp rate (i.e., from pixels where the average cross-talk degradation is no more than 2% the native energy resolution) is achieved by reducing the incident count rate from the default, on-axis value. This can be achieved by using a filter to reduce the effective area (see curves in Figure 8.3) and/or pointing off-axis. The Be filter removes most of the photons below 2 keV and is not useful in the current configuration, while the neutral-density (ND) filter reduces the count rate at every energy by a factor of about four.

Pointing off-axis causes more focused X-rays to fall off the chip and can also be used to concentrate low-resolution events and their attendant cross-talk signals in one sacrificial quadrant, thereby maximizing the clean Hp+Mp rate in the other quadrants. Figure 8.4 shows the results for a Crab-like point source located at the quadrant opposite the calibration pixel. The upper right quadrant is saturated by low resolution events and contributes

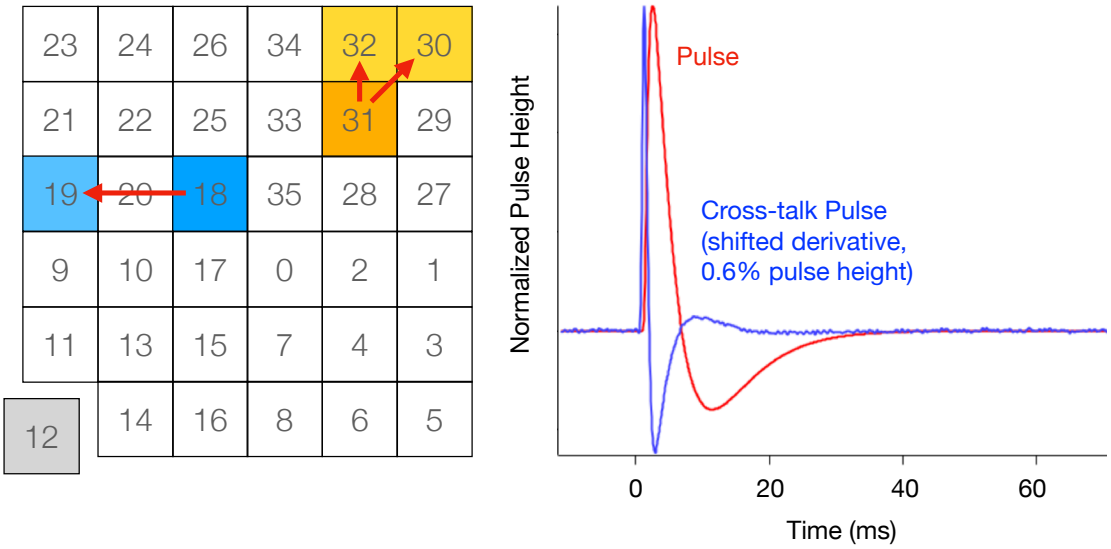

Figure 8.1: Electrical cross-talk "child" pulses occur in *electrically* adjacent pixels, so the cross-talk distribution does not follow the shape of the PSF. Left: Resolve pixel map showing electrically neighboring pixels. A parent pulse in pixel 18 (blue) will produce a child pulse in pixel 19 (light blue), but not in pixel 17 because it is in a different and electrically isolated quadrant. Likewise, a parent pulse in pixel 31 (orange) will produce child pulses in both pixels 30 and 32. Right: Cross-talk pulses (blue) have a shape based on the time derivative of the parent pulse (red) and a much smaller signal, with a peak amplitude of 0.6% of the pulse height. The child pulses are superimposed on the data stream in their pixels; when a child pulse in pixel 19, induced by a parent pulse in pixel 18, occurs around the same time as a parent pulse in pixel 19, the pulse shape is distorted. This leads to an erroneous energy measurement.

about 10% of the Hp+Mp events, which also have average energy resolutions degraded by 0.1-2.5 eV. However, the other three quadrants produce about 55 counts s^{-1} with an energy resolution within 0.1 eV of the fiducial 5 eV value. The count rates in the other quadrants are also low enough that a crosstalk exclusion filter ($\pm$25 ms) can be applied with little or no impact on the number of Hp+Mp events, but such filtering should not be necessary. **Note:** The structure of the PSF wings, based on a ray trace incorporating ground measurements, is not yet fully known, especially as a function of off-axis angle. Figure 8.4 thus does not have very high fidelity and is shown as an example. Observers should also bear in mind the effects of roll angle.

Table 8.1 illustrates how the optimal configuration (in bold) changes with increasing count rate for a sample spectrum from a point source. The Be filter is omitted as makes hardly any difference over the gate valve itself (a much thicker Be filter). For sources brighter than about 3 Crab, the ND filter becomes optimal; at 10 Crab off-axis pointing also becomes important.

While this table is for the purpose of illustration (adopting a modestly absorbed $\Gamma = 2$ power law spectrum), it reveals the basic strategy: first try a filter, then point off axis

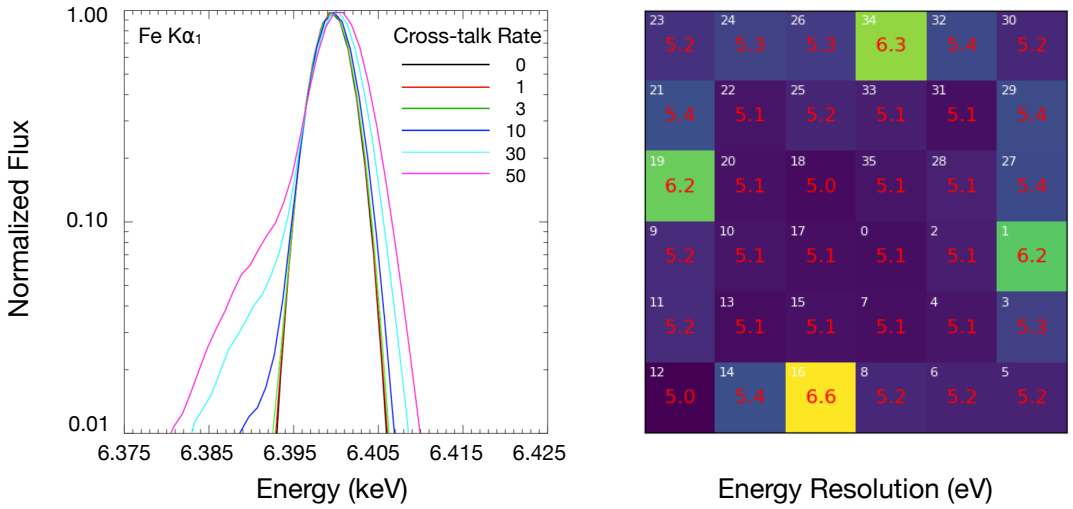

Figure 8.2: Left: Increasing contamination by cross-talk child pulses both broadens lines and shifts their centroids. At high count rates, this can significantly alter the energy resolution in individual pixels, as shown here for an example Fe Kα line. Right: As an example, this Resolve pixel map shows the energy resolution (i.e., broadening) in each pixel when starting from $\Delta E = 5$ eV and observing a source four times brighter than the Crab Nebula at the array center. The four exterior pixels with the worst resolution are *electrically adjacent* to the central four pixels. Note that the map is not weighted by the event rate or grade: despite the better energy resolution in the central pixels, there are hardly any Hp+Mp events from those pixels.

towards the corner of one quadrant. We do *not* recommend using the quadrant with the dummy pixel, as the CPU for that quadrant must process the ^{55}Fe calibration source photons that are necessary for gain tracking. We have summarized general recommendations as a function of source brightness in Table 8.2. Here we offer a few additional comments for proposers:

First, proposers should use the effective area curves (encoded in the ARFs) to estimate the count rates for different filters (e.g., via WebPIMMS: `https://heasarc.gsfc.nasa.gov/cgi-bin/Tools/w3pimms/w3pimms.pl`). On-axis, point-source ARFs are sufficient for this purpose when proposing; there is a small ($< 10\%$) decline in effective area for off-axis pointing due to vignetting, but this is not sufficient to change the optimal strategy. Observers should also be aware of the impact of uncertainty in the spectral shape on the expected count rate and the uncertainty in the PSF wings to the Resolve illumination pattern for the off-axis pointing. Note that values quoted here are based on the PSP algorithm, measurements from *Hitomi* on the time needed to process events of each grade, measurements of the cross-talk contamination, and ground calibration measurements of the PSF and the energy resolution. As more on-orbit XRISM measurements are made, the model will be updated in future cycles.

Table 8.1: Resolve Count Rates

Flux (0.3-10 keV 10^{-8} erg s^{-1} cm^{-2})	No filter			ND Filter			ND+Off-axis		
	Total	Hp+Mp (ph s^{-1})	Clean	Total	Hp+Mp (ph s^{-1})	Clean	Total	Hp+Mp (ph s^{-1})	Clean
0.5	35	30	***15***	10	10	5	10	10	5
1.0	70	45	***30***	20	15	5	20	15	10
2.0	140	60	***50***	30	30	15	30	25	20
3.0	210	70	***50***	50	35	15	50	35	25
4.0	280	70	***50***	70	45	30	60	40	25
5.0	350	80	***45***	90	50	30	80	40	30
6.0	420	85	40	100	50	***45***	100	40	25
7.0	490	85	30	120	60	***45***	110	50	25
8.0	560	80	25	140	60	***45***	130	50	25
9.0	630	80	25	160	65	***50***	150	50	25
10.	700	80	10	170	70	***55***	160	50	30
20.	1410	70	1	340	80	***40***	330	65	30
50.	3520	30	0	860	80	5	810	65	***35***

All values assume an on-axis source except for the "off-axis" set at a fiducial offset of +0.5 arcmin offset in both RA and Dec. "Clean" events are those H+Mp events whose average energy resolution is within 2% of a fiducial 5 eV resolution. Bold text indicates the optimal rate and thus observing configuration. The input spectrum is a $\Gamma = 2$ power law with photoelectric absorption from 10^{21} cm^{-2} of foreground atomic gas. Exact values are sensitive to the spectrum, structure in the PSF wings, etc. This table is for illustration only.

Secondly, proposers should estimate the sensitivity of their scientific goals to small changes in energy resolution. We defined clean Hp+Mp events as those originating in pixels with average energy resolution within 2% of the native resolution (i.e., 5.1 eV for a native 5 eV). This would make the cross-talk degradation smaller than the calibration uncertainty to the point where it could essentially be ignored. Proposals that are not focused on fine line structures or that can accept greater velocity uncertainty may maximize the total Hp+Mp rate rather than the "clean" rate. The clean rate cannot be estimated from the ARFs alone but requires knowing the expected count rate in each pixel (e.g., from *heasim*), so that one can make an estimate of the cross-talk rate in each pixel, and *also* the incident spectrum, so that one can estimate the energy degradation for a line of interest. A tool to estimate the impact of cross-talk for an input spectrum will be made available at `https://heasarc.gsfc.nasa.gov/docs/xrism/proposals/index.html`, but it is not necessary: Table 8.1 can be used as a guide for proposing to maximize the total Hp+Mp rate or the clean Hp+Mp rate.

8.5 Filtering Cross-talk on the Ground

Once the data are in hand, the main objective is to maximize the clean Hp+Mp counts. The definition of "clean" very much depends on the science goal: extracting a spectrum from the entire array makes sense for maximizing the signal-to-noise ratio (S/N) in a short

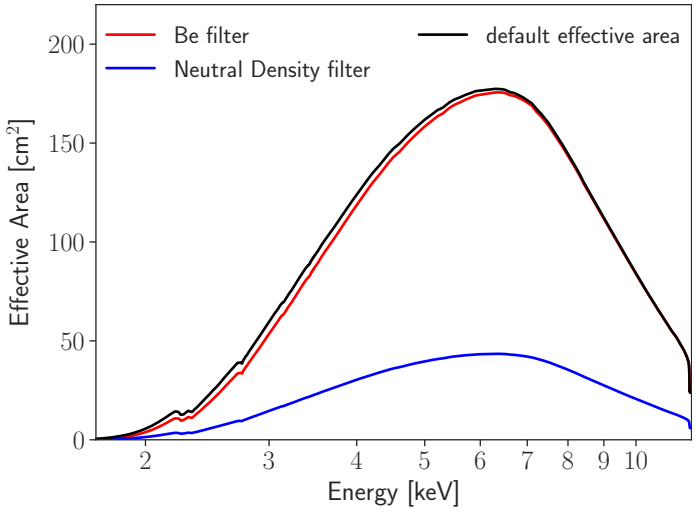

Figure 8.3: Resolve effective area curves with the gate valve closed for no filter (black), the Be filter (red), and the neutral-density filter (blue). The neutral-density filter reduces the count rate by about a factor of four across the bandpass. For filter transmission curves see Figure 5.13. The Be filter is optimized for suppressing (continuum) events at low energy in favor of preserving high-resolution events in the Fe-K complex.

time frame, while detailed velocity measurements using an Fe XXVI absorption line may require selecting events only from pixels largely unaffected by cross-talk. We defined clean above as 2% of the native energy resolution (i.e., 5.1 eV for a 5.0 eV native resolution), which is well within the calibration uncertainty, but observers can estimate the cross-talk impact from the data themselves and adopt their own definition of clean.

The simplest way to *eliminate* cross-talk contamination is to exclude ±25 ms from each pulse in each electrically neighboring pixel, which can be captured via a good-time interval file. This exclusion window is in the CALDB and, while not automatically executed in the pipeline processing, can be implemented with the XRISM software tools. The impact on the effective exposure time is a strong function of pixel, since the pixels near the core of the PSF will have by far the highest count rates, and their electrically neighboring pixels are not only the ones physically adjacent on the detector. If this removes too many events, the next simplest approach is to use the count rate per pixel to determine which electrically neighboring pixels will be most affected by cross-talk degradation and omit those pixels from a combined spectrum. This can be predicted as a function of count rate, position, and a rough idea of the spectrum, as shown in Figures 8.2 and 8.4. For these purposes, the MXS can be treated as part of the same source as it will be affected by cross-talk filtering.

We note that these predictions carry inherent uncertainty of about 1-2% of the native energy resolution. This is because only a small fraction of cross-talk pulses significantly affect the energy measurement (those that occur near the peak of a real pulse), and the magnitude of the error also depends on the relative energy of the real pulse and the cross-

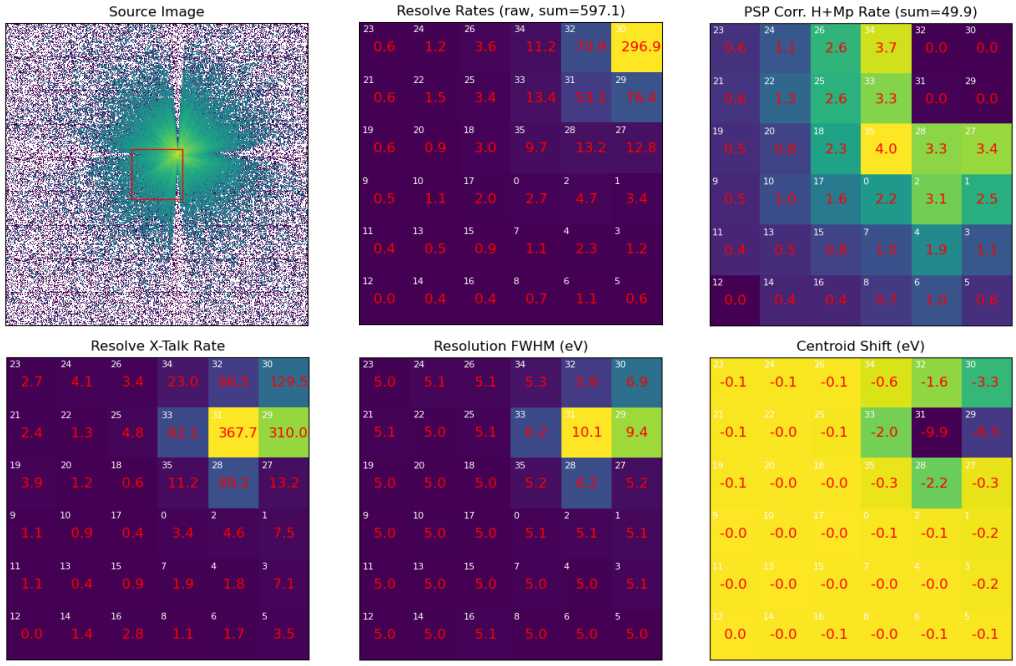

Figure 8.4: These six plots show a mock image (top left), raw incident count rate (top center), processed Hp+Mp rate (top right), cross-talk child pulse rate (bottom left), effective spectral resolution (bottom center), and centroid shift (bottom right) in each pixel for a 10^{-7} erg s^{-1} cm^{-2} source observed no filters. The top right quadrant is sacrificed to maximize the Hp+Mp rate in the other three quadrants, as each quadrant is processed separately in the PSP.

talk parent pulse. Since photon arrival is a Poisson process, any given observation will deviate from the average a small amount.

To determine the importance of cross-talk contamination, consider that line centroids can be measured to a precision

$$\frac{\Delta v}{c} = \frac{1}{2.35(S/N)} \frac{\Delta E}{E} \tag{8.1}$$

For an instrumental resolution of 5 eV, an Fe Kα line at 6.4 keV, and $S/N = 10$, one can measure Δv to ± 10 km s^{-1}. Degrading the resolution to 6 eV would lead to a constraint of ± 12 km s^{-1}. Line broadening can be determined to a precision

$$\frac{\Delta \sigma_{\rm line}}{\sigma_{\rm line}} = \frac{1}{\sqrt{2}(S/N)} \frac{\sigma^2_{\rm line} + \sigma^2_{\rm inst}}{\sigma^2_{\rm line}} \tag{8.2}$$

For a line of intrinsic width 1 eV and an instrumental resolution of 5 eV, $S/N \sim 12$ is needed to measure $\sigma_{\rm line}$ to 30% precision. At 6 eV, $S/N \sim 15$ is needed to make the

same measurement. It is also important to consider the limiting precision on a prospective measurement from systematic calibration uncertainty, such as gain differences between pixels, which effectively degrades the energy resolution.

8.6 Summary of Observing Recommendations

The optimal combination of offset pointing and/or filter depends on the source type and science goals. Here we provide basic guidelines for observing point sources of various fluxes with the goal of characterizing Fe K emission or absorption above 6 keV in a source otherwise characterized by an absorbed power law.

Table 8.2: Bright Source Observing Recommendations.

Flux (0.3-10 keV 10^{-8} erg s^{-1} cm^{-2})	Recommendation	Clean Rate (ph s^{-1})
0.5-1	On axis, no filter	20-30
1-3	On-axis, no filter	40-55
3-10	On-axis, ND	40-60
10-30	On-axis (0-0.5′), ND	40-50
50	Off-axis (1.0′), ND	30

"Clean" events are those H+Mp events whose average energy resolution is within 2% of the fiducial 5 eV resolution. The input source is a point source with a a $\Gamma = 2$ power law spectrum with photoelectric absorption from 10^{21} cm^{-2} of foreground atomic gas. Exact values are sensitive to the spectrum, structure in the PSF wings, and off-axis position. At all fluxes, the appropriate Xtend mode is 1/8 window+burst, as the source always produces >500 counts s^{-1}.

References

Bautz, M. W., LaMarr, B. J., Miller, E. D., et al. 2007, *Proc. of SPIE*, 6886, 68860Q. doi: 10.1117/12.734094

Bautz, M. W., Miller, E. D., Sanders, J. S., et al. 2009, *PASJ*, 61, 1117. doi:10.1093/pasj/61.5.1117

Bebek, C. J., Bercovitz, J. H., Groom, D. E., et al. 2004, *Proc. of SPIE*, 5167, 50. doi:10.1117/12.506221

Boissay-Malaquin, R., Hayashi, T., Tamura, K., et al. 2022, *Proc. of SPIE*, 12181, 121811U. doi:10.1117/12.2627563

Boyce, K. R., Audley, M. D., Baker, R. G., et al. 1999, *Proc. of SPIE*, 3765, 741. doi:10.1117/12.366557

Bulbul, E., Randall, S. W., Bayliss, M., et al. 2016, *ApJ*, 818, 131. doi:10.3847/0004-637X/818/2/131

de Vries, C. P., den Herder, J. W., Costantini, E., et al. 2010, *Proc. of SPIE*, 7732, 773213. doi:10.1117/12.855880

de Vries, C. P., Haas, D., Yamasaki, N. Y., et al. 2018, *Journal of Astronomical Telescopes, Instruments, and Systems*, 4, 011204. doi:10.1117/1.JATIS.4.1.011204

Eckart, M. E., Adams, J. S., Boyce, K. R., et al. 2018, *Journal of Astronomical Telescopes, Instruments, and Systems*, 4, 021406. doi:10.1117/1.JATIS.4.2.021406

Hayashida, K., Tomida, H., Mori K., et al. 2018, *Proc. of SPIE*, 10699, 1069923. doi:10.1117/12.2311446

Hitomi Collaboration et al. 2018, *PASJ*, 70, 9. doi:10.1093/pasj/psx138

Iizuka, R., Hayashi, T., Maeda, Y., et al. 2018, *Journal of Astronomical Telescopes, Instruments, and Systems*, 4, 011213. doi:10.1117/1.JATIS.4.1.011213

Ishisaki, Y., Yamada, S., Seta, H., et al. 2018, *Journal of Astronomical Telescopes, Instruments, and Systems*, 4, 011217. doi:10.1117/1.JATIS.4.1.011217

Kanemaru, Y., Sato, J., Mori, K., et al. 2019, *Journal of Instrumentation*, 14, C04003. doi:10.1088/1748-0221/14/04/C04003

Kanemaru, Y., Sato, J., Takaki, T., et al. 2020, *Nuclear Instruments and Methods in Physics Research A*, 984, 164646. doi:10.1016/j.nima.2020.164646

Kelley, R. L., Mitsuda, K., Allen, C. A., et al. 2007, *PASJ*, 59, S77. doi:10.1093/pasj/59.sp1.S77

Kelley, R. L., Akamatsu, H., Azzarello, P., et al. 2016, *Proc. of SPIE*, 9905, 99050V. doi:10.1117/12.2232509

Kilbourne, C. A., Sawada, M., Tsujimoto, M., et al. 2018, *PASJ*, 70, 18. doi:10.1093/pasj/psx139

Kilbourne, C. A., Adams, J. S., Brekosky, R. P., et al. 2018, *Journal of Astronomical Telescopes, Instruments, and Systems*, 4, 011214. doi:10.1117/1.JATIS.4.1.011214

Markevitch, M., Mushotzky, R., Inoue, et al. 1996, *ApJ*, 456, 437. doi:10.1086/176668

Midooka, T., Tsujimoto, M., Kitamoto, S., et al. 2021, *Journal of Astronomical Telescopes, Instruments, and Systems*, 7, 028005. doi:10.1117/1.JATIS.7.2.028005

Mitsuda, K., Kelley, R. L., Boyce, K. R., et al. 2010, *Proc. of SPIE*, 7732, 773211. doi:10.1117/12.856778

Mitsuda, K., Kelley, R. L., Akamatsu, H., et al. 2014, *Proc. of SPIE*, 9144, 91442A. doi:10.1117/12.2057199

Mizumoto, M., Tsujimoto, M., Cumbee, R., et al. 2022, *Proc. of SPIE*, 12181, 5Z. doi:10.1117/12.2628784

Mori, H., Iizuka, R., Shibata, R., et al. 2005, *PASJ*, 57, 245. doi:10.1093/pasj/57.1.245

Mori, K., Tomida, H., Nakajima, H., et al. 2022, *Proc. of SPIE*, 12181, 121811T. doi:10.1117/12.2626894

Moseley, S. H., Kelley, R. L., Schoelkopf, R. J., et al. 1988, *IEEE Transactions on Nuclear Science*, 35, 59. doi:10.1109/23.12673

Nakajima, H., Maeda, Y., Uchida, H., et al. 2018, *PASJ*, 70, 21. doi:10.1093/pasj/psx116

Nakajima, H., Hayashida, K., Tomida, H., et al. 2020, *Proc. of SPIE*, 11444, 1144423. doi:10.1117/12.2560348

Okajima, T., Serlemitsos, P. J., Soong, Y., et al. 2012, *Proc. of SPIE*, 8443, 844320. doi:10.1117/12.926443

Porter, F. S., Adams, J. S., Brown, G. V., et al. 2010, *Proc. of SPIE*, 7732, 77323J. doi:10.1117/12.857888

Serlemitsos, P. J., Soong, Y., Okajima, T., et al. 2010, *Proc. of SPIE*, 7732, 77320A. doi:10.1117/12.857355

Szymkowiak, A. E., Kelley, R. L., Moseley, S. H., et al. 1993, *Journal of Low Temperature Physics*, 93, 281. doi:10.1007/BF00693433

Tamura, K., Hayashi, T., Boissay-Malaquin, R., et al. 2022, *Proc. of SPIE*, 12181, 121811V. doi:10.1117/12.2629534

Tanaka, T., Uchida, H., Nakamjima, H., et al. 2018, *Journal of Astronomical Telescopes, Instruments, and Systems* 4, 011211. doi:10.1117/1.JATIS.4.1.011211

Tsunemi, H., Hayashida, K., Nakajima, H., et al. 2013, *Proc. of SPIE*, 8859, 88590C. doi:10.1117/12.2023267

Uchida, H., Tanaka, T., Amano, Y., et al. 2020, *Nuclear Instruments and Methods in Physics Research A*, 978, 164374. doi:10.1016/j.nima.2020.164374

Uchiyama, Y., Ozawa, M., Matsumoto, H., et al. 2009, *PASJ*, 61, S9. doi:10.1093/pasj/61.sp1.S9

Willingale, R., Aschenbach, B., Griffiths, R. G., et al. 2001, *A&A*, 365, L212. doi:10.1051/0004-6361:20000114

Yoneyama, T., Noda, H., Hanaoka, M., et al. 2020, *Proc. of SPIE*, 11444, 1144425. doi:10.1117/12.2561524

Yoneyama, T., Noda, H., Hanaoka, M., et al. 2021, *Nuclear Instruments and Methods in Physics Research A*, 985, 164676. doi:10.1016/j.nima.2020.164676